ANALYSIS AND SIMULATION OF A COLD-AIR POOL AND HIGH WINTERTIME OZONE EPISODE IN UTAH'S UINTAH BASIN

by

Erik M. Neemann

A thesis submitted to the faculty of
The University of Utah
in partial fulfillment of the requirements for the degree of

Master of Science

Department of Atmospheric Science

The University of Utah

August 2014

The University of Utah Graduate School

STATEMENT OF THESIS APPROVAL

The following faculty members served as the supervisory committee chair and members for the thesis of Erik M. Neemann. Dates at right indicate the members' approval of the thesis.

John D. Horel, Chair	03/31/2014 Date Approved
W. James Steenburgh, Member	03/31/2014 Date Approved
John C. Lin, Member	03/31/2014 Date Approved

The thesis has also been approved by Kevin D. Perry
Chair of the Department/School/College of Atmospheric Sciences
and by David B. Kieda, Dean of The Graduate School.

ABSTRACT

High ozone concentrations associated with a winter cold-air pool during the Uintah Basin Winter Ozone Study are investigated. Field campaign observations combined with numerical simulations are analyzed in Utah's Uintah Basin from 1–6 February 2013 when ozone concentrations exceeded 150 ppb. Cold-air pool sensitivity to cloud microphysics and snow cover variations within the Weather Research and Forecasting model simulations are examined, along with their impact on air quality in Community Multiscale Air Quality model simulations. Ice-dominant clouds are found to enhance cold-air pool strength compared to liquid-dominant clouds through increased nocturnal cooling and decreased longwave cloud forcing. The presence of snow cover also strengthens cold-air pool structure by lowering near-surface air temperatures and increasing boundary layer stability due to reduced absorbed solar insolation by the high-albedo snow surface. Snow cover also increases ozone levels by enhancing solar radiation available for photochemical reactions. Flow features affecting Uintah Basin cold-air pools that affect pollutant mixing and air quality within the basin are studied, including: penetration of clean air into the basin from across the surrounding mountains, elevated easterlies within the inversion layer, and diurnal upslope and drainage flows.

TABLE OF CONTENTS

LIST OF TABLES

ACKNOWLEDGEMENTS

I thank Professor John Horel for his invaluable guidance, focus, and constructive criticism throughout the entirety of my research. I thank my two committee members, Professors Jim Steenburgh and John Lin for comments and suggestions during the draft editing process. I thank Erik Crosman for many hours of assistance with WRF and informative discussions about cold-air pools. I thank the department's WRF Users Group for expanding my knowledge on a monthly basis, and particularly John McMillen for many discussions that aided my work. Finally, I thank my parents for all of the support and encouragement over the years.

The support and resources from the Center for High Performance Computing at the University of Utah is gratefully acknowledged. This research was supported by the Utah Division of Air Quality as part of the 2013 Uinta Basin Winter Ozone Study and I thank Lance Avey, for running CMAQ and contributing to several discussions about its capabilities and limitations. I thank Alex Jacques, Matt Lammers, John and Maggie Lawson, and Nola Lucke of the University of Utah for their work during the 2013 UBWOS field campaign. I thank Utah State University and all other participants of the 2013 UBWOS for assisting in the collection of atmospheric and air quality data and the NASA SPoRT program for reprocessing satellite imagery used in this study.

I gratefully acknowledge the support of the U.S. Air Force Institute of Technology. The views expressed in this thesis are those of the author and do not reflect the official policy or position of the United States Air Force, Department of Defense, or the U.S. Government.

CHAPTER 1

INTRODUCTION

High concentrations of ozone are known to have an adverse impact on human health, including respiratory irritation and inflammation, reduced lung function, aggravated asthma, and long-term lung damage (Lippmann 1993; Bell et al. 2004). Ozone is formed through photochemical reactions of pollutants emitted from industrial sources and vehicles known as "ozone precursors." These precursors are typically nitrogen oxides (NO_X) and volatile organic compounds (VOCs) (Pollack et al. 2013). Once thought to primarily be an urban, summertime problem (due to the high insolation required for photochemical reactions), high ozone levels have recently been detected during the wintertime in snow-covered rural basins with significant industrial fossil fuel extraction activities (Schnell et al. 2009). The presence of snow cover greatly increases the surface albedo and enhances the actinic flux (quantity of light available to molecules) in the near-surface atmosphere leading to photolysis rates notably larger (~50%) than those observed in summer (Schnell et al. 2009). In addition, the shallow and highly stable boundary layer often observed during the wintertime in snow-covered rural basins further exacerbates the problem by trapping the high ozone concentrations in the lowest several hundred meters of the atmosphere. A schematic of this typical setup is shown in Fig. 1.1.

Schnell et al. (2009) first analyzed high wintertime ozone episodes in Wyoming's Upper Green River Basin in early 2005. By 2008, this region experienced several instances when the 8-hr average ozone concentrations were over 100 ppb, well above the EPA's National Ambient Air Quality Standard (NAAQS) of 75 ppb (U.S. EPA 2013), and far above the background levels of ozone near the earth's surface that typically range between 20–45 ppb (U.S. EPA 2006).

Similar high levels of ozone were first detected in northeast Utah's Uintah Basin in 2009 (Lyman and Shorthill 2013). The Uintah and Upper Green River Basins share many characteristics, including extensive oil and gas operations, frequent winter snow cover, and a similar climate and vegetation. Fossil fuel production, particularly gas, has increased in the Uintah Basin over the last several years (Fig. 1.2), and will likely continue to increase. In March 2014, there were over 9,400 producing wells in the basin and over 3,600 additional permit applications since the beginning of 2012. These wells, and associated ozone precursor sources, are currently operating throughout the basin with oil wells primarily clustered in the west and gas wells clustered in the east (Fig 1.3).

Extensive scientific research has been conducted in the Uintah Basin to better understand the wintertime rural ozone problem both chemically and meteorologically during the past several winters (Lyman and Shorthill 2013; Stoeckenius and McNally 2014). These field campaigns point to the importance of nitrous acid and formaldehyde in the surface snow pack for ozone production. Meteorologically, the importance of snow cover, cloud cover, interbasin flows, and terrain-flow interactions in the evolution of the shallow, stable boundary layers associated with these high wintertime ozone episodes are recognized as being important but have not been well documented.

The presence of snow cover in combination with a stable, persistent boundary layer cold-air pool (CAP) is integral to these wintertime high ozone events (Schnell et al. 2009). Considerable year-to-year variations in seasonal snow cover exist in the Uintah Basin, depending on whether or not strong early-winter storms deposit sufficient snow to last into February or new snow is deposited during that month. These variations in annual snow cover lead to similar variations in the occurrence of high ozone events (Lyman and Shorthill 2013). For instance, snow cover was absent from the basin during February 2012 and much of February 2014 and ozone levels remained low during those months, while February 2013 saw extensive snow cover and several high ozone events. The large variations in snow cover between February 2013 and 2014 are illustrated in Fig. 1.4. The basin was fully covered with snow on 2 February 2013 (Fig. 1.4a), but on 2 February 2014 it was only partially snow-covered (Fig. 1.4b) and by 21 February (Fig. 1.4c), the snow had largely disappeared.

A persistent CAP is defined here following Lareau et al. (2013) as a stagnant, stable layer of air confined in a topographical depression (with warmer air typically aloft) that lasts for more than a diurnal cycle. They result when solar heating and subsequent boundary layer growth is insufficient to destroy the presence of a deep low-level volume of cold air, causing multiday episodes of stagnation. Persistent CAPs and their resulting impacts on local weather and particulate air pollution concentrations in urban basins have been extensively studied (Whiteman et al. 2001; Malek et al. 2006; Silcox et al. 2012; Lareau et al. 2013; Lareau 2014; Lareau and Horel 2014). Persistent CAPs are most often a wintertime phenomena, with their occurrence largely driven by synoptic weather patterns and upper level ridging. Their onset is coincident with midlevel warming and

they are eventually removed by midlevel cooling (Reeves and Stensrud 2009). The characteristics of persistent CAPs can be modulated by the presence of snow cover, local topography, and terrain-flow interactions with migratory weather systems. They are also often associated with low clouds, fog, freezing precipitation, and hazardous ground and air travel. Observational and numerical studies have been conducted on CAPs for a variety of idealized (Zangl 2005a; Katurji and Zhong 2012; Lareau 2014) and actual topographic basins (Whiteman et al. 2001; Clements et al. 2003; Zangl 2005b; Billings et al. 2006; Reeves & Stensrud 2009; Reeves et al. 2011; Lareau et al. 2013; Lareau and Horel 2014). The basins vary in size from thousands of km^2 (Columbia Basin, WA) to a single km^2 (Peter Sinks, Utah). In many cases, and particularly in smaller basins, operational models have a difficult time capturing the presence of CAPs (Hart et al. 2005; Reeves et al. 2011). Often times this can be due to the inaccurate representation of terrain from coarse grid-spacing and attendant inability to resolve localized flows.

Operational weather forecast models also regularly struggle with explicitly predicting low clouds within persistent CAPs (overprediction or underprediction of low clouds and fog are both common occurrences), as well as the turbulent mixing processes occurring at the interface between synoptically-driven winds and a relatively calm, stable boundary-layer (Holtslag et al. 2013). However, relatively few numerical studies have examined the impact of clouds and cloud microphysics on CAP formation and evolution. In addition, the impacts of cloud-topped boundary-layers on pollutant dispersion have received considerably less attention than clear-sky cases (Verzijlbergh et al. 2009). Zangl (2005a) indirectly examined the effect of cloud particle phase on the formation of extreme CAPs in the Gstettneralm sinkhole, Austria. He found that an efficient drying

mechanism was required for extreme CAPs to develop. Without one, the formation of fog and its accompanying longwave radiation would prevent the low-level cooling necessary for a strong CAP. Zangl found that the most efficient process for drying the atmosphere was through the formation of cloud ice and its eventual sedimentation. Moreover, the lower vapor pressure over ice compared to water allowed for preferential growth of cloud ice at the expense of cloud water. This accelerated the drying process, with even greater acceleration possible if cloud ice was able to grow into snow, which has a greater fall speed. Simulations dominated by cloud ice were found to dry out the atmosphere more effectively than simulations with a mixture of cloud ice and cloud water, translating to greater cooling and lower temperatures in the ice-dominant case.

The impact of the snow-albedo feedback on surface temperatures of interior continental locations during wintertime is known to be high. However, in remote locations such as the Uintah Basin, where snow cover is typically very thin (~5–10 cm) and spatially and temporally variable, accurately assessing snow mass or water equivalent for input into numerical models can be difficult (Jeong et al. 2013). Despite their importance in wintertime persistent CAP formation and maintenance, relatively few numerical studies have examined in detail the impact of snow cover on CAPs. Billings et al. (2006) studied the impact of snow cover on a CAP in the Yampa Valley, Colorado. Although unable to produce a temperature inversion, simulations with snow cover produced an isothermal profile that more closely aligned with observations than snow-free simulations. The snow-free simulations were incapable of producing the CAP and had the highest temperatures located on the valley floor. They concluded that the primary influence of snow cover was to increase the surface albedo and decrease the

sensible heat flux. Snow cover also increased the latent heat flux for certain locations due to melting and evaporation. Zangl (2005a) also investigated the role of snow cover on the nocturnal formation of extreme CAPs. He found that a small heat conductivity of the ground was important for efficient cooling and was most readily accomplished by the presence of fresh snowfall. Comparison between a snow-covered and grass-covered sinkhole floor suggested that the larger surface heat capacity of the grass floor resulted in more gradual cooling, a smaller afternoon-morning temperature difference, and weaker static stability than simulations with a snow-covered floor. Interestingly, the grass case produced no cloud cover in the center of the basin, while snow cases did.

The topography of the Uintah Basin is highly conducive to the formation of strong CAPs in the presence of snow cover (Fig. 1.5). It is a large, deep, nearly bowl-like depression bounded to the north by the Uinta Mountains, the west by the Wasatch Range, and the south by the Tavaputs Plateau. Covering over 15,000 km^2, the lowest elevations in the center of the basin are below 1450 m and the terrain extends above 1950 m on all sides, with ridgelines reaching well above 2500 m to the north, west, and south. The only outlet below 1950 m along the basin's perimeter is the deep, narrow Desolation Canyon where the Green River drains south into east-central Utah, eventually emptying into the Colorado River. As a winding, narrow river canyon, this outlet provides very little airmass exchange between the Uintah Basin and eastern Utah. The synergy between the confining topography, winter snow cover, and surface high pressure often result in a stagnant, stably stratified environment with little horizontal mixing. At the same time, vertical mixing is inhibited by the existence of a strong inversion atop the shallow, cold planetary boundary layer (PBL) that effectively shields the lower elevations of the basin

from weak, transient synoptic weather disturbances.

The detailed meteorology associated with wintertime high ozone episodes in the Uintah Basin is not well-understood and only limited observational data sets are available at isolated locations within the vast basin. While it is recognized that surface high pressure, strong temperature inversions, light winds, and the presence of snow cover are associated with high ozone episodes, detailed flow patterns and thermodynamic structure in the basin have been only partially explored. While a number of permanent surface weather stations exist within the basin at various elevations, upper level sounding data are not collected routinely. Hence, limited documentation exists regarding the highly stratified boundary layer in the basin during CAPs or the mesoscale terrain- and thermally-driven flows that likely play an important role in the transport and mixing of pollutants within the basin during these episodes. Understanding the ozone concentrations within the basin requires adequate meteorological information to drive air chemistry models capable of simulating the complex photochemical processes that lead to degraded air quality. The size, depth, and shape of the Uintah Basin provide an appropriate scale for mesoscale models and the frequent occurrence of persistent CAPs during the winter season presents numerous cases for examination. The local topography and scale of the basin potentially leave it more protected from synoptic flow interactions than persistent CAPs observed in other locales (Zangl 2005b; Lareau et al. 2013; Lareau and Horel 2014).

The purpose of this study is to use atmospheric and air quality numerical model simulations of a high ozone episode during early February 2013 in the Uintah Basin to help answer the following questions:

- *What is the sensitivity of simulated CAP structure and evolution to cloud microphysics?*
- *How do snow cover variations affect CAP simulations and structure?*
- *What are the important wind flow regimes in the Uintah Basin CAP? Can they be diagnosed by mesoscale modeling and how might they affect air quality in the basin?*
- *What is the influence of snow cover on air quality simulations in the Uintah Basin?*

The lifecycle of the persistent CAP in the Uintah Basin associated with high ozone levels between 1 and 6 February 2013 during the Uintah Basin Winter Ozone Study (UBWOS) is analyzed using the Weather Research and Forecasting Model (WRF). The sensitivity of the modeled persistent CAP to variations in snow cover, specification of surface albedo, and microphysics parameterizations is tested. Chapter 2 will describe data sources, model setup, and modifications used in the simulations, and Chapter 3 will discuss CAP evolution and modeling results. Chapter 4 will illustrate the sensitivity of simulated ozone concentrations during this period to surface and atmospheric forcings supplied to the Community Multiscale Air Quality Model (CMAQ). Conclusions and additional discussion will be provided in Chapter 5.

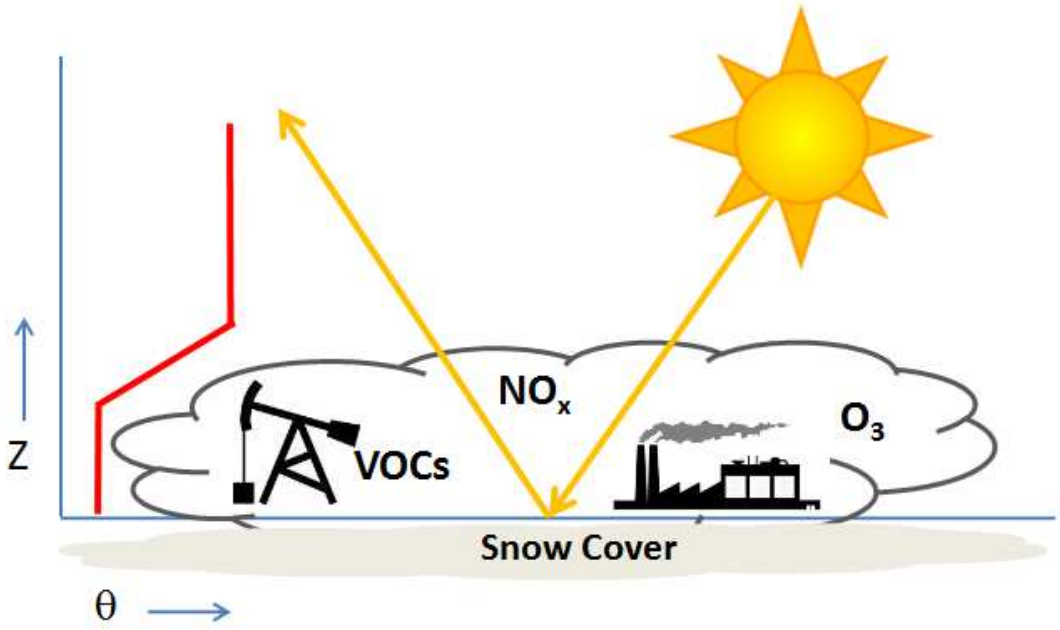

Fig. 1.1: Schematic of factors contributing to high ozone concentrations. Potential temperature profile (red line) with stable layer trapping ozone precursors (NO_x and VOCs) within the cold-air pool. Snow cover reflects solar radiation, increases photolysis rates, and leads to enhanced ozone (O_3) concentrations near the surface. Ice fogs are common in the cold-air pool.

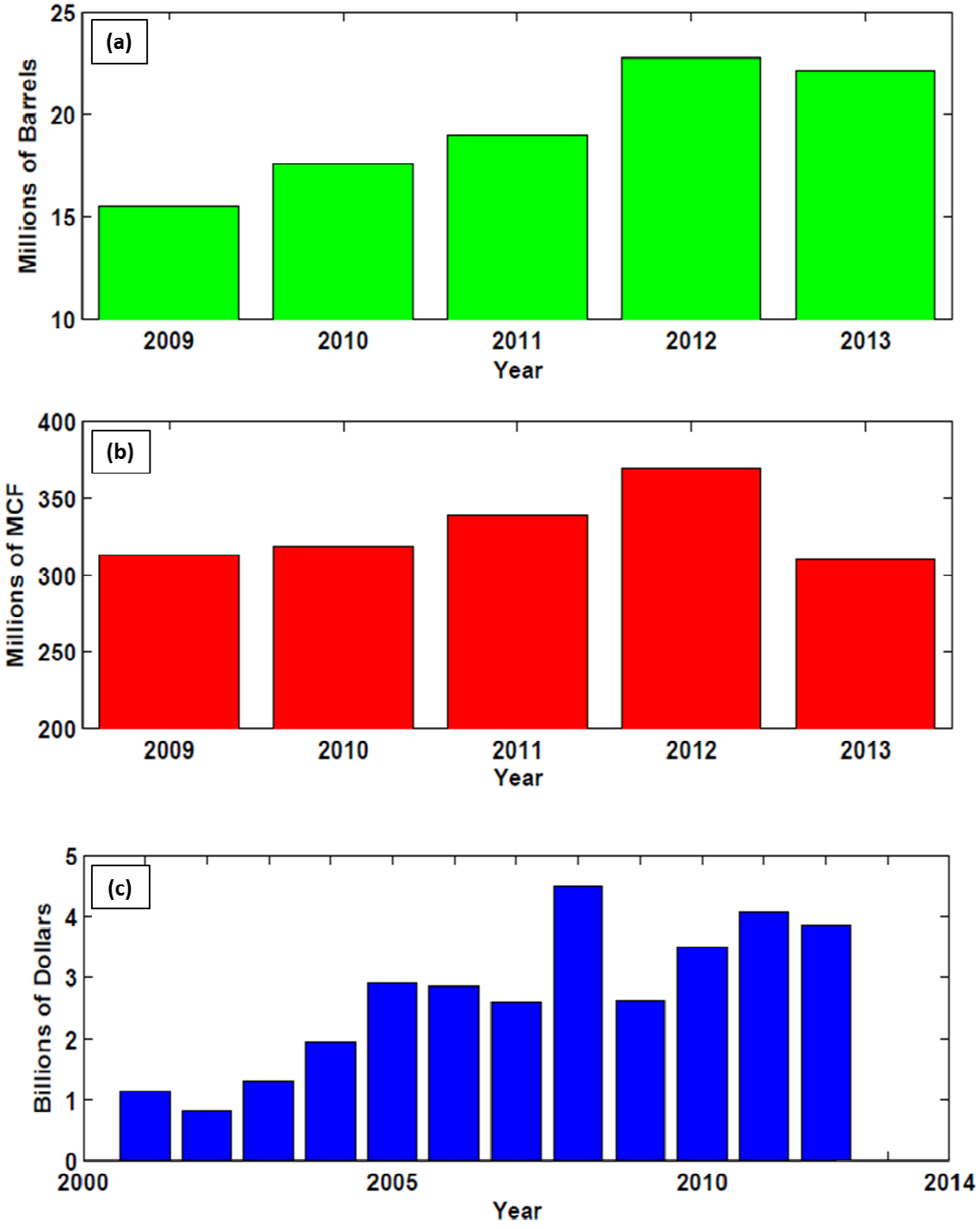

Fig. 1.2: Annual fossil fuel production in Uintah Basin since 2009 for (a) oil and (b) gas. (c) Total value of fossil fuel production in Utah since 2001. One barrel = 159 L, 1 MCF = 28.3 m^3. Data provided by Utah Division of Oil, Gas, and Mining.

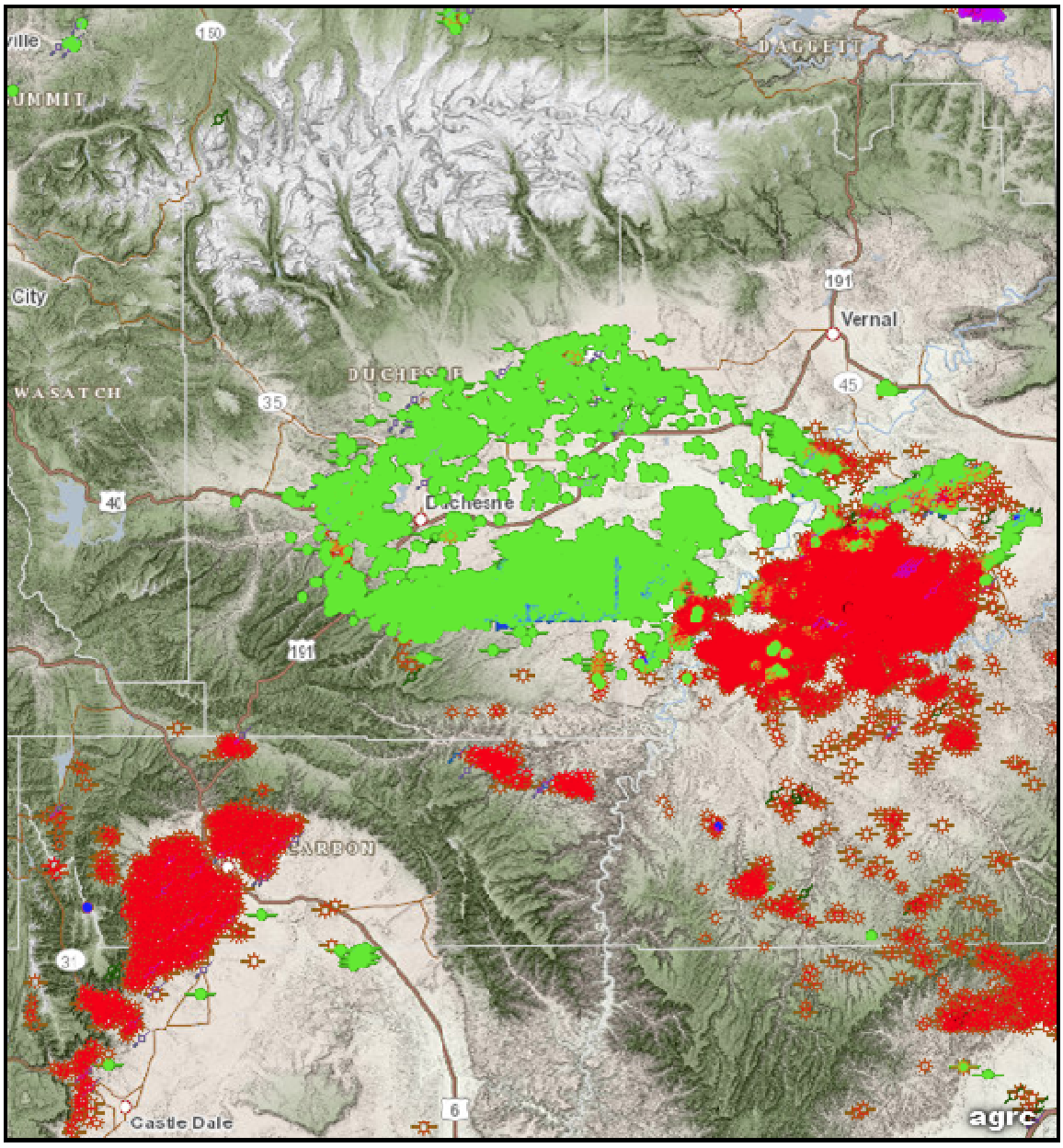

Fig. 1.3: Location of oil wells (green) and gas wells (red) operating inside the Uintah Basin in March 2014. Data and graphic provided by Utah Division of Oil, Gas, and Mining.

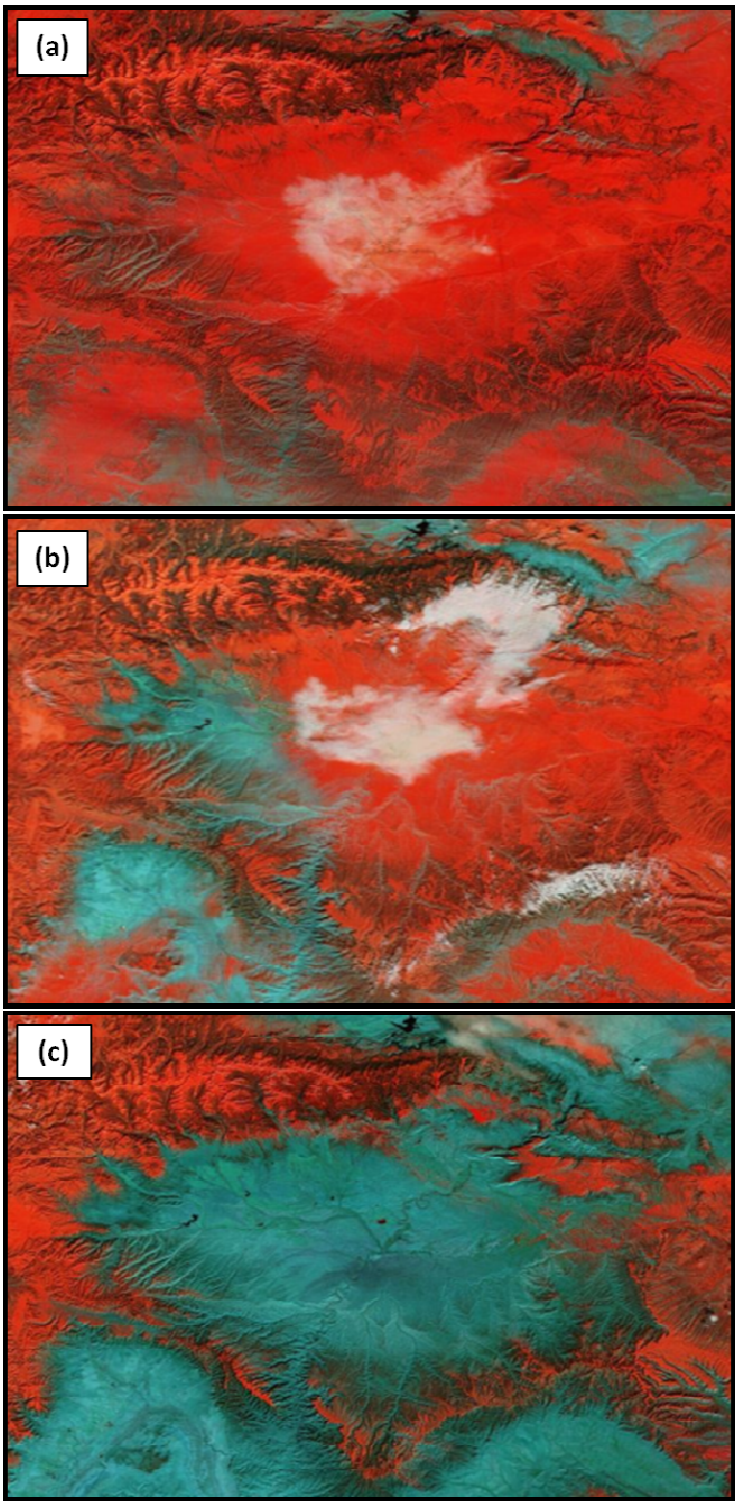

Fig. 1.4: NASA Short-term Prediction Research and Transition Center (SPoRT) snow-cloud product for: (a) 2 February 2013 (Uintah Basin completely snow covered with fog/stratus over low basin elevations), (b) 2 February 2014 (western basin snow free); and (c) 21 February 2014 (full basin snow-free). Snow cover appears red, bare ground is cyan, and clouds are white. Real-time SPoRT imagery: http://weather.msfc.nasa.gov/sport/

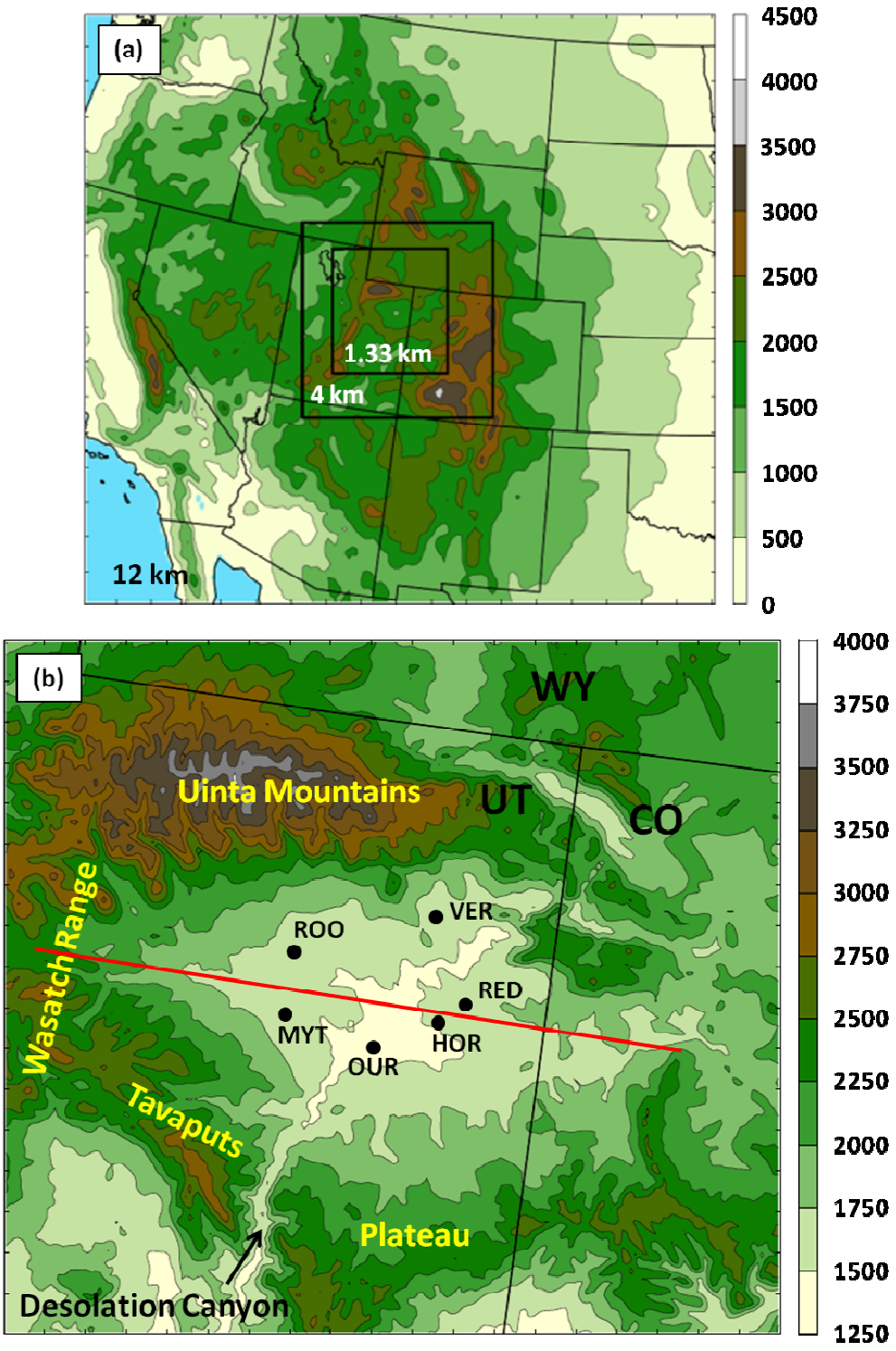

Fig. 1.5: Model domains and terrain elevation. (a) WRF 12-, 4-, and 1.33-km domains with terrain contoured every 500 m. (b) Uintah Basin subdomain with terrain contoured every 250 m and major geographic features labeled. Black dots indicate locations of surface stations used for verification: Horsepool (HOR), Myton (MYT), Ouray (OUR), Red Wash (RED), Roosevelt (ROO), and Vernal (VER). Red line indicates position of vertical cross sections shown later.

CHAPTER 2

DATA AND METHODS

2.1 Observational Data

The MesoWest cooperative network (Horel et al. 2002) was used to gather surface weather observations from a variety of permanent stations as well as those deployed for the 2013 UBWOS (Fig. 2.1). A description of the extensive instrumentation deployed for the intensive field campaign is detailed by Stoeckenius and McNally (2014). The University of Utah contribution included: vehicle-mounted 2B Technologies 205 ozone and temperature sensors; portable Graw rawinsonde base station with release of DFM-06 rawinsondes; and deployment near Roosevelt of a Vaisala CL-31 ceilometer combined with a trailer-mounted tower with temperature, relative humidity, incoming and outgoing solar radiation, and pressure sensors as well as a sonic anemometer to measure near-surface three-dimensional wind. For model validation, six surface stations with complete records were selected as representative of the conditions in the core of the basin (see Figs. 1.5b and 2.1).

2.2 Control Run WRF Model Setup

We model the evolution of a persistent cold air pool in the Uintah Basin that lasted from 31 January to 10 February 2013. The simulations were run for 144 hours from 0000

UTC (Coordinated Universal Time) 1 February 2013 to 0000 UTC 7 February 2013. This time frame represents the strongest period of the CAP and was one of the most heavily-instrumented periods during the 2013 UBWOS. Some of the highest-measured ozone concentrations during the winter season were observed during this period, with readings along a mobile transect of over 150 ppb taken near Ouray during the afternoon of 6 February 2013.

2.2.1 WRF Domain and Parameterization Schemes

A summary of the WRF model setup in this study is given in Table 2.1. We use WRF version 3.5 and the Advanced Research WRF core. The WRF model is nonhydrostatic, with a pressure-based, terrain-following (eta) vertical coordinate system. Simulations herein used 41 eta levels with the lowest 8 model layers ~20 m thick, the next 6 layers ~40 m thick, and the lowest 20 model levels within approximately 1 km of the terrain surface (Fig. 2.2). Three telescoping, one-way nested domains were employed to place the highest-resolution nest over the Uintah Basin. The grid spacing for each nested domain is 12, 4, and 1.33 km respectively (Fig. 1.5), with model time steps of 45, 15, and 5 seconds in subsequent domains. Operational North American Mesoscale Model (NAM) analyses were obtained from the National Oceanic and Atmospheric Administration's (NOAA) Operational Model Archive and Distribution System to initialize atmospheric and land surface variables (except for snow variables, see Section 2.2.2) as well as provide the lateral boundary conditions for the outer domain at 6-hour intervals for the duration of the 6-day simulations.

2.2.2 Prescribing Initial WRF Snow Cover in Uintah Basin

The available NAM snow cover analyses were found to poorly reflect the observed shallow snow layer in the Uintah Basin during February 2013. While the NAM analyses represented fairly well the spatial coverage of snow during the 1–6 February 2013 period, they overestimated snow depth and snow water equivalent (SWE) within the basin and underestimated them at higher elevations. In order to better represent the actual snow surface conditions, an "idealized" layer of snow was specified in the WRF initialization fields based on elevation, snow depth and SWE in a manner similar to Alcott and Steenburgh (2013). This prescribed snow cover was determined using all available observations: Snowpack Telemetry (SNOTEL); National Operational Hydrologic Remote Sensing Center (NOHRSC) analyses; Moderate Resolution Imaging Spectroradiometer (MODIS) imagery, and manual and automated observations from Community Collaborative Rain, Hail, and Snow Network (CoCoRaHS), and field campaign locations.

Figure 2.3 shows the specified relationship between snow depth, SWE and elevation relative to observations and NAM analyses, which demonstrates the over- (under-) estimation of snow by the NAM at low (high) elevations. The prescribed snow cover was applied within all model domains with no snow cover outside of the Uintah Basin below an elevation of 2000 m and a 17 cm snow depth from the basin floor up to an elevation of 2000 m. Above 2000 m, the snow depth was elevation-dependent, increasing to 100 cm for elevations at 2900 m or higher.

In addition, the NAM analyses underestimated snow albedo relative to observed shortwave radiation measurements at Horsepool and Roosevelt. For example, albedo

averaged from 1 January–2 March 2013 at Horsepool was 0.82 (Roberts et al. 2014), which is roughly 0.17 higher than the NAM analyses. Very low temperatures combined with repeated light rime deposition onto the snow surface during many nights apparently maintained the highly reflective surface. Hence, the snow albedo variable in WRF was modified to be 0.82 inside the basin, although the mean albedo at Horsepool during the 1–6 February period was actually a bit higher (~0.84). Furthermore, based on visual observations of the snow covering nearly all of the sparse vegetation in the basin during the 1–6 February period, changes were made to the WRF variable SNUP (threshold depth for 100% snow cover) in the vegetation parameter table for the two dominant vegetation/land use types: "shrubland" and "cropland/grassland mosaic." For these vegetation types, 20 kg m^{-2} of SWE was allowed to fully cover the vegetation in the Noah land surface model. The combination of increasing the snow albedo and modifying SNUP enabled the model surface to attain the high albedos observed during the field campaign (Fig. 2.4). The NAM analyses were used for all other land-surface variables in the snow-free region of these simulations, with surface albedo being determined by the National Land Cover Database 2006 (Fry et al. 2011).

2.3 Numerical Sensitivity Studies

A number of sensitivity tests were conducted to study the impact of variations in cloud type and snow cover on persistent cold air pools in the Uintah Basin. These tests are summarized in Table 2.2.

As will be shown in the next chapter, ice fog and low stratus were commonly observed throughout the basin during this event. However, simulations with the default

WRF model (referred to as the BASE run) tended to develop liquid-phase clouds. In order to test the sensitivity of the Uintah Basin CAP to ice versus liquid phase cloud particles, modifications were made to the Thompson microphysics scheme to produce fog/low clouds that were ice-phase dominant. We anticipated that ice-dominant clouds would have less radiative forcing than liquid-dominant clouds (Shupe and Intrieri 2004), allowing for stronger CAP formation, shallower PBLs, and lower low-level temperatures with smaller bias/errors. This was accomplished by editing the Thompson code in the lowest 15 model layers (~500 m) to change the treatment of cloud ice by turning off cloud ice sedimentation and the autoconversion of cloud ice to snow. These changes allowed low-level cloud ice to remain suspended and thrive through vapor deposition due to the lower vapor pressure over ice compared to water.

As discussed in Chapter 1, large variations of snow cover have been observed from winter to winter in the Uintah Basin. To examine the sensitivity of the conditions in the basin to snow cover, numerical simulations were run for the 1–6 February period using the same model configuration but varying the spatial extent of the snow cover. Fig. 2.5 shows the snow cover from the original NAM analysis (Fig. 2.5a) in comparison to the 3 other cases where snow cover is prescribed (Fig. 2.5b–d). The simulations with prescribed snow cover throughout the entire basin as discussed in Section 2.2 are shown in Fig. 2.5b (BASE and FULL). In the second sensitivity simulation (NONE), snow was removed from the basin for elevations below 2000 m (Fig. 2.5c) similar to what was observed during February 2012 and late February 2014. A more realistic coverage for the early February 2014 period is Fig 2.5d with snow cover removed from the western section of the basin (west of -110.4° W) for elevations below 2100 m (referred to as the

NW run). This partial erosion of the snowpack resulted from periods of downsloping flow over the Wasatch Range that left the snowpack further east in the basin undisturbed.

Several additional numerical simulations were conducted while searching for the best WRF model setup (not shown). These included the use of various microphysics and PBL schemes, prescribed cloud droplet concentrations, and modified initial/boundary condition files. Microphysics parameterizations tested included the WRF single moment 3-class and Morrison schemes. Additional modifications to the Thompson scheme were also explored before implementing the changes discussed above. The results from various microphysics testing converged to 3 general outcomes for the 1–6 February period: (1) a CAP dominated by dense liquid-phase stratus clouds; (2) a CAP with clear skies through the entire simulation; and (3) a CAP dominated by low-level ice fog. Outcome (2) was deemed unrepresentative of observed conditions, and outcomes (1) and (3) are analogs for the BASE and FULL simulations discussed further in this study. In addition to the MYJ (Mellor-Yamada-Janjic), the Yonsei University (YSU), Asymmetric Convective Model, Grenier-Bretherton-McCaa, and Bretherton-Park PBL schemes were tested. The YSU scheme with the Jimenez surface layer formulation and updated stability functions (Jimenez et al. 2012) was also considered, but did not show improved results over the original YSU scheme. The MYJ was chosen since it best represented the combination of moisture, stability, and temperature characteristics that were observed in the Uintah Basin for the simulated period. Simulations were conducted with cloud droplet concentrations prescribed for maritime (100×10^6 m^{-3}), continental (300×10^6 m^{-3}), and polluted continental (1000×10^6 m^{-3}) situations. However, changing the prescribed cloud droplet concentrations had no perceptible impact on CAP formation, so

the default value in the Thompson scheme was used (100×10^6 m^{-3}). Finally, NAM analysis initial/boundary conditions were tested with relative humidity reduced by 5, 20, and 40% to determine what effect it would have on cloud cover within the CAP. Reducing relative humidity was noted to delay the onset and decrease the coverage of clouds/fog for the first day or two of the simulation. Nonetheless, the final 3–4 days of the simulation converged on similar results for all cases, so the original NAM analysis data were used.

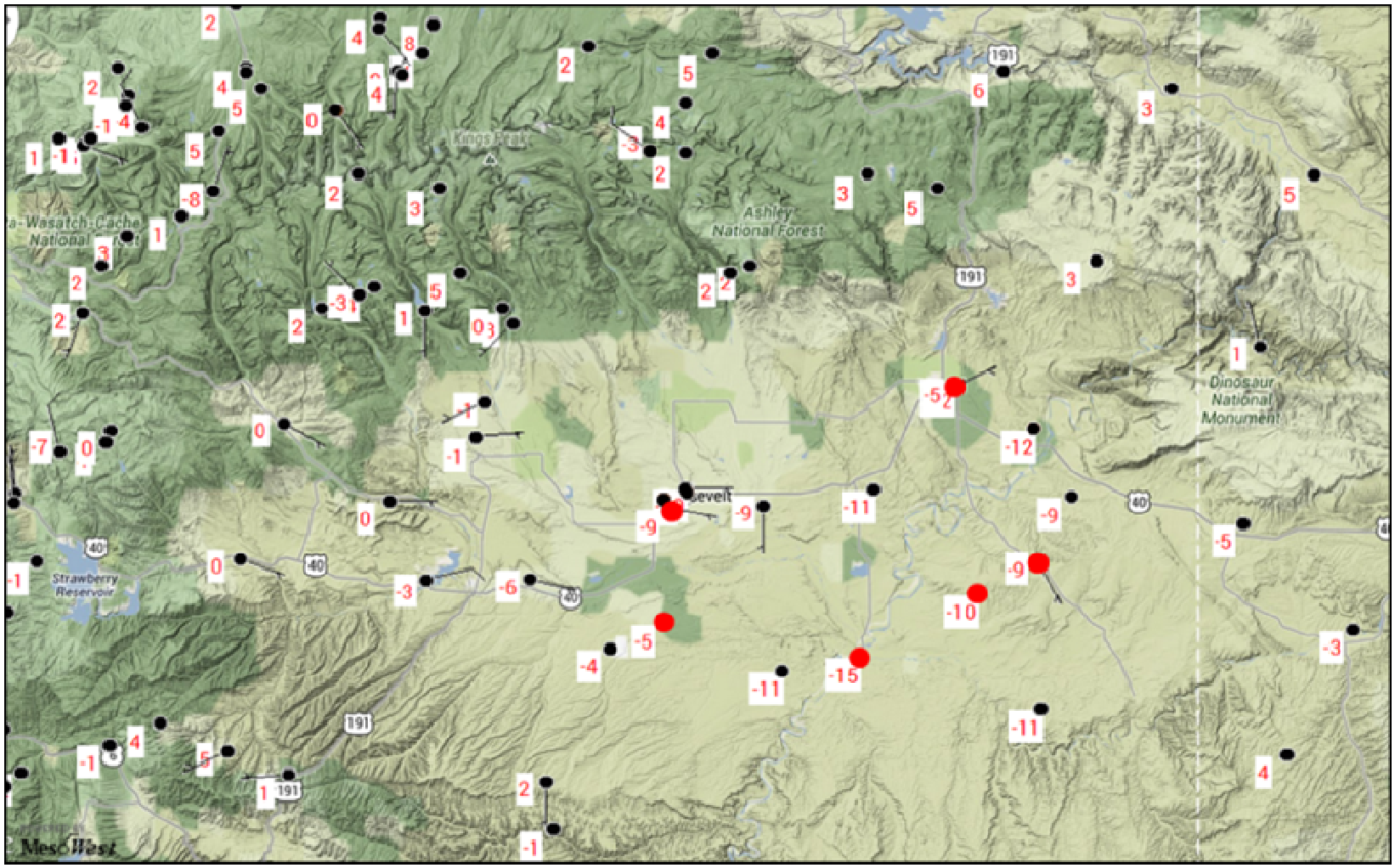

Fig. 2.1: Surface observations near the Uintah Basin at 1800 UTC on 2 February 2013. Air temperature (°C) plotted to the lower left of the station location (black dots). Red dots indicate locations used for model validation.

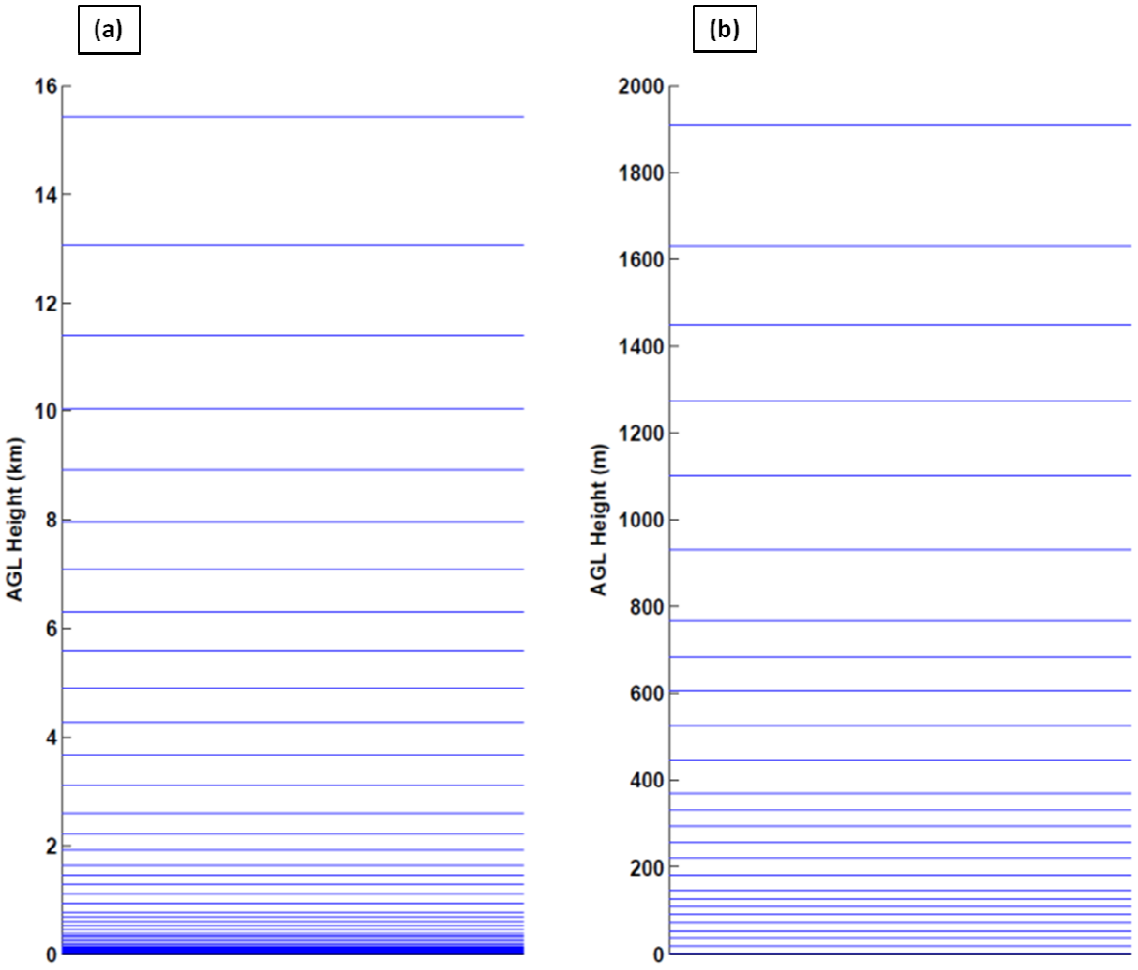

Fig. 2.2: WRF vertical model level setup. The bottom of model levels are plotted for (a) entire model domain (in km) and (b) lowest 2 km of domain (in m).

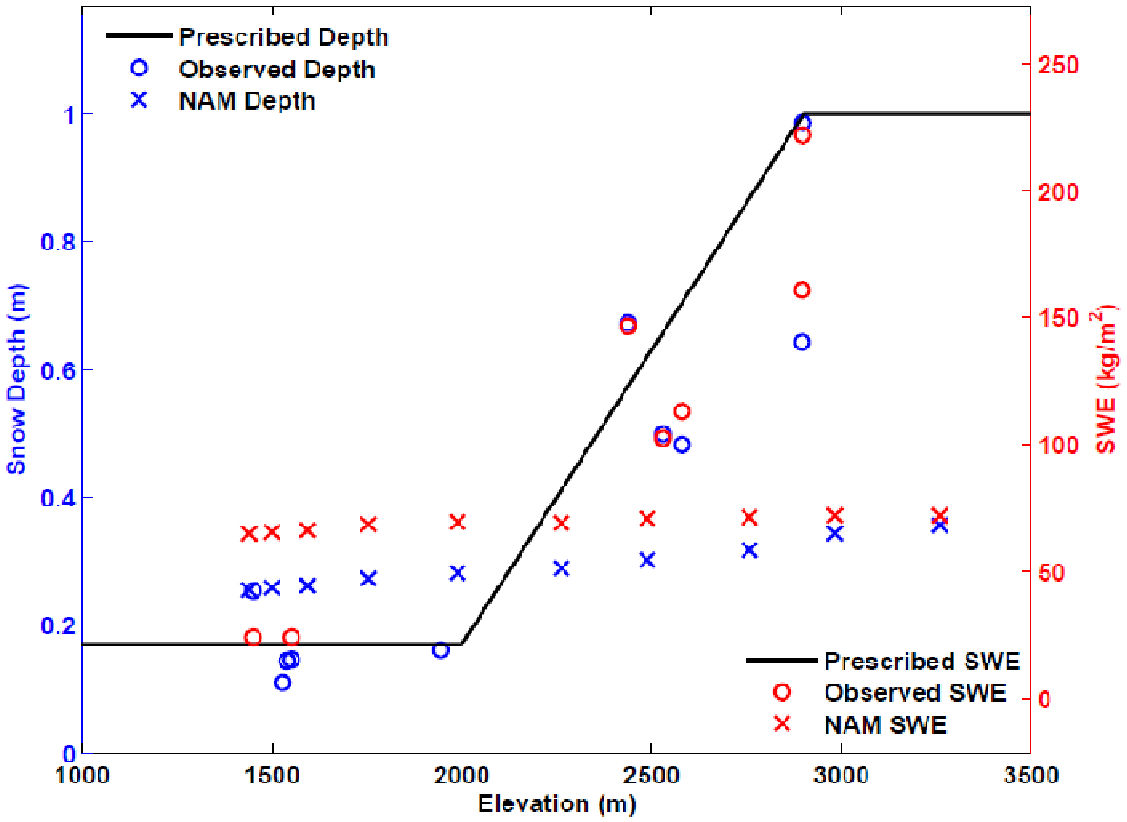

Fig. 2.3: Snow depth (blue) and snow water equivalent (red) as a function of elevation for 0000 UTC 1 February 2013 for: prescribed snow applied to WRF simulations (black line); observations (O) from the Uintah Basin and surrounding mountains; and NAM analysis (X). NAM analysis data were extracted along a southeast to northwest transect from the center of the basin to the center of the Uinta Mountains.

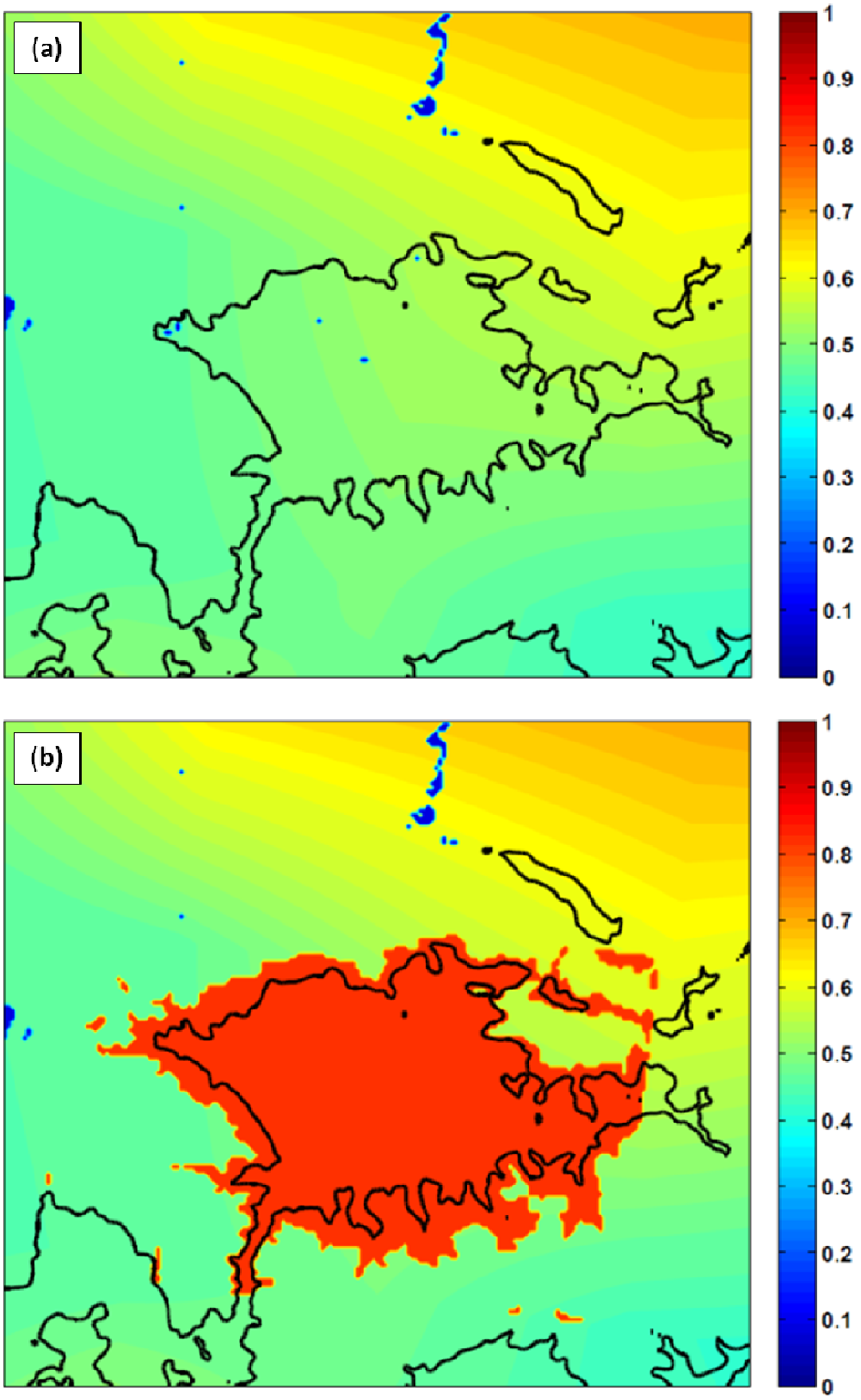

Fig. 2.4: WRF snow albedo variable at 0100 UTC 01 February 2013 for (a) before and (b) after modifications to the model.

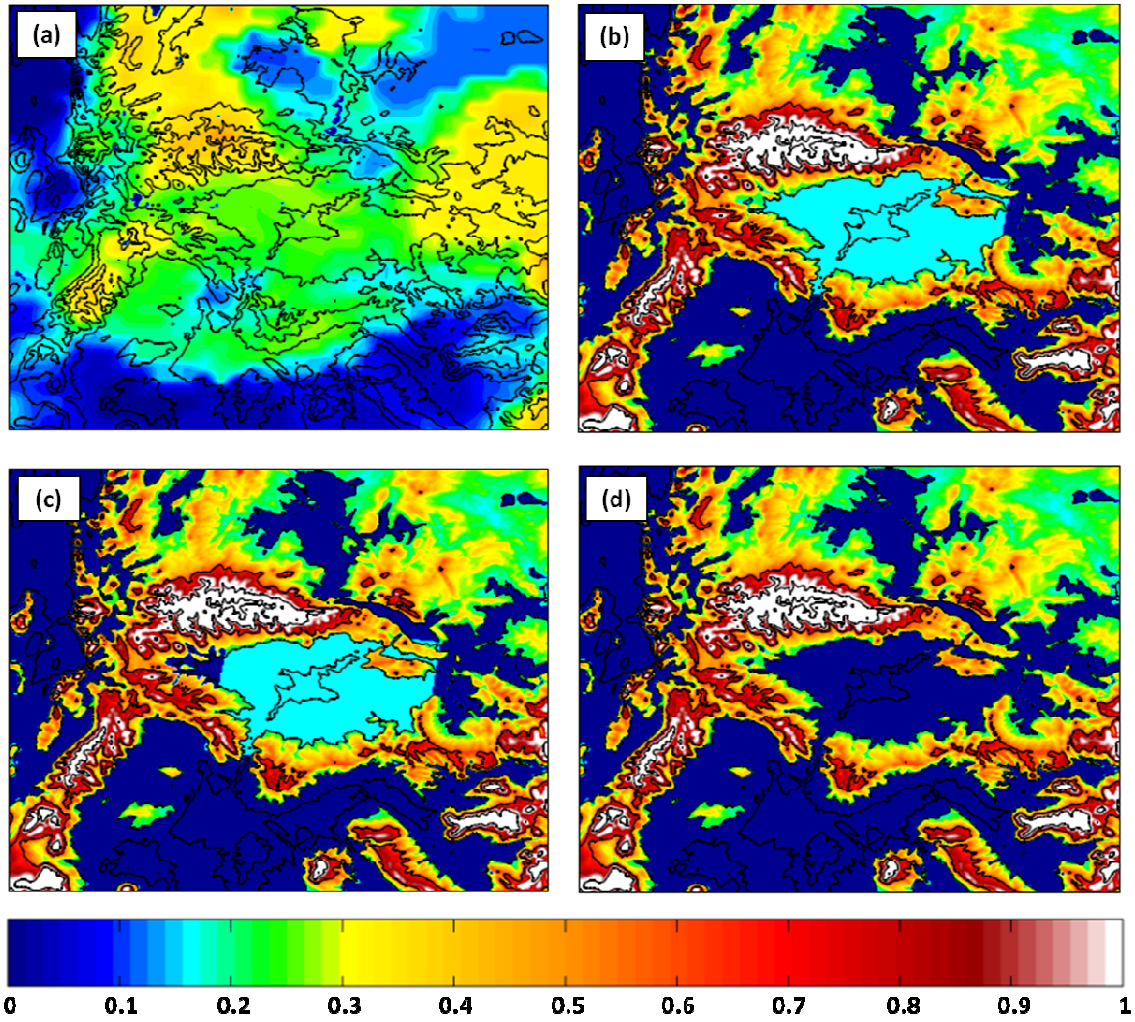

Fig. 2.5: Snow depth from (a) NAM analysis at 0000 UTC 01 February 2013, (b) "Full Snow" cases (BASE/FULL), (c) "No Western Snow" case (NW), and (d) "No Snow" case (NONE).

Table 2.1: Summary of WRF setup and parameterizations.

Parameter	**Chosen Setup**	**Reference**
Initial/Boundary Conditions	NAM Analysis	
Vertical Levels	41	
Domains	3 one-way nests	
Resolution	12 km, 4 km, 1.33 km	
Time Step	45 s, 15 s, 5 s	
Microphysics	Thompson	Thompson et al. 2008
Shortwave Radiation	RRTMG	Iacono et al. 2008
Longwave Radiation	RRTMG	Iacono et al. 2008
Boundary Layer	Mellor-Yamada-Janjic (MYJ)	Janjic 1994
Surface Layer	Eta Similarity	
Land Surface	Noah	Chen and Dudhia 2001
Cumulus	Kain-Fritsch (12 km domain only)	Kain 2004
Diffusion	2nd order on coordinate surfaces	

Table 2.2: Overview of WRF sensitivity studies.

	Snow Cover	Cloud Ice Sedimentation	Cloud Ice Auto-conversion to Snow	Simulation Name
Microphysics Sensitivity Simulations	Full Snow in basin	ON	ON	BASE
	Full Snow in basin	OFF	OFF	FULL
Snow Cover Sensitivity Simulations	No Snow below 2100 m in western 1/4 of basin	OFF	OFF	NW
	No Snow below 2000 m in basin	OFF	OFF	NONE

CHAPTER 3

RESULTS

3.1 Overview

The numerical sensitivity simulations presented in this chapter investigate the role of snow cover and boundary-layer clouds on the intensity and vertical structure of the 1–6 February 2013 CAP. The focus lies on the vertical profiles of temperature, wind, and moisture within the first km above the surface since there is little sensitivity to snow cover and low clouds at higher levels. In addition, pollutant mixing depth and transport within the CAP depends on the atmospheric stability and flows in the lowest km above the surface. A common limitation of many air quality modeling studies is an over-reliance on surface wind observations at scattered locations to validate the advective fluxes of pollutants within CAPs (L. Avey, Utah Division of Air Quality, personal communication 2014).

This chapter is organized as follows: First, an overview of the observed evolution of the 1–6 February 2013 CAP in the Uintah Basin is presented in Section 3.2, followed by analysis of the BASE WRF model simulation in Section 3.3. The sensitivity of the simulated CAP to variations in cloud type and snow cover are presented in Sections 3.3 and 3.4, respectively. Then, the FULL WRF model simulation is used in Section 3.5 to diagnose the mesoscale flows that may be important to pollutant transport within the

basin.

3.2 1–6 February 2013 Cold-Air Pool

A deep upper-level trough and associated midlatitude cyclone moved through the Great Basin from 28–30 January 2013, bringing very cold air aloft (700 hPa temperatures ~-20 °C) and 1–5 cm of light snowfall on top of a ~10–20 cm base across most of the Uintah Basin. Following the upper-level trough passage, 1–6 February was dominated by upper-level ridging over the western US and surface high pressure in the Great Basin (Fig. 3.1). This pattern placed northeastern Utah in a region of large-scale subsidence and midlevel warming. With warm air aloft (700 hPa temperatures between ~-7 and 0 °C), quiescent surface weather conditions, fresh snow cover, cold low-level air in place, and sufficient incoming solar insolation to drive photochemistry, the stage was set for a persistent CAP event and development of high ozone concentrations in the Uintah Basin.

The surface temperatures from -5 to -15 °C observed at 1800 UTC (11 Mountain Standard Time; MST) 2 February 2013 (Fig. 2.1) provide an indication of the extent of the cold-air trapped in the lowest elevations of the Uintah Basin during this period. Above-freezing temperatures at higher elevations were common. At this time, ice fog and low stratus were observed in the lowest reaches of the basin with relative humidity values generally in the 85–90% range (reflecting saturation with respect to ice) while values dropped to less than 50% on the slopes (not shown).

Selected vertical profiles of temperature, dew point temperature, and wind at Roosevelt from rawinsondes released daily at midday (1800 UTC) during the CAP are shown in Fig. 3.2. A shallow mixed layer with high relative humidity near the surface

(with thin ice fog and stratus observed intermittently at the time) is capped by increasing temperatures on 2 February below 840 hPa (Fig. 3.2a). The strong inversion extends upwards to 700 hPa with decreasing moisture aloft. Weak easterly winds of 2-3 m s^{-1} near 800 hPa centered within the inversion layer give way to westerly winds of ~5 m s^{-1} near the top of the inversion layer. The mixed layer is deeper on the 4th (Fig. 3.2b) with more substantive ice fog and stratus observed at the time of the launch. Weak easterly winds are present again below 800 hPa with westerly winds exceeding 10 m s^{-1} in the upper reaches of the capping inversion layer. The vertical profiles of temperature, moisture and wind show more changes between the 4th (Fig. 3.2b) and 6th (Fig. 3.2c): the inversion layer descends to 750 hPa; temperatures at 800 hPa increase by 5°C; the surface mixed layer is shallower; relative humidity drops near the surface; and the winds tend to be light and variable within the inversion.

The spatial coverage of snow and cloud on 2 February 2013 is provided in Fig. 3.3a by the snow-cloud product supplied by the NASA Short-term Prediction Research and Transition Center (SPoRT) (a section of this image was displayed previously in Fig 1.4a). This midday image depicts the lower elevations of the Uintah Basin covered in snow with less snow in its far western extremity. Fog and stratus are confined to the lowest elevations of the basin. An earlier (0931 UTC 2 February) Visible Infrared Imaging Radiometer Suite (VIIRS) nighttime microphysics RGB (red-green-blue) product from SPoRT (Fig. 3.3b) helped detect low clouds at night and discriminate particle phase by combining data from the 3.9, 10.8, and 12.0 micron infrared channels. In this image, liquid-phase low stratus and fog are represented by aqua/green colors in southern Idaho and portions of western and central Utah while the yellow/orange colors are typically

associated with ice-phase stratus and fog. The elevation dependence of the fog/stratus is evident in Fig. 3.3b by the cloud tendrils extending up the river valleys within the basin.

Figure 3.4a presents the time evolution of surface ozone at selected locations in the basin during the CAP. The concentrations exceeded the EPA standard of 75 ppb at all of these locations on many of the days. While ozone at Vernal tended to drop to background concentration levels at night, ozone at Horsepool and Ouray (one of the lowest locations in the basin) remained above the standard during nearly all hours from the 4th through the 9th.

Figure 3.4b presents the time evolution of aerosol backscatter, low clouds, and an estimate of the depth of the aerosol layer from the Roosevelt laser ceilometer during the 1–6 February period. Fewer aerosols were observed on 1 February followed that evening by the development of ice fog, evident as well in Fig. 3.3b. Then, a semiregular pattern developed over the next several days with shallow nighttime fog and low clouds thinning by midday and followed by a deeper layer of aerosols in the afternoon that quickly collapsed at sunset. The ceilometer backscatter data also corroborate other observations that the fog and low cloud occurrence in the basin peaked during 3–4 February. During that time, significant hoar frost was observed on trees and other surfaces after sunrise with light accumulations of snow crystals falling out of the ice clouds in Roosevelt later in the morning. The high levels of aerosol backscatter on 5–6 February diminished abruptly during late afternoon on 6 February as a result of a weak weather system; however, elevated ozone levels continued until 9 February, after which a stronger weather system with sufficient cold-air advection aloft to destabilize the column moved through the region.

3.3 1–6 February 2013 BASE Model Simulation

Evaluation of the BASE model simulation on the 1.33 km inner grid confirms that the WRF model captures the salient temperature, moisture and wind features of the CAP episode throughout the 1–6 February period above ~500 m AGL. For example, the simulated potential temperature profiles from the BASE simulation at elevations above that level tend to agree well with the observed midday profiles at Roosevelt (Fig. 3.5).

However, the BASE simulation exhibits unrealistically deep surface-based mixed layers midday (Fig. 3.5) and unrealistic spatial patterns in 2-m temperature (compare Fig. 3.6a to Fig. 2.1), which will both be shown in the next subsection to be related to unrealistically thick layers of liquid fog and stratus. While the simulated fog and stratus tends to dissipate during most afternoons, those clouds greatly hinder cooling overnight, disrupt the strength of the near-surface layers of the CAP, and result in subcloud mixed layers that are 2–4 times deeper than those observed and surface temperatures that are too warm (Fig 3.5).

Figure 3.7 shows the temporal evolution of the temperature bias (model – observed) computed from the 6 representative surface stations in the center of the basin that are highlighted in Figs. 1.5b and 2.1. Large warm biases are evident from the 2nd to the 5th with small or cold biases on the 1st and 6th, which leads to an overall bias of 1.7 °C when averaged over the entire simulation with a mean absolute error of 3.3 °C (Table 3.1). As will be discussed in the next subsection, the time evolution of these biases are related to the evolution of the observed cloudiness coupled with the overproduction of liquid clouds throughout the model run.

3.4 Sensitivity to Cloud Type

The default settings in the Thompson microphysics scheme used in the BASE simulation will be shown in this section to lead to dense, liquid-phase low clouds and fog that notably alter the radiation budget within the basin, and consequently, the strength of the CAP. The extensive fog and stratus, particularly during the overnight hours, result in excessive longwave radiation that inhibits low-level cooling and forms a region of warm air in the center of the basin during much of the CAP period. Although a number of modifications were evaluated (see Section 2.3), straightforward modifications to the Thompson microphysics scheme that are employed in the FULL model run make it possible to examine the sensitivity of the CAP simulations to cloud type. As detailed in Table 2.2, the FULL simulation has cloud ice sedimentation and cloud ice autoconversion to snow turned off in the lowest 15 model levels. The intent of these modifications is to force the WRF model to produce and maintain clouds dominated by ice-phase particles.

Returning to Fig 3.5, consider the differences between the midday potential temperature profiles at Roosevelt of the FULL and BASE simulations relative to the observed profiles. While the FULL profiles are not necessarily in agreement with the observed ones at all times, they tend to show lower temperatures near the surface and shallower surface-based mixed layers. As discussed in the previous section, the differences in potential temperature between the FULL and BASE simulations become small above ~500 m AGL. These differences in the vertical structure of the FULL simulation relative to the BASE simulation yield a more realistic deepening (2–4 February) and subsequent lowering (5–6 February) of the top of the shallow mixed-layer.

The 2-m temperatures at 1800 UTC 2 February from the FULL simulation (Fig. 3.6b)

are much lower in the center of the basin and appear closer to those observed (Fig. 2.1). Further, the bias and mean errors of the FULL simulation are sharply reduced relative to the 6-station sample (Table 3.1). However, both the BASE and FULL simulations develop unrealistic liquid and ice clouds, respectively, on the 1st and the 6th when clouds were not observed (Fig. 3.4b). That results in lower temperatures than observed (Fig. 3.7). Temperatures at 2-m averaged over the entire simulation period demonstrate the colder CAP produced in the FULL relative to the BASE simulation (Fig. 3.8). The difference between those two fields indicates an average decrease in temperature of ~1.5 °C throughout the interior of the basin with negligible differences elsewhere (Fig. 3.9a).

These improved 2-m temperatures are related to the change from liquid to ice cloud particles. Snapshots of the cloud characteristics at 0600 UTC 5 February (Fig. 3.10) reflect similar total cloud amounts and coverage. The BASE run is dominated by liquid-phase particles, or "cloud water" (Fig. 3.10c), while the FULL run is dominated by ice-phase particles, or "cloud ice" (Fig. 3.10d). Since the liquid clouds produced in BASE are generally stratus while the ice clouds produced in FULL are primarily surface-based fog, occasionally periods of greater horizontal cloud coverage are found in BASE as the stratus is able to extend outwards away from the center of the basin. Considering that the sedimentation of cloud ice is turned off in the FULL simulation, there is greater cloud mass in that run relative to the BASE simulation. However, the liquid clouds in the BASE run produce 70–80 W m^{-2} of downwelling longwave radiation, while the ice clouds in the FULL run produce only 40–70 W m^{-2} over the same region at the same time, despite the extra cloud mass (compare Fig. 3.10e to Fig. 3.10f).

Averaged over the entire 6-day period, downwelling longwave radiation from the

liquid clouds is 10–20 W m^{-2} more than from the ice clouds (Fig. 3.9b), which is consistent with the elevated temperatures over the entire period as well (Fig. 3.9a). The greatest difference in 2-m temperature is at the low elevations in the center of the basin, while the greatest difference in longwave radiation is midway up the basin slope along the periphery of cloud cover. Table 3.2 demonstrates this behavior with mean differences calculated below specified elevations within the basin. Hence, the stratus clouds in the BASE simulation typically had greater spatial coverage than the ice fog in the FULL run, which leads to larger differences in longwave radiation in locales where liquid clouds are present and ice clouds are not.

3.5 Sensitivity to Snow Cover

3.5.1 No Snow

As mentioned in the Introduction, the lack of snow during the 2012 winter led to high surface temperatures, deep afternoon mixed layers, and low ozone concentrations (Lyman and Shorthill 2013). We examine the impact of snow cover by comparing a simulation for the 1–6 February 2013 period with no snow below 2000 m (NONE) to the FULL simulation. Returning to Fig. 3.5, the lack of snow raises the midday surface temperatures by as much as 10 °C and the depth of the mixed layer is much greater than that observed during February 2013. The differences in potential temperature at Roosevelt tend to become negligible above a few hundred meters from the surface. As a further example, potential temperature profiles from the FULL and NONE simulations are plotted at Ouray from 0900 UTC to 1800 UTC on 3 February (Fig. 3.11). Extensive tethersonde observations at this location help to provide an indication of the boundary

layer structure there during the day (Schnell et al. 2014). Potential temperatures are ~7 K warmer in NONE in the lowest 500 m (not shown). However, even the FULL simulation fails to capture the extremely cold and shallow mixed layer observed on this day.

Not surprisingly, the 2-m temperature biases relative to the 6 surface stations are very large, particularly at night, with the average difference for the 6-day period being 7.6 °C (see Fig. 3.7 and Table 3.3). In addition, the mean 2-m temperatures from the NONE simulation are much higher than those apparent from the BASE or FULL simulations (Fig. 3.8).

Several interrelated processes contribute to the higher low-level temperatures in the NONE simulation relative to the FULL simulation. First, when the snow is removed from the basin floor, the thermal conductivity of the land surface increases, and the decrease in surface albedo results in greater absorption of solar radiation. These combined land surface effects lead to a warmer boundary layer. Second, the sensitivity of the CAP to ice-phase microphysics is minimized in the NONE simulation since the warmer boundary layer over the bare ground/vegetation is too warm (i.e., higher than -12 °C) to nucleate cloud ice. Finally, liquid-phase stratus develops in the NONE simulation as opposed to ice-phase fogs overnight, which leads to higher temperatures due to increased longwave radiation at the surface.

Figure 3.12 contrasts the simulated time evolution of the CAP at Horsepool from the BASE, FULL, and NONE simulations. The strong capping inversion effectively constrains the thermal and stability differences to lie beneath it. The FULL simulation clearly has a colder, shallower CAP than the BASE simulation with the NONE simulation having the weakest inversion and warmest CAP. This weakened stability

allows further eastward penetration of downsloping westerly flow from the Wasatch Range into the western periphery of the CAP (not shown).

3.5.2 No Western Snow

A simulation with snow removed from the western corner of the basin (NW) was completed to emulate situations where downsloping westerly flow has melted the snowpack there, similar to the conditions during early February 2014. The removal of snow cover in the NW simulation proved to have very little impact on the overall CAP structure, e.g., modeled 2-m temperatures and vertical structure within the PBL in the basin's core show strong similarities to those in the FULL simulation (see Figs. 3.5, 3.7, 3.8). Temperatures at 2-m are, on average, within ~0.2 °C of FULL (Table 3.3). Nonetheless, differences in 2-m temperatures are detected near the snow boundary (e.g., compare Fig. 3.8b to Fig. 3.8c). The lower albedo and increased solar absorption of the region where snow is removed in the NW simulation leads to 2-m temperatures that average 2.5–3 °C higher than the same region in the FULL run while temperature differences over areas that remain snow-covered are generally less than 0.25 °C higher. These patterns hold true for both daytime and nighttime periods. As a consequence of this enhanced low-level temperature gradient, a thermally driven circulation is produced across the snow boundary (Fig. 3.13). The 10-m zonal wind component over the bare ground in the NW run is 1.5–2 m s^{-1} more negative (easterly) than the same region in the FULL simulation when averaged over the entire simulation. Furthermore, this "snow breeze" extends several km away from the snow boundary in both directions indicating that the circulation has significant horizontal extent.

3.6 Flow Features

While the observations collected during the UBWOS field campaigns are the most extensive available to date for studying the thermodynamic and dynamic conditions in the Uintah Basin (Lyman and Shorthill 2013; Stoeckenius and McNally 2014), the majority of them consist of enhanced surface observations throughout the basin combined with limited profiles at a few locations (e.g., Horsepool, Ouray, and Roosevelt). While far from adequately resolving CAP characteristics, the FULL simulation provides additional information on the four-dimensional fields of temperature, wind, and moisture that helps identify relevant physical processes. Several flow features were detected in the FULL simulation that could be partially validated using the limited available data that likely play an important role to transport pollutants within the CAP and ultimately affect air quality.

3.6.1 Clean-Air Intrusions into the Basin

The structure of the CAP varies extensively over the course of the FULL simulation. As shown in the potential temperature time-height plot at Horsepool (Fig. 3.12b), the 280–282 K isentrope range helps define the upper limit of the CAP. The cross sections in Fig. 3.14 (which are along the path outlined in Fig. 1.5b) suggest that the CAP is initially confined to elevations below 1800 m MSL (Fig. 3.14a). The CAP then deepens through the day on 2 February to a base near 2000 m at 0600 UTC 3 February (Fig. 3.14b) before settling below 2000 m by 1800 UTC 4 February (Fig. 3.14c). The CAP then lowers back down to ~1800 m by 0000 UTC 6 February through the end of the simulation (Fig. 3.14d).

The CAP is continually modulated by synoptically-driven midlevel flow atop the CAP, forcing it to "slosh" back and forth within the basin. Ridging aloft can lead to flow surmounting the surrounding terrain from nearly every direction from the southwest to the north. Downsloping flows mixing higher potential temperature and cleaner air downward into the basin are common and their impact depends on the stability and strength of the flow across the upwind barriers. For example, when the cross-barrier flow had a northerly component across the high Uintah Mountains during the 2013 winter, a notable strengthening of the inversion top due to subsidence warming of flow descending in the lee of the mountains was evident in the Uintah Basin (not shown).

The CAP may become displaced or tilted through hydrostatic and dynamic processes, which can then be disrupted by changes in wind speed above the CAP (Lareau and Horel 2014). These disruptions may produce a gravity current-like behavior as the CAP rebounds, causing relatively large changes in depth (a few hundred meters) within just a few hours. Figure 3.15 shows an example of this behavior. Strong westerly flow crossing the mountain barrier to the west of the basin at 0600 UTC 4 February is highlighted by a narrow band of increased westerly to northwesterly flow at 2300 m MSL over the western portion of the basin (Fig. 3.15a). The cross section of potential temperature from west to east through the center of the basin at the same time is shown in Fig. 3.15b. The westerly downslope winds have eroded and tilted the CAP, pushing it east of Starvation Reservoir (vertical line labeled "STA" in Fig. 3.15b). The CAP is depressed to ~1750 m in the western basin, much lower than in the eastern half of the basin. The FULL simulation suggests that weakening westerly winds over the next several hours lead to the CAP rebounding westward past Starvation Reservoir with the

inversion base quickly rising to ~1900 m, roughly level with the rest of the basin (Fig. 3.14c).

3.6.2 East-West Cross Basin Transport

Easterly flow immediately above the shallow mixed layer is evident in the midday soundings at Roosevelt on a number of days (Fig. 3.2). The ceilometer data at Roosevelt (Fig. 3.4) as well as ozone tethersonde observations at Ouray (Schnell et al. 2014) suggest that aerosols, ozone precursors, and ozone extend upward into this layer of easterly flow, likely as a result of weak turbulence and entrainment (Cai and Luhar 2002; Salmond 2005). The ozone precursors from eastern basin source regions that are able to leak into the easterly flow layer may then be transported westward to portions of the basin that have more limited precursor sources, which allows ozone production to take place more widely (Karion et al. 2014).

Figure 3.16a shows the time-averaged zonal wind component for the entire 6-day simulation along the cross section shown in Fig. 1.5b. Synoptic westerly flow dominates above 2200 m MSL with easterly flow present a few hundred meters above the basin floor. The core of the easterly flow coincides with the strongest stability in the basin and lies between 1800–2000 m MSL. Although this feature is relatively weak (~0.5 m s^{-1}), it is persistent enough to appear as a coherent spatial pattern when averaged over the 6-day period. Even weaker flow is noted in the lowest 100 m above the basin floor within the CAP, indicating that the mean flow is near zero for that region.

The mean flow is also examined separately for daytime and nighttime periods, Figs. 3.17a and 3.18a, respectively. During the day, the core of the easterly flow is more

intense aloft (~1 m s^{-1}), and the west-east spatial extent is greater (compare Fig. 3.16a to Fig. 3.17a). At night, the easterly flow exhibits a weaker and more regional core shifted to the eastern portion of the basin and extending down to the surface (Fig. 3.18a).

3.6.3 Diurnal Valley and Slope Flows

Figures 3.17 and 3.18 suggest both additive and destructive interactions between the cross-basin elevated easterly flows and near-surface daytime upvalley/upslope and nighttime downvalley/downslope flows. While basin-scale thermal gradients likely drive the elevated easterly flow, those gradients are at times in concert with and at other times interfering with more localized thermal gradients within drainages and along slopes.

During the night (Fig. 3.18a), drainage flows are evident by light westerly winds in the lowest 100 m on the west side of the basin in combination with light easterly winds on the east side. This pattern reverses during the day (Fig. 3.17a); however, the cross-basin easterlies appear to accentuate the upvalley/upslope winds at ~1800 m MSL. As with any basin or mountain range, the diurnal flow patterns within the Uintah Basin are complex, as summarized in Fig. 3.19. The mean wind direction during the day (Fig. 3.19a) highlights areas of upslope flow within the CAP where local ridgelines inside the basin affect the local flow direction. Outside of the CAP, to the north and west of the Uintah Basin, synoptic west-northwesterly flow and its interaction with local topography dominate (white vectors). This exhibits how the strong stability above the CAP is able to effectively shield the basin interior from synoptic flows, allowing for thermally-driven terrain circulations. During the night (Fig. 3.19b), drainage flows toward the center of the basin are evident.

3.6.4 Effects of Snow Cover on Terrain-Flow Interactions

The sensitivity of terrain-flow interactions to the presence or absence of snow cover in the Uintah Basin is briefly examined here. Comparison of the cross sections of time-averaged zonal winds from the no snow (NONE) and snow (FULL) simulations for the entire period, day, and night are shown in Figs. 3.16–3.18, respectively. Consistent with earlier results, the removal of snow cover only affects the near-surface atmosphere below the capping inversion. The core easterly winds in the FULL simulation were stronger and elevated slightly higher above the terrain than those in the NONE simulation (Fig. 3.16). The weaker stability within the capping inversion in the NONE simulation likely allows the synoptic-scale westerlies to extend further down and diminish the intensity of the easterly winds within the lower reaches of the inversion layer expected in NONE given the lack of snow cover. Comparable differences are evident during the day (Fig. 3.17) and night (Fig. 3.18) with weaker and lower elevation easterly flow aloft when snow cover is removed. However, the intensity of the upvalley/upslope and downvalley/downslope flows near the surface remains largely the same and is actually increased during the day on the western side of the basin in the NONE simulation.

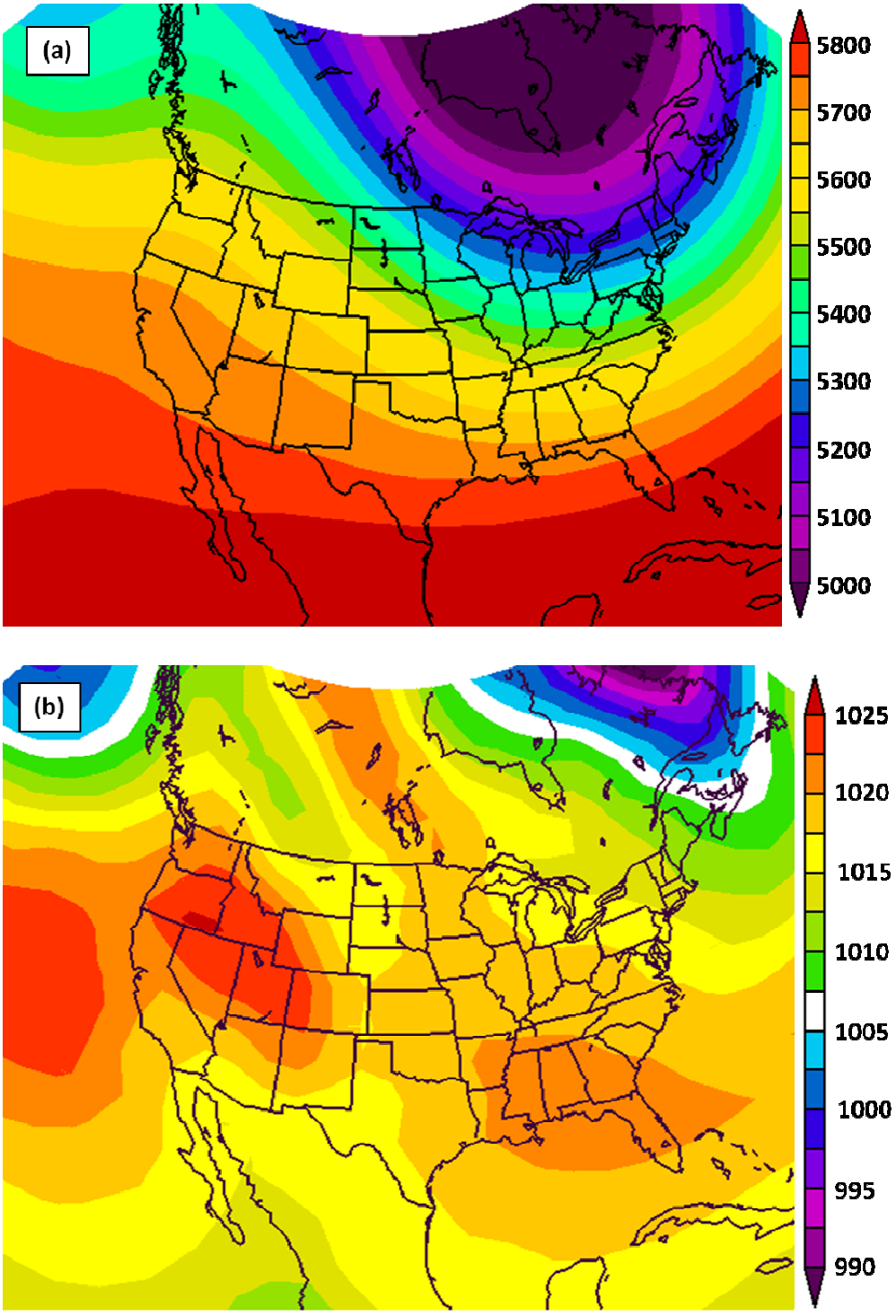

Fig. 3.1: Composite average of National Centers for Environmental Prediction (NCEP) North American Regional Reanalyses for the period from 0000 UTC 1 February to 0000 UTC 7 February 2013 for (a) 500 hPa geopotential height (in m) and (b) mean sea level pressure (in hPa). Images provided by the NOAA/ESRL Physical Sciences Division, Boulder Colorado from their Web site at http://www.esrl.noaa.gov/psd/

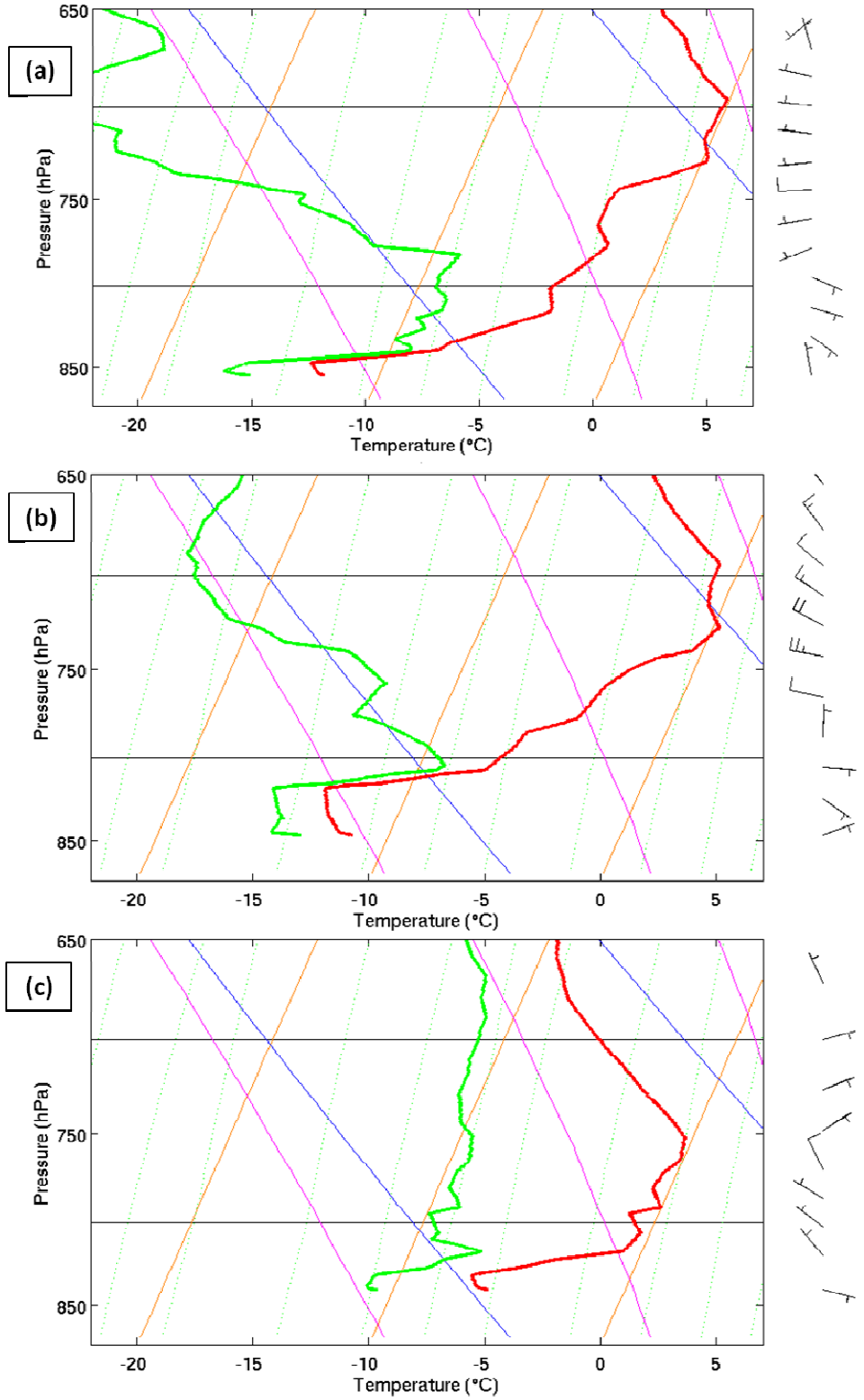

Fig. 3.2: Rawinsondes released from Roosevelt at (a) 1800 UTC 2 February 2013, (b) 1800 UTC 4 February 2013, and (c) 1800 UTC 6 February 2013. Temperature (dewpoint temperature) in red (green). Wind barbs on right side denote wind speed and direction (full barb = 5 m s^{-1}).

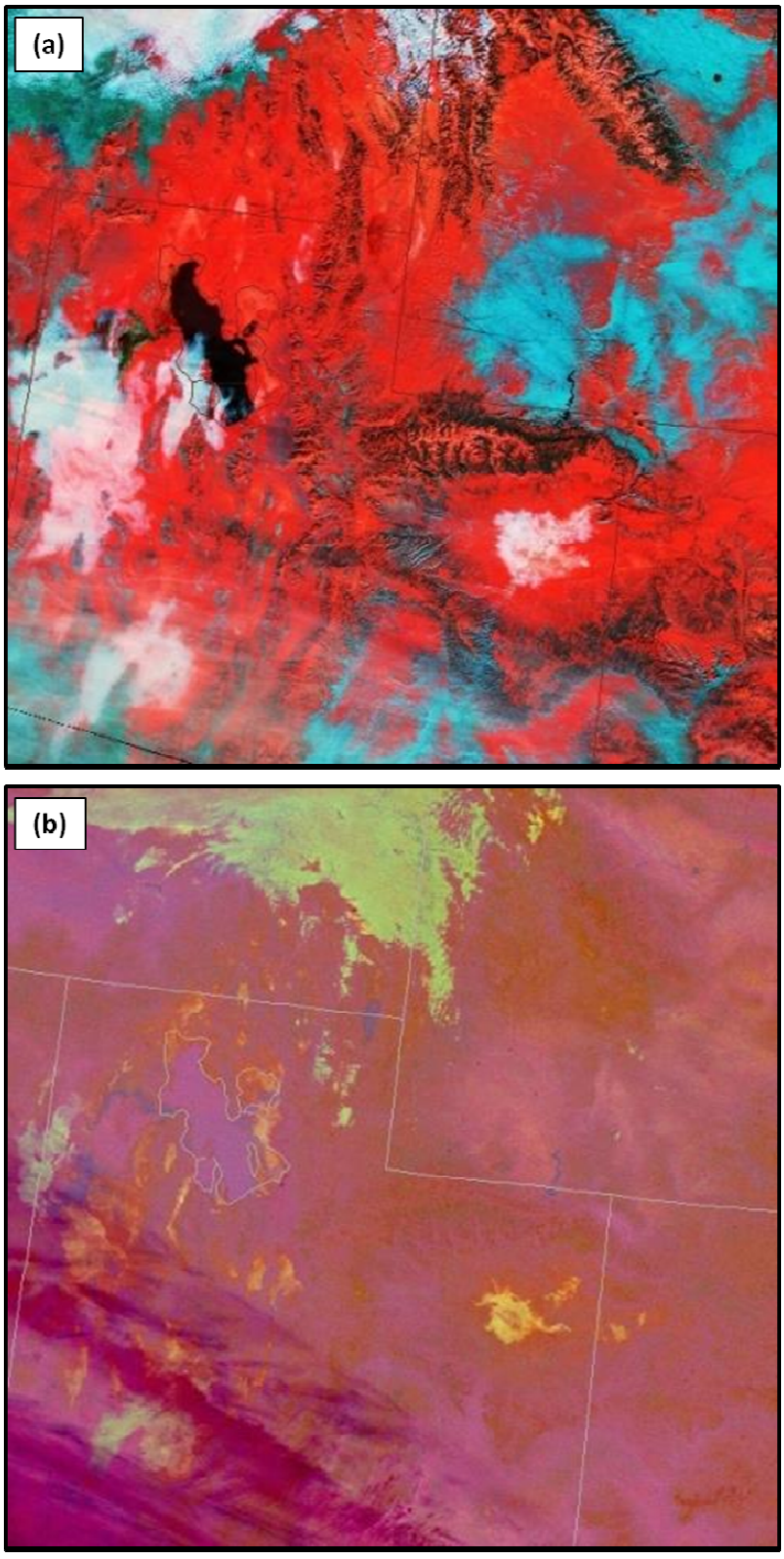

Fig. 3.3: SPoRT-derived VIIRS satellite images: (a) Snow-Cloud product at 1815 UTC 2 February 2013 and (b) Nighttime Microphysics RGB product at 0931 UTC 2 February 2013.

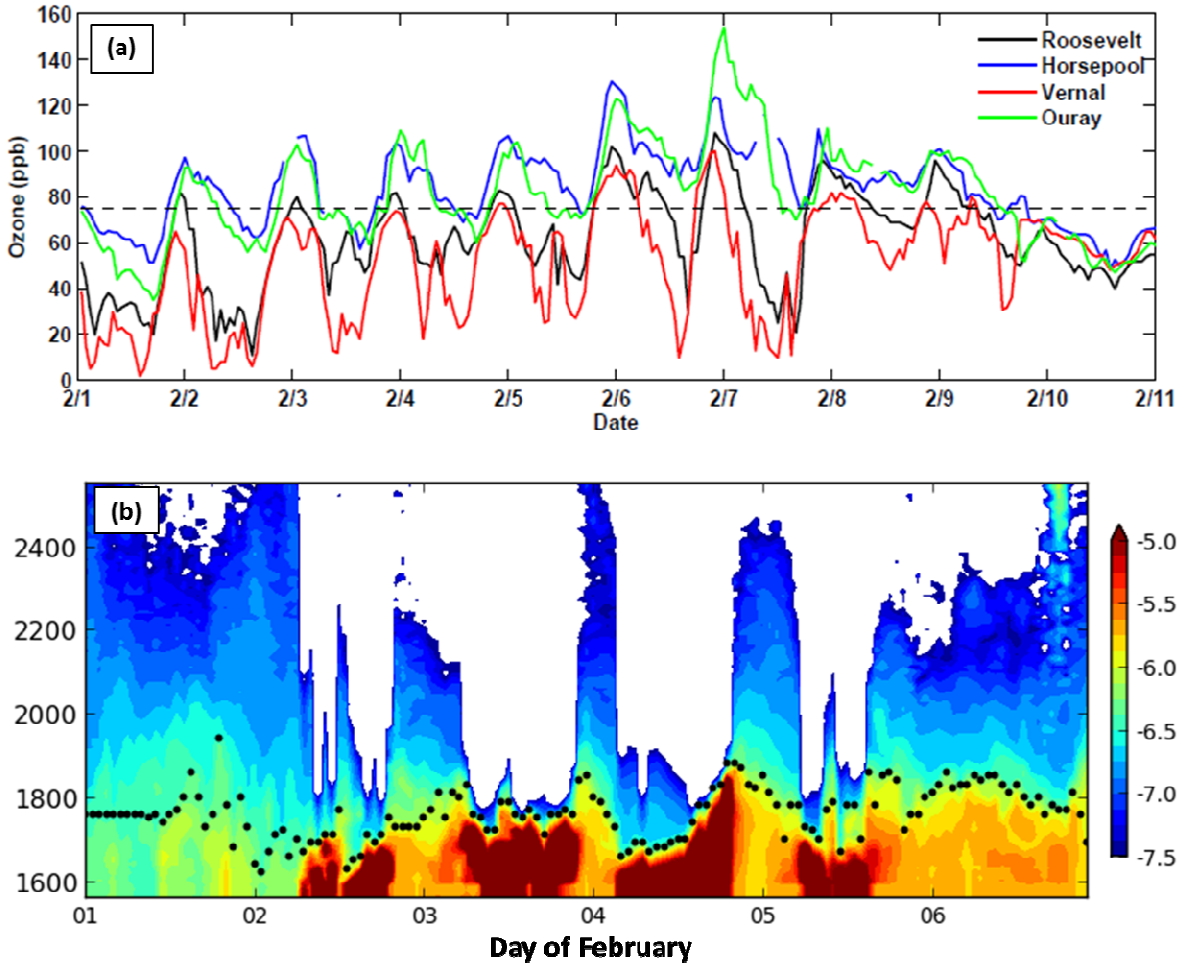

Fig. 3.4: Time series of ozone concentrations and ceilometer backscatter. (a) Hourly ozone concentrations from 1-10 February 2013 for Roosevelt (black), Horsepool (blue), Vernal (red), and Ouray (green) with the 75 ppb (8-hour mean) NAAQS denoted by the dashed line. (b) Ceilometer backscatter (shaded) and estimated aerosol depth (black dots) as a function of height (m) at Roosevelt from 1-7 February 2013. Red, yellow, blue, and white shading denote fog and stratus clouds, high aerosol concentrations; low aerosol concentrations, and beam attenuation, respectively.

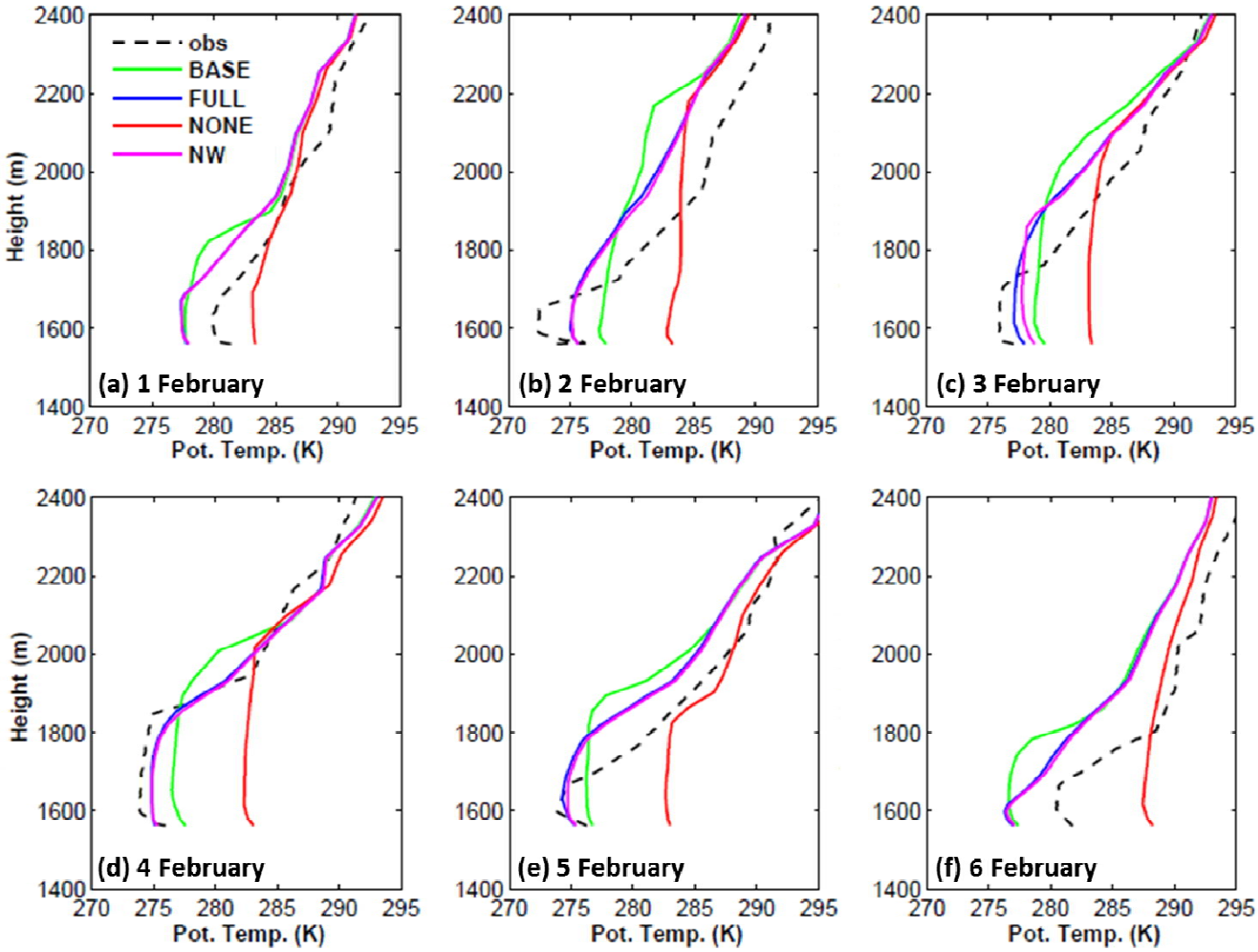

Fig. 3.5: Potential temperature profiles at Roosevelt at 1800 UTC on 1–6 February (a-f, respectively) 2013. Profiles are shown for the observed sounding (dashed black), BASE (green), FULL (blue), NONE (red), and NW (magenta) simulations.

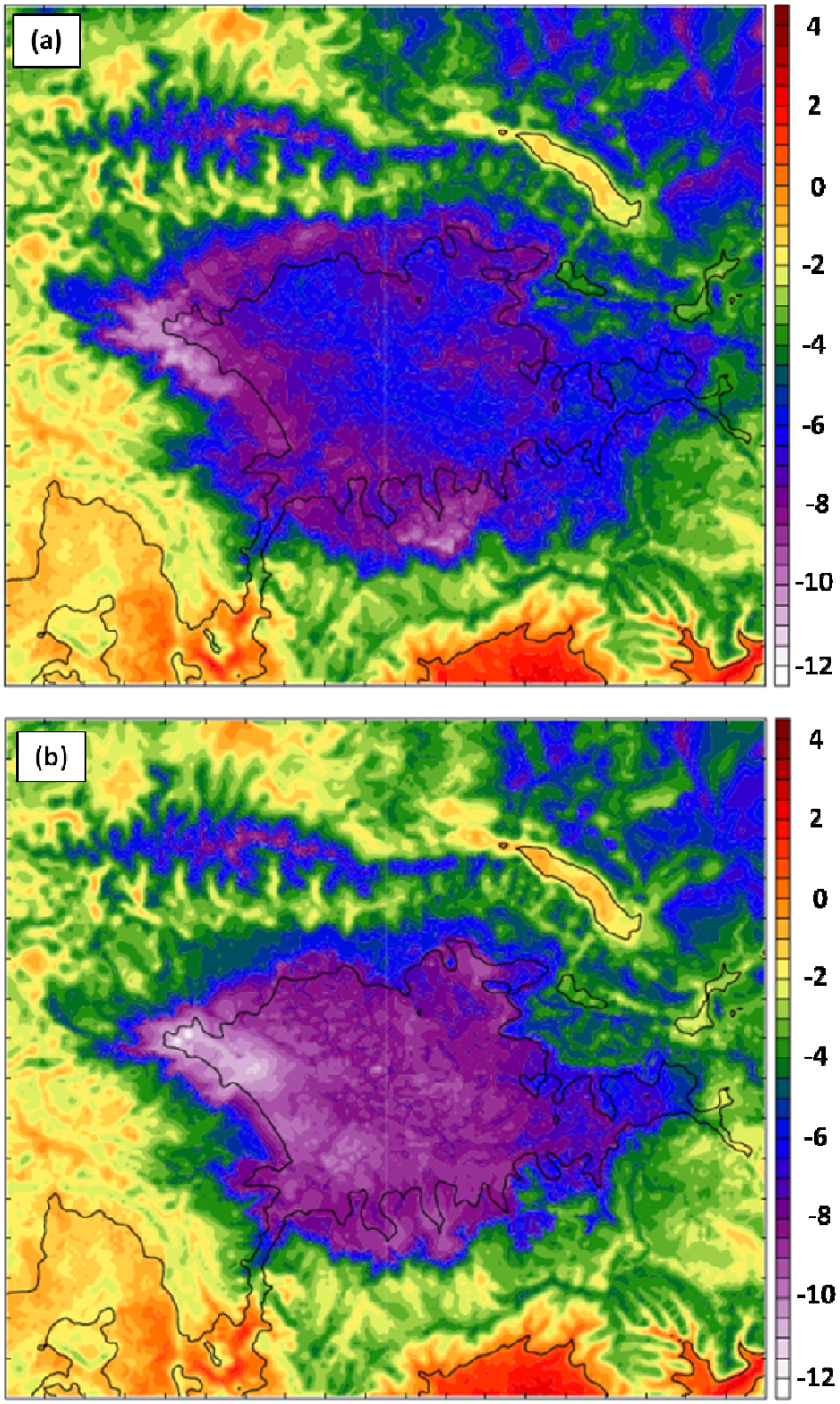

Fig. 3.6: Two-meter temperatures (in °C according to scale on right) at 1800 UTC 2 February 2013 for (a) BASE and (b) FULL simulations. Black contour indicates terrain elevation of 1800 m.

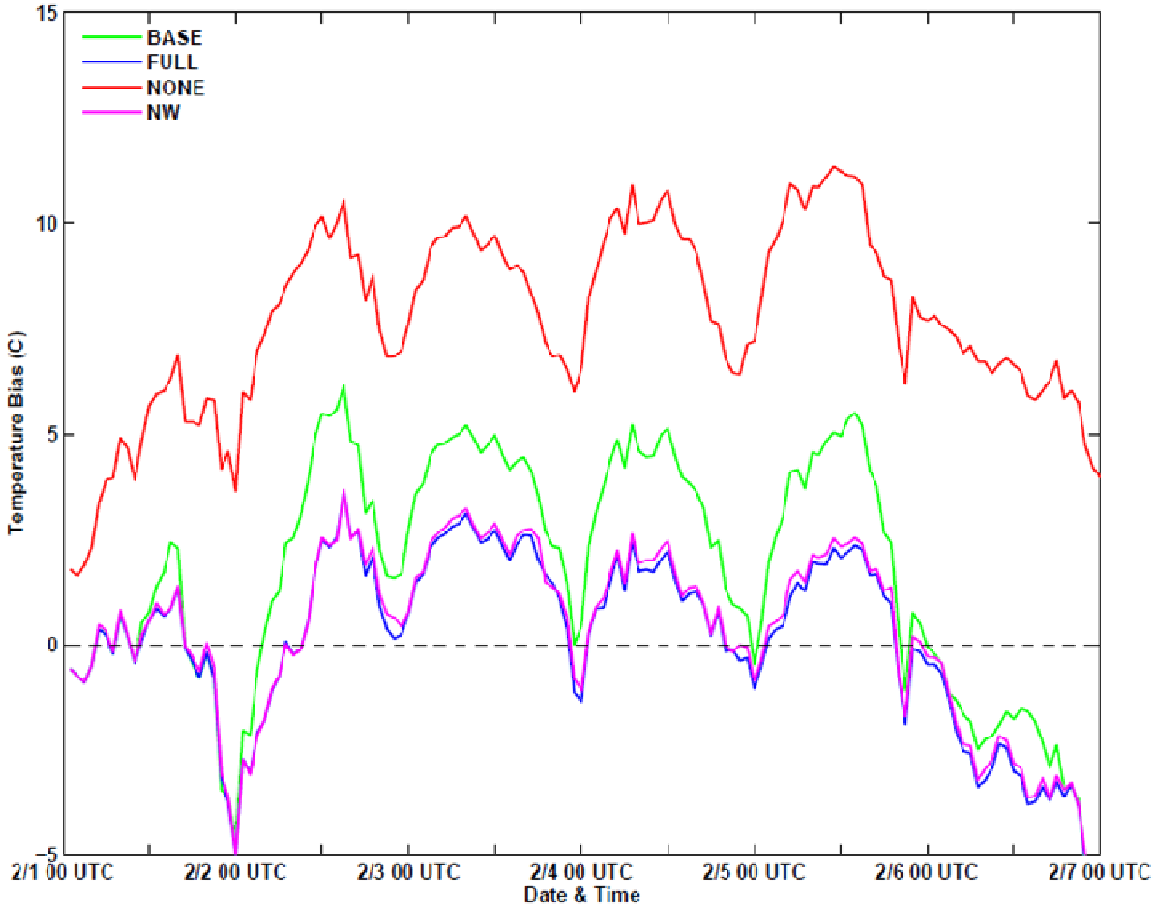

Fig. 3.7: Time series of mean 2-m temperature bias for BASE (green), FULL (blue), NONE (red), and NW (magenta) simulations. Biases are derived from averages for the 6 surface stations in Fig. 1.5b.

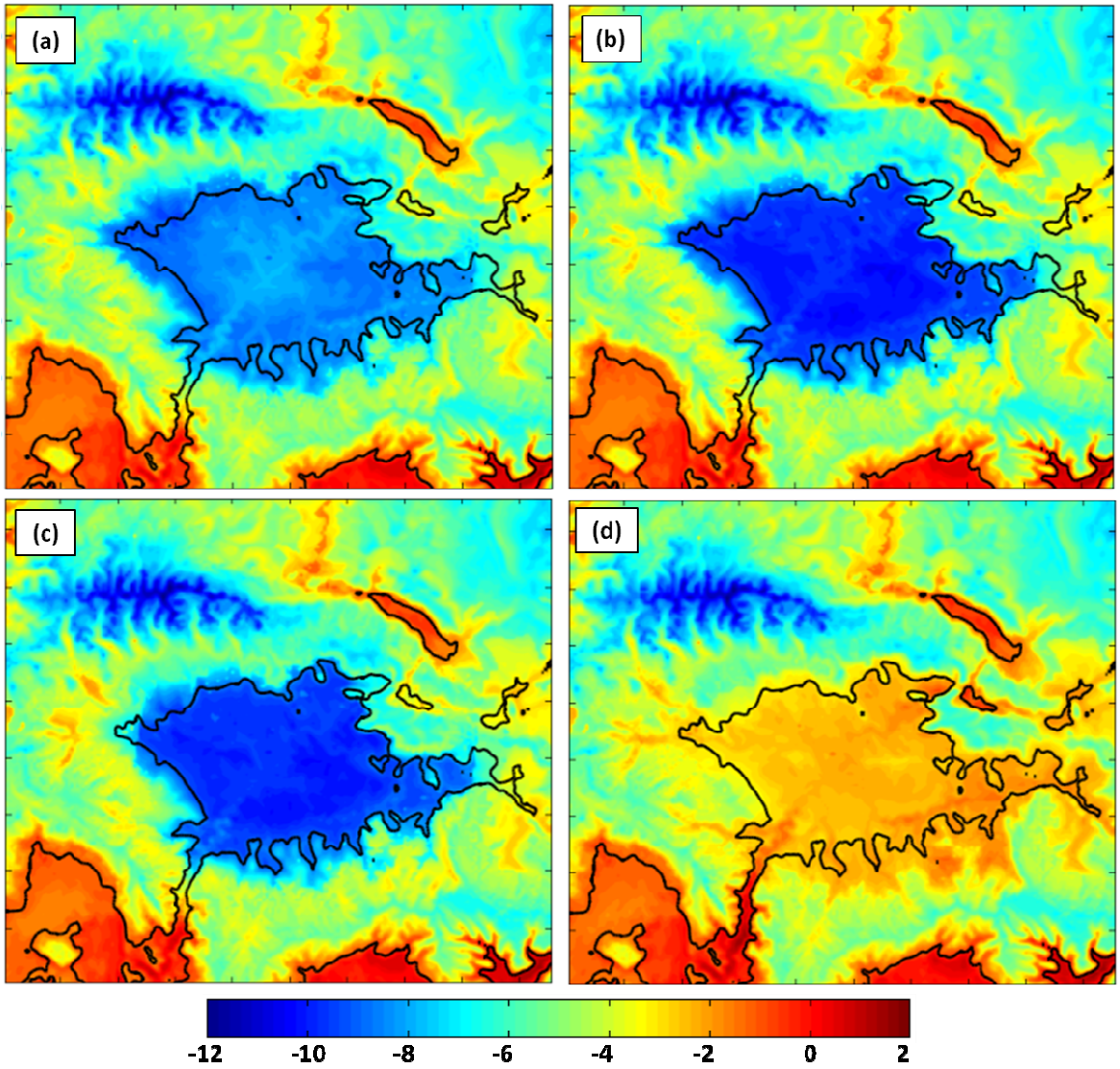

Fig. 3.8: Average 2-m temperature (in °C according to the scale below) for 1–6 February 2013 from (a) BASE, (b) FULL, (c) NW, and (d) NONE simulations.

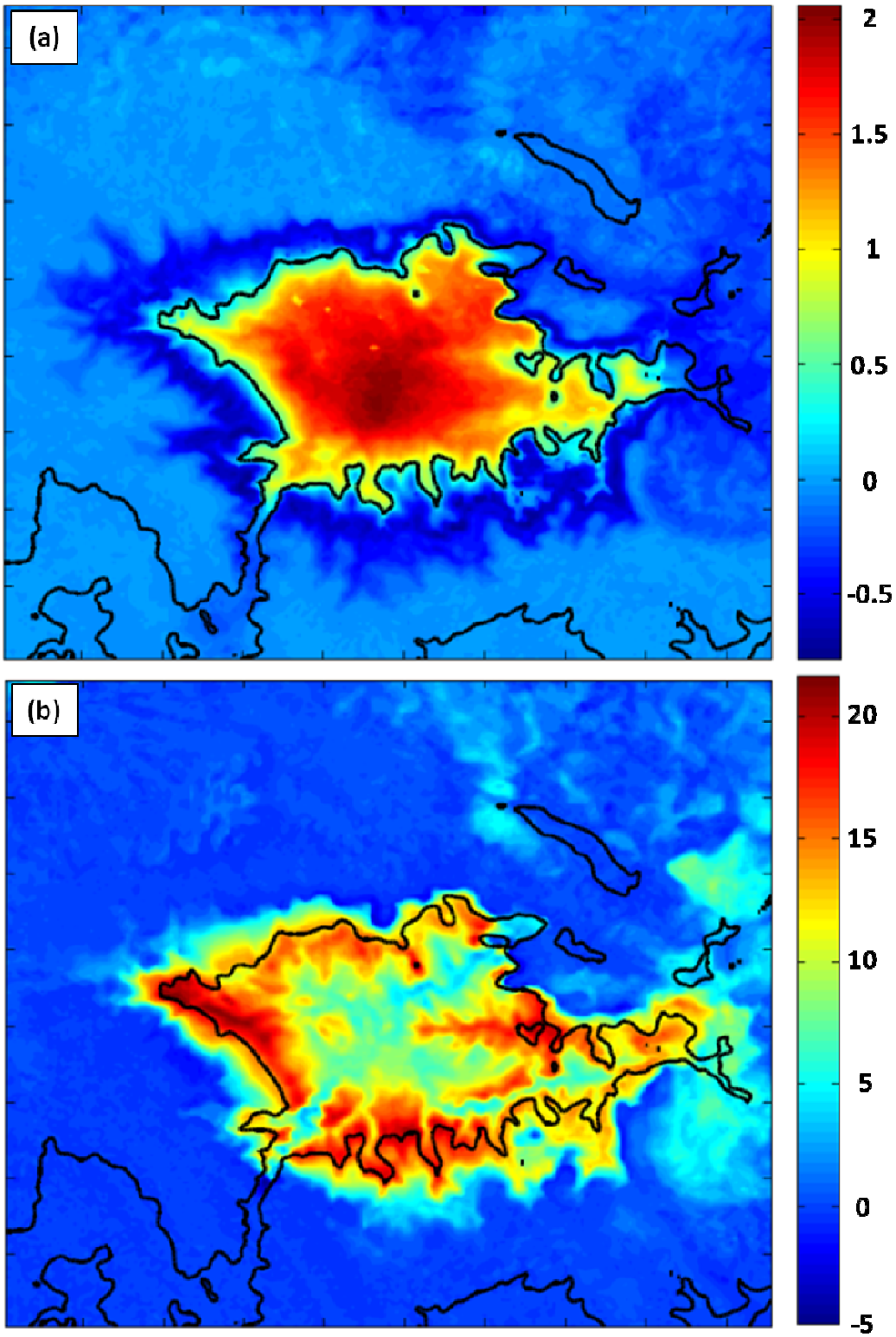

Fig. 3.9: Average difference (BASE – FULL) for 1–6 February 2013 period in: (a) 2-m temperature (in °C according to the scale to the right) and (b) downwelling longwave radiation (in W m^{-2} according to the scale on the right).

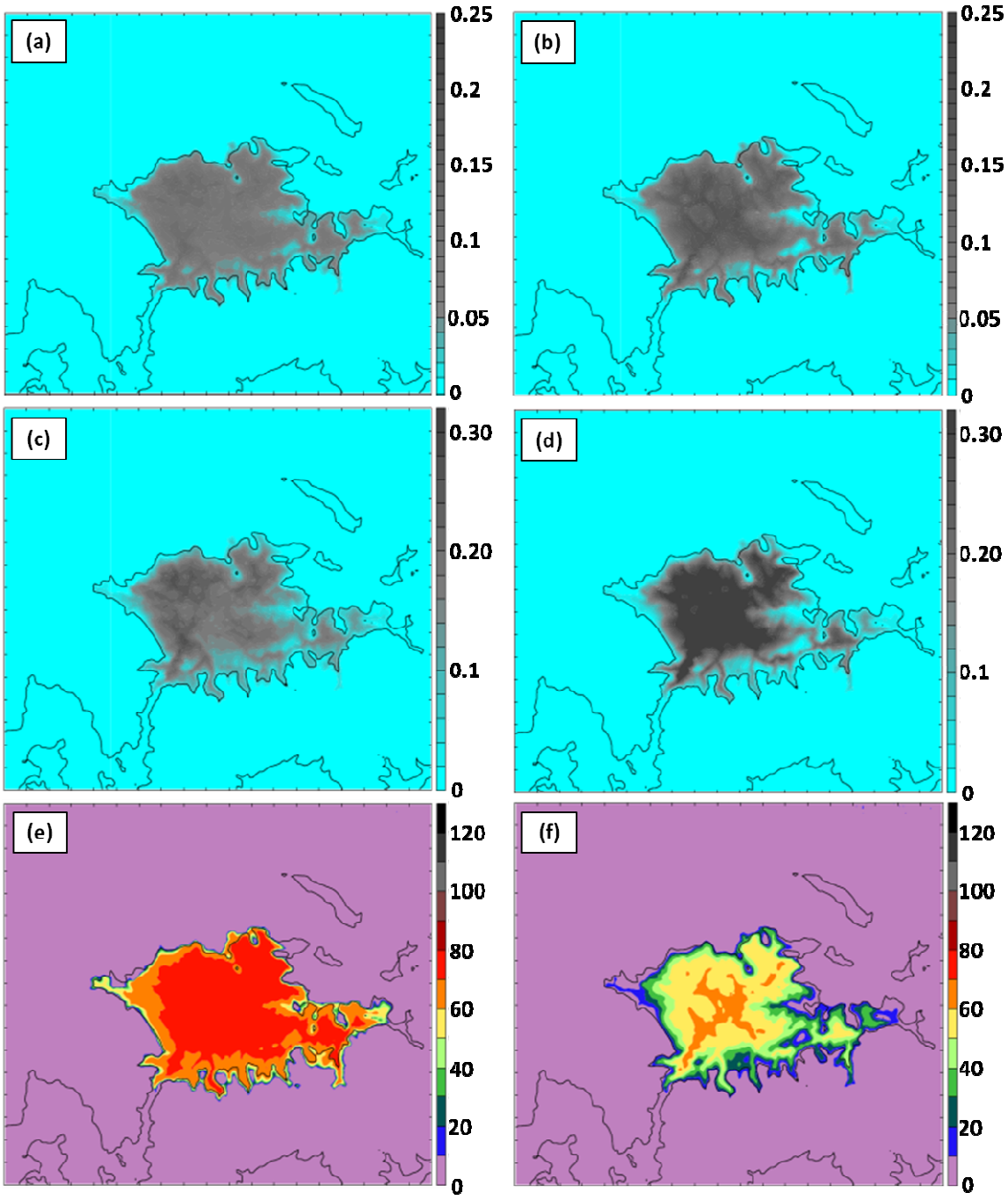

Fig.3.10: Cloud characteristics from BASE (a, c, e) and FULL (b, d, f) simulations at 0600 UTC 5 February 2013. (a, b) Integrated cloud amount (in mm according to the scale on the right), (c) mean cloud water in bottom 15 model levels (in g kg^{-1} according to the scale on the right), (d) mean cloud ice in bottom 15 model levels (in g kg^{-1} according to the scale on the right), (e, f) net downwelling longwave radiation from clouds (in W m^{-2} according to the scale on the right).

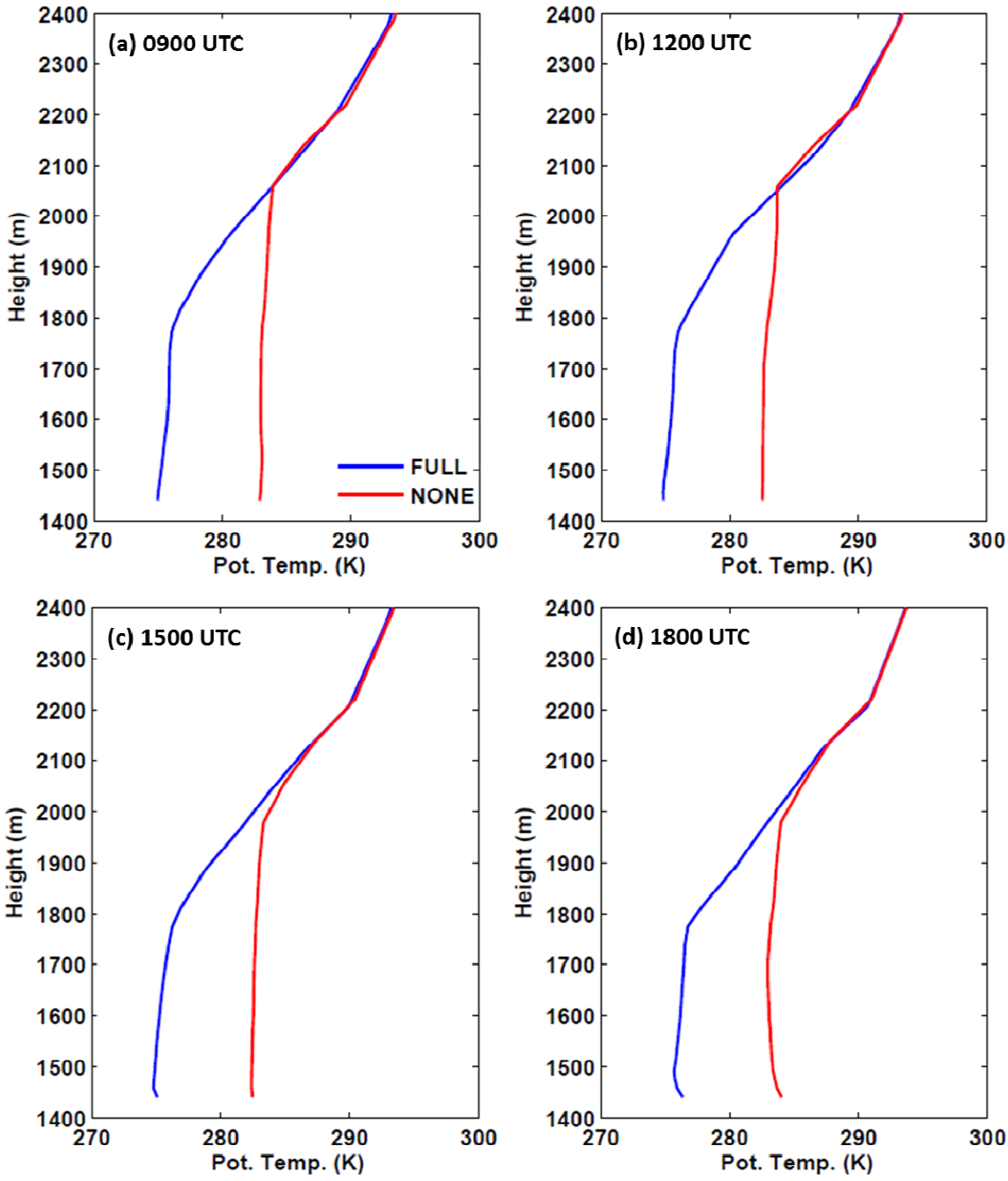

Fig. 3.11: Potential temperature profiles at Ouray on 3 February 2013 at (a) 0900 UTC, (b) 1200 UTC, (c) 1500 UTC, and (d) 1800 UTC from FULL (blue) and NONE (red) simulations.

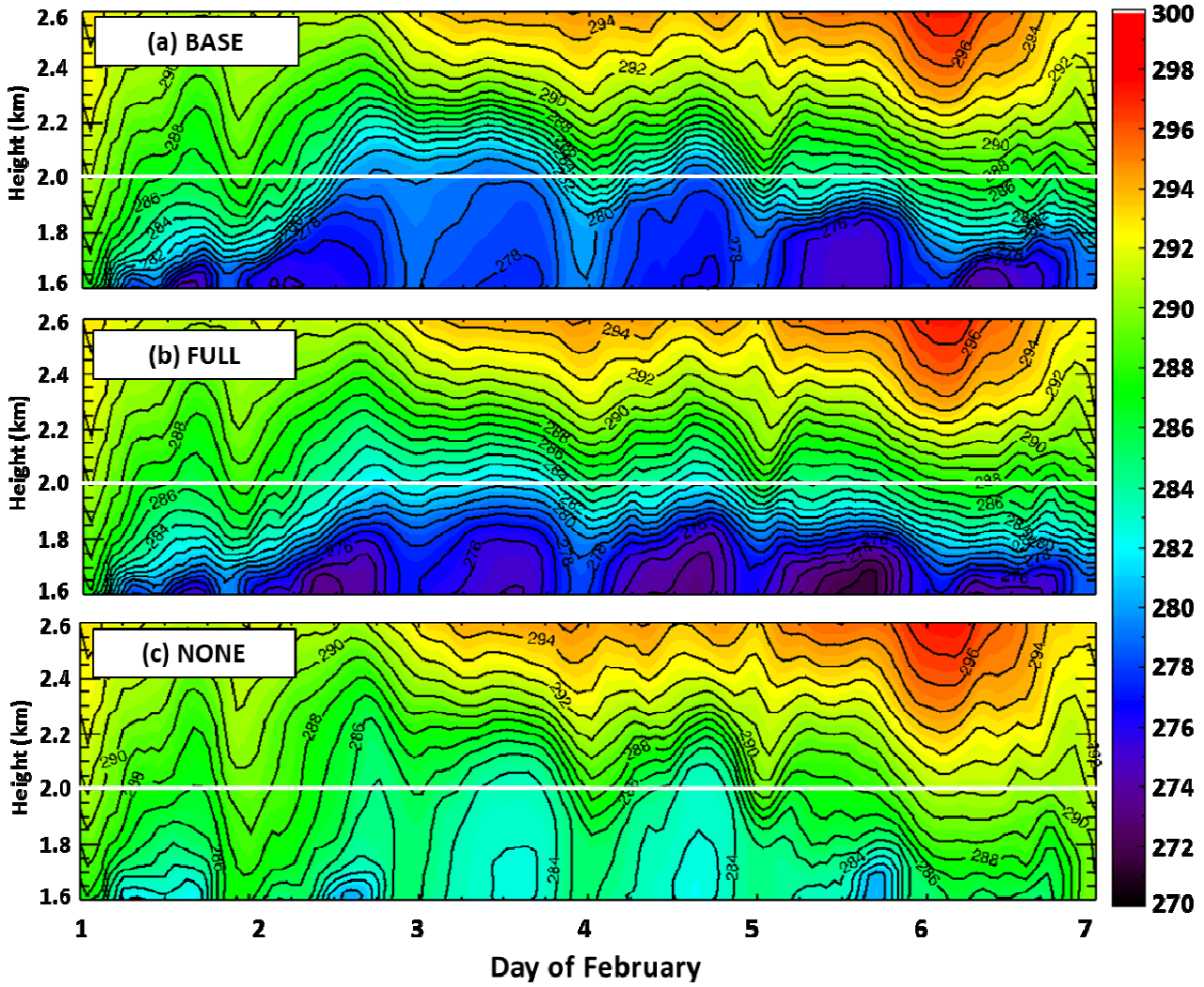

Fig. 3.12: Time-height plot of potential temperature (in K according to the scale on the right) at Horsepool from 1–6 February 2013 from (a) BASE, (b) FULL, and (c) NONE simulations.

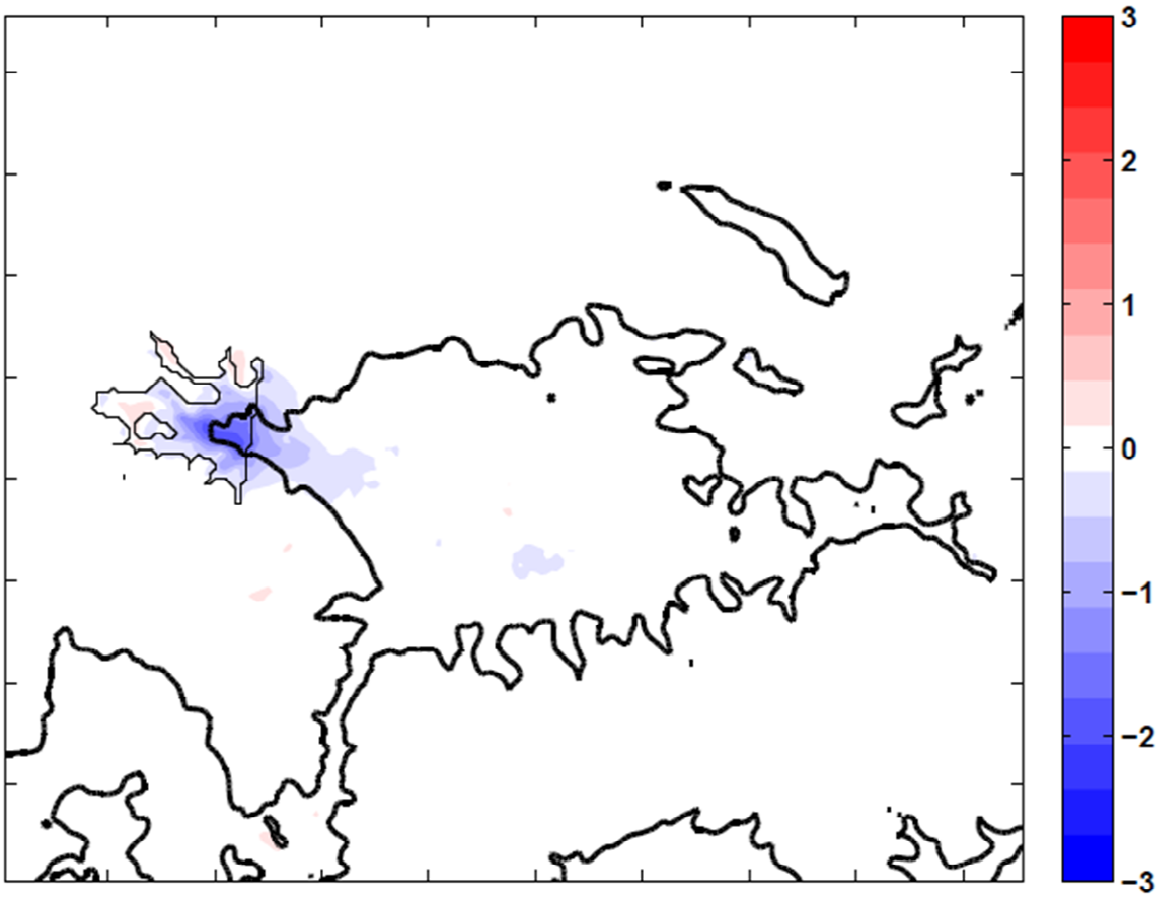

Fig. 3.13: Average zonal wind difference (in m s^{-1} according to the scale on the right) between NW and FULL simulations (NW - FULL) for the 1–6 February 2013 period. Reference terrain elevation of 1800 m shown by the heavy black line while the thin black contour delineates the region where snow is removed in the NW simulation.

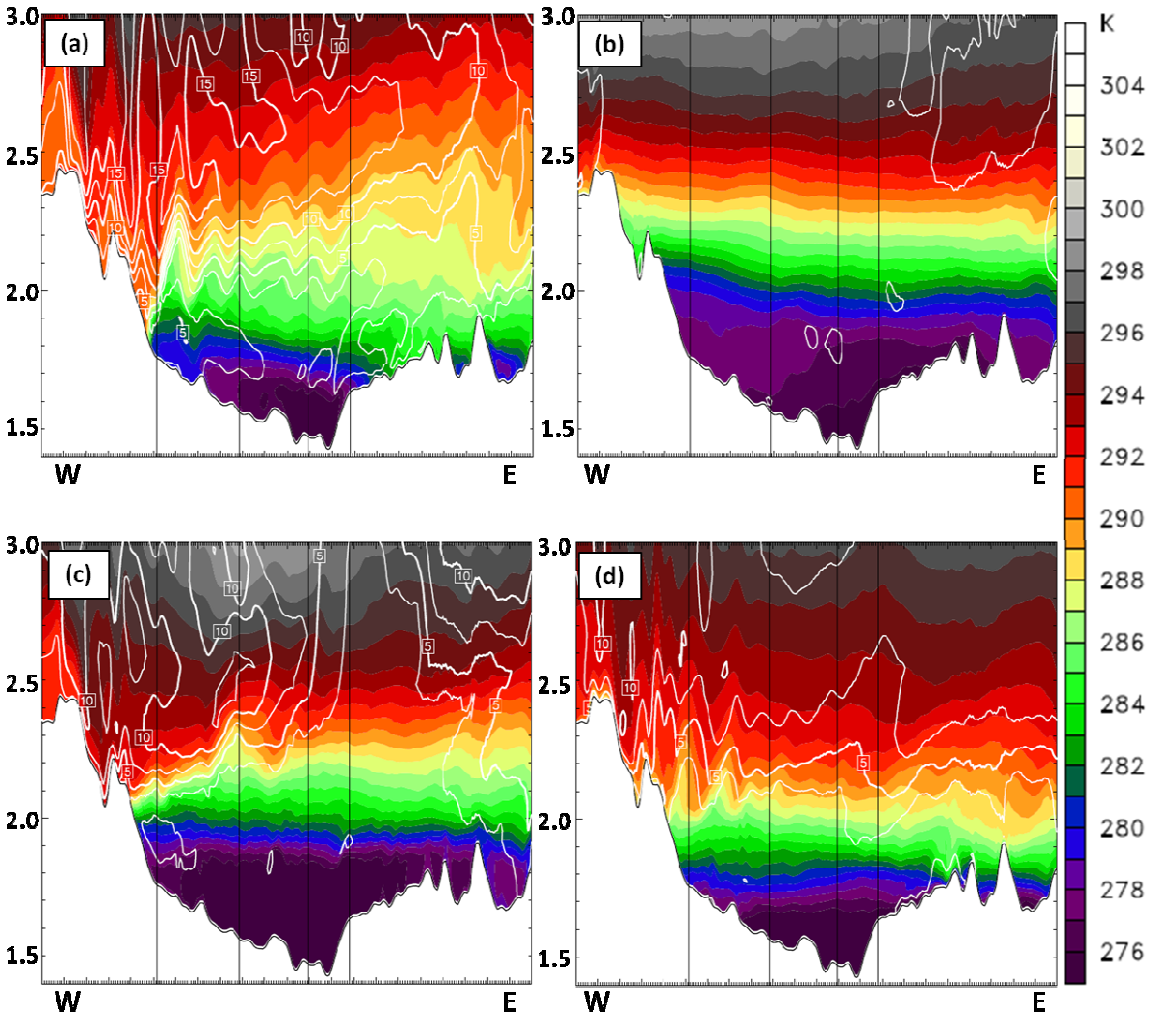

Fig. 3.14: Vertical cross sections of potential temperature (in K according to the scale on the right) and wind speed (contoured every 2.5 m s^{-1}) taken along the red line in Fig. 1.5b. MSL height on left side (km). Results shown from FULL simulation for (a) 1800 UTC 1 February, (b) 0600 UTC 3 February, (c) 1800 UTC 4 February and (d) 1500 UTC 6 February 2013.

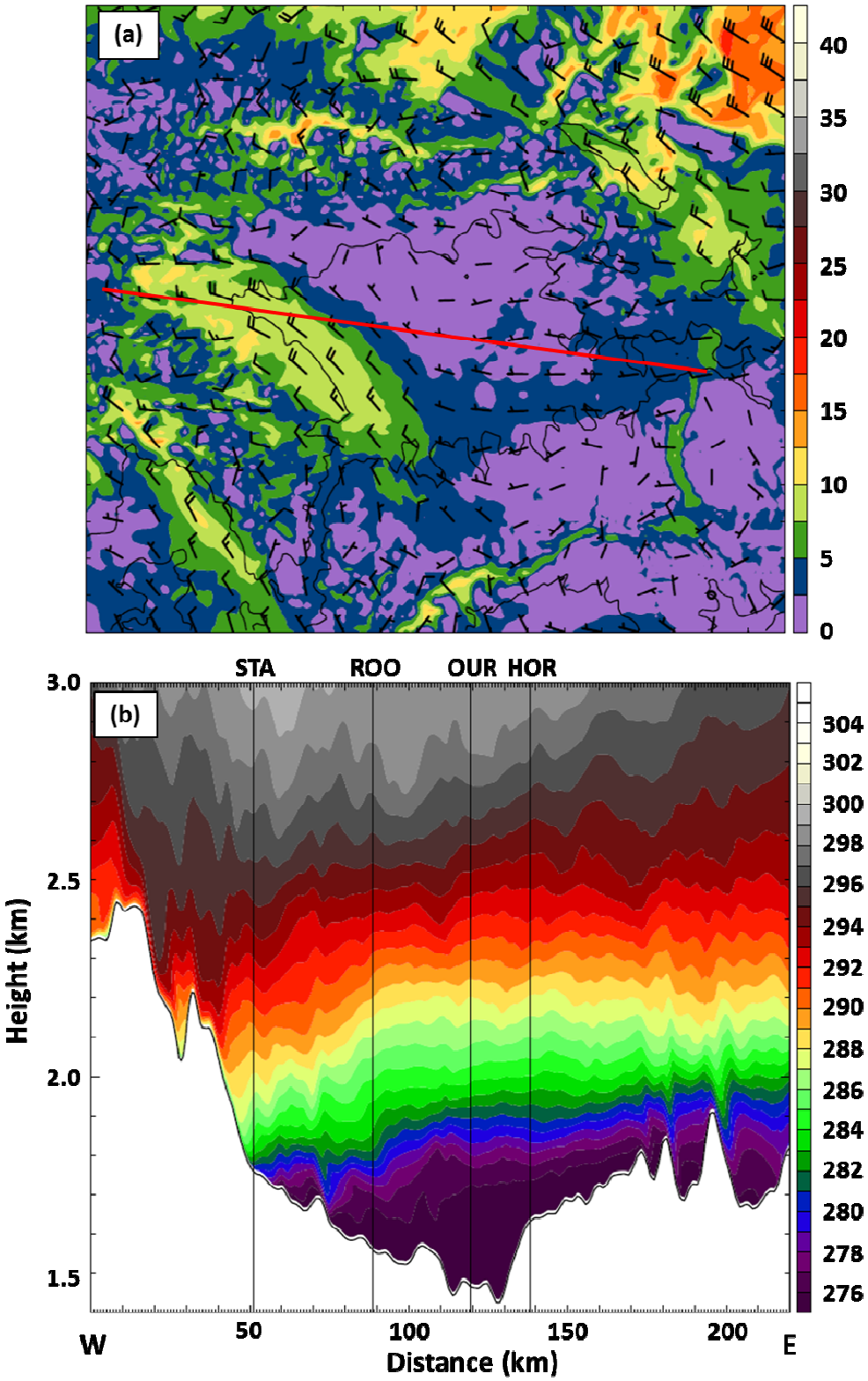

Fig. 3.15: FULL simulation at 0600 UTC 4 February 2013 for (a) 2.3 km MSL wind speed (in m s^{-1} according to the scale on the right) and barbs (full barb 5 m s^{-1}). (b) Vertical cross section of potential temperature (in K according to the scale on the right) along red line in (a).

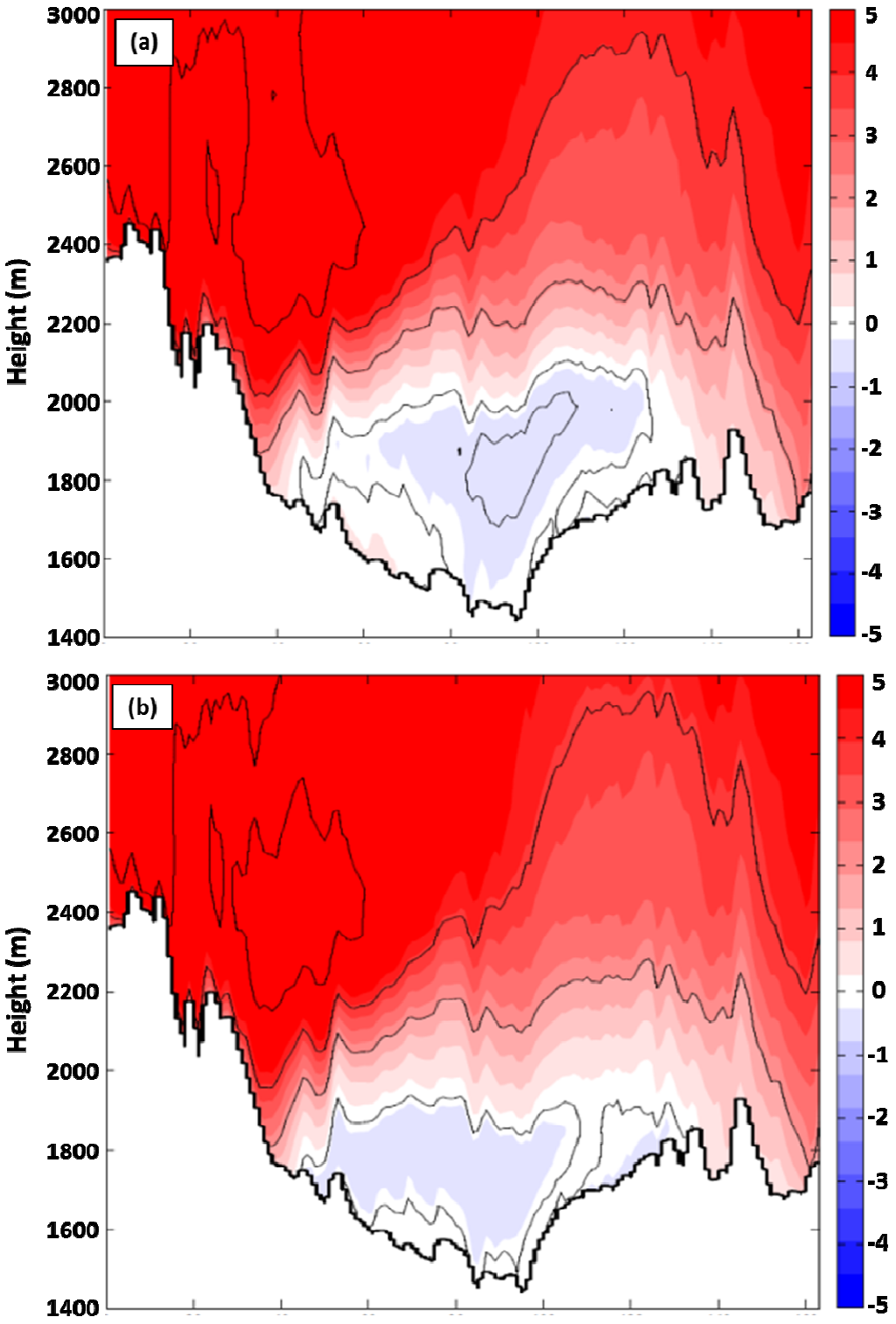

Fig. 3.16: Average zonal wind in the vicinity of the cross section in Fig. 1.5b for the 1–6 February 2013 period from (a) FULL and (b) NONE simulations. Westerly (easterly) winds shaded in m s^{-1} according to the scale on the right in red (blue) with westerly (easterly) winds contoured every 2 m s^{-1} (-0.5, -1, and -2 m s^{-1} only). Values are averaged over a ~26-km wide swath perpendicular to the cross section.

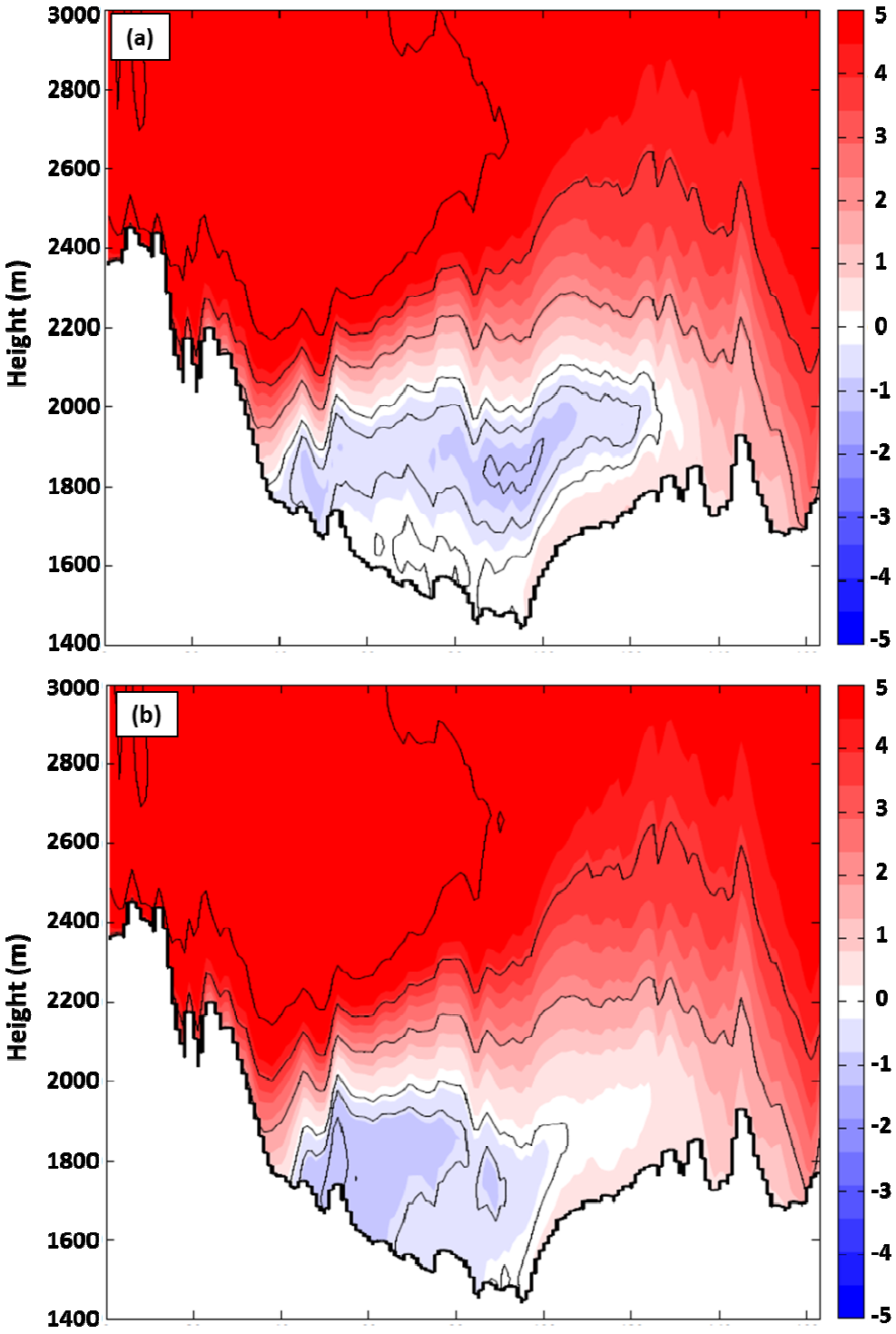

Fig. 3.17: Average zonal wind in the vicinity of the cross section in Fig. 1.5b for only the daytime hours (0800 to 1700 MST) of the 1–6 February 2013 period from (a) FULL and (b) NONE simulations. Westerly (easterly) winds shaded in m s-1 according to the scale on the right in red (blue) with westerly (easterly) winds contoured every 2 m s-1 (-0.5, -1, and -2 m s-1 only). Values are averaged over a ~26-km wide swath perpendicular to the cross section.

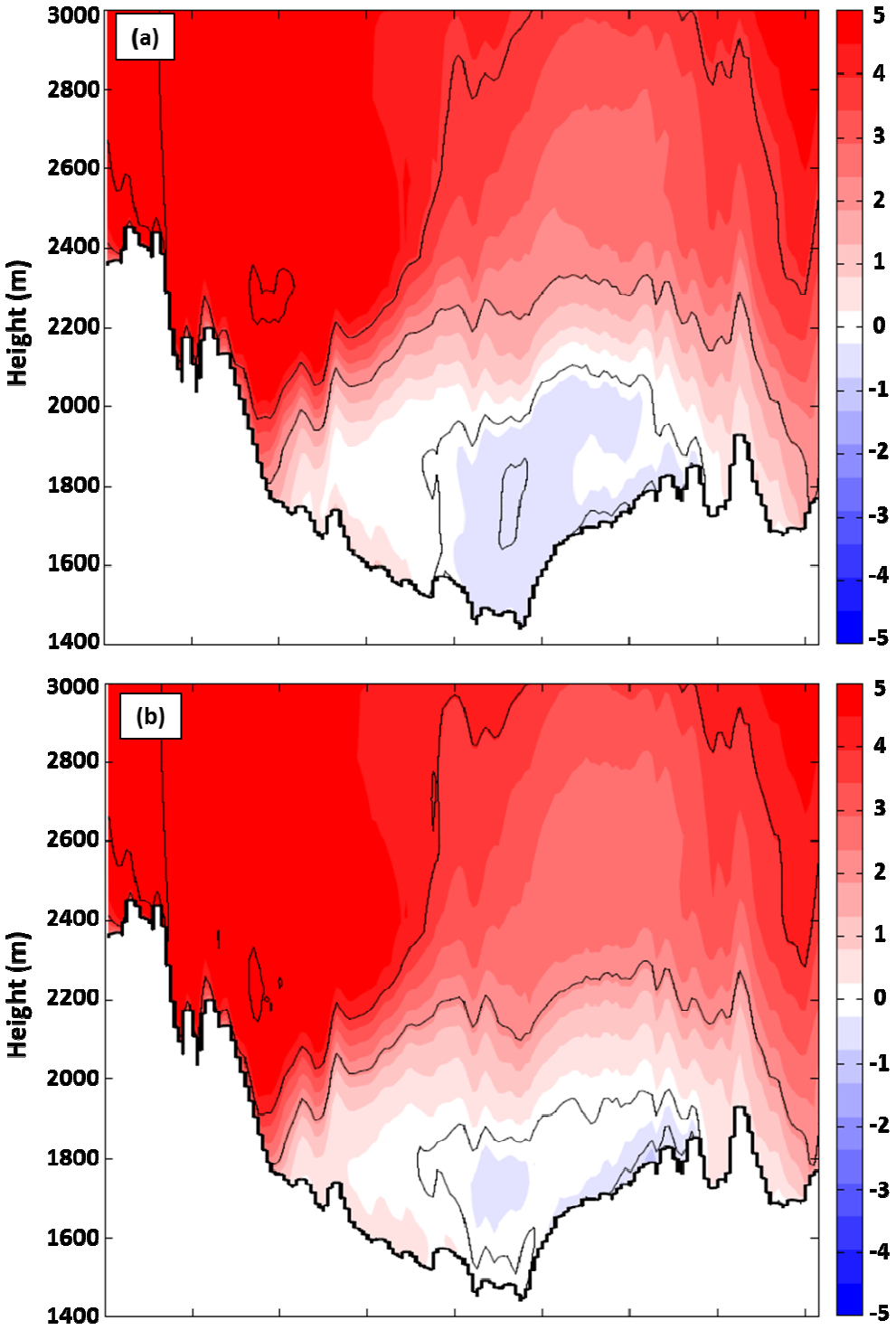

Fig. 3.18: Average zonal wind in the vicinity of the cross section in Fig. 1.5b for only the nighttime hours (1800 to 0700 MST) of the 1–6 February 2013 period from (a) FULL and (b) NONE simulations. Westerly (easterly) winds shaded in m s-1 according to the scale on the right in red (blue) with westerly (easterly) winds contoured every 2 m s-1 (-0.5, -1, and -2 m s-1 only). Values are averaged over a ~26-km wide swath perpendicular to the cross section.

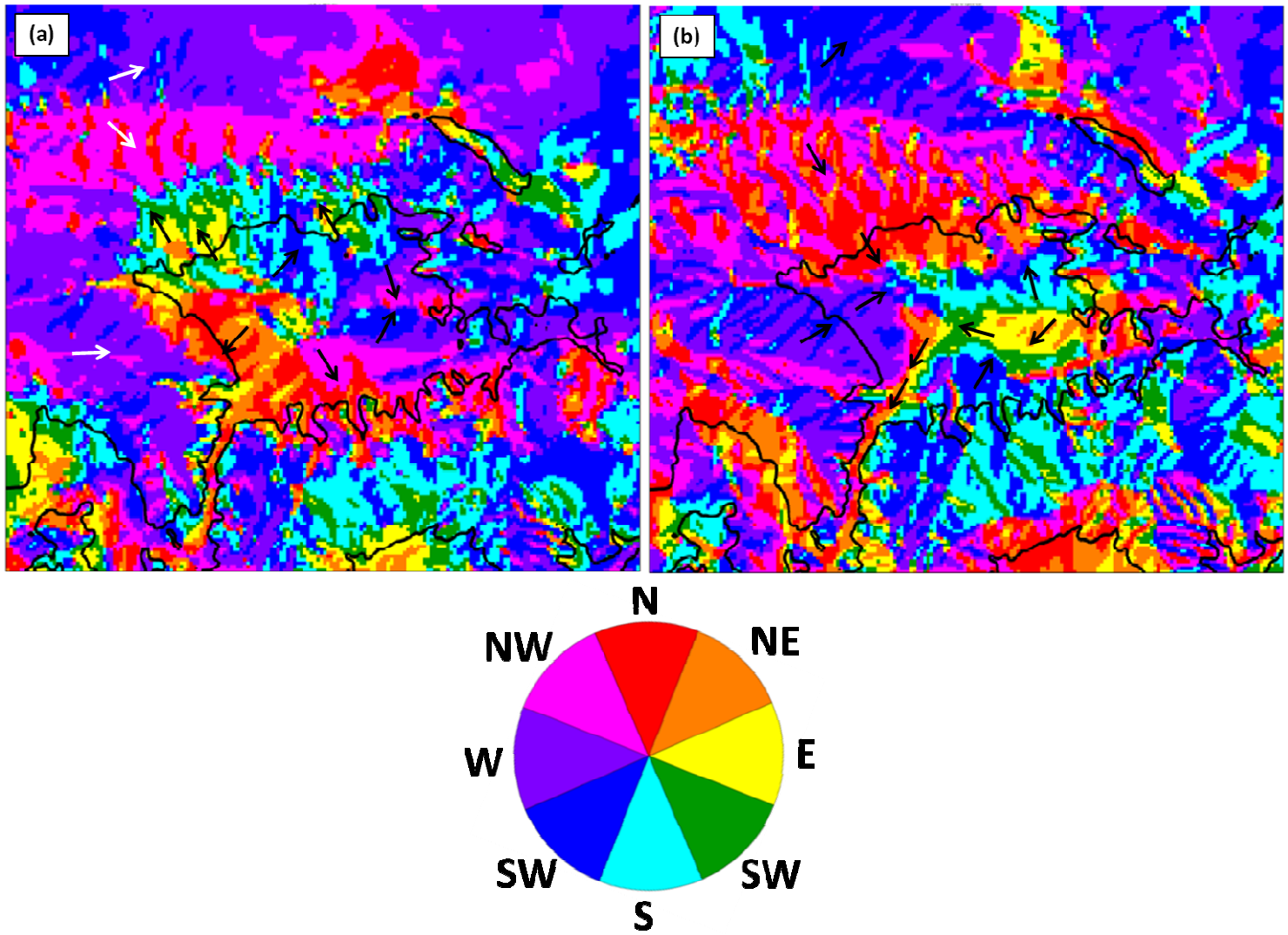

Fig. 3.19: Average 10-m wind direction for the 1–6 February 2013 period during (a) daytime hours (0800 to 1700 MST) and (b) nighttime hours (1800 to 0700 MST) from the FULL simulation.

Table 3.1: Two-meter temperature errors from WRF simulations. Mean errors calculated from the 6 surface stations in Fig. 1.5b during the 1–6 February 2013 period.

Simulation	**Bias (°C)**	**Mean Abs Error (°C)**	**RMSE (°C)**
BASE	1.65	3.25	3.97
FULL	0.11	2.44	2.98

Table 3.2: WRF simulation sensitivity to microphysics. Difference in longwave radiation and 2-m temperature between BASE and FULL simulations (BASE – FULL) during the 1–6 February 2013 period. Mean values shown for area below selected terrain contours within the basin.

BASE-FULL Difference	**< 1800 m**	**< 1700 m**	**< 1600 m**	**< 1500 m**
Longwave (W m^{-2})	11.77	10.63	8.97	7.21
2-m Temperature (°C)	1.24	1.46	1.65	1.78

Table 3.3: Two-meter temperature differences from WRF simulations. Mean differences calculated from FULL simulation (NW – FULL or NONE – FULL) during the 1–6 February 2013 period.

Simulation	**Difference (°C)**	**Mean Abs Diff (°C)**	**RMSD (°C)**
NW	0.14	0.21	0.28
NONE	7.60	7.60	7.85

CHAPTER 4

OZONE AND AIR QUALITY

4.1 1–6 February 2013 Air Quality Overview

The January–March 2013 period featured seven extended periods of high ozone concentrations in the Uintah Basin associated with persistent cold air pools (Stoeckenius and McNally 2014). An upper-level trough and associated cyclone traversed the region between 28 and 30 January 2013 (as discussed in Section 3.2), effectively cleaning out the basin of pollutants that had accumulated since mid-January and returning ozone concentrations to background levels. However, the persistent CAP that set in on 1 February led to building pollutant concentrations over the next several days. Fig. 3.4a shows the observed increase in ozone at selected locations. Concentrations started out relatively low on 1 February (~20 to 60 ppb) and gradually built to a maximum of 154 ppb at Ouray on 6 February. A key characteristic of ozone concentrations in many areas of the Uintah Basin is the maintenance of high levels of ozone overnight far above background concentrations. A mobile transect of the basin during the afternoon of 6 February shows elevated ozone concentrations in all locations, but the highest values (up to 151 ppb) were generally seen in lower elevations and river valleys (Fig. 4.1), particularly in the southeastern quadrant of the transect near Horsepool and Ouray.

While a weak system moved through the region late on 6 February, ozone levels remained elevated (particularly at Horsepool) until a stronger system moved through on 9 February (Fig. 3.4a).

Data collected from ozonesondes and tethersondes from February 2013 show that the vertical extent of maximum ozone concentrations was typically limited to 1700 m MSL and below, or in the lowest 200–300 m of the boundary-layer (Schnell et al. 2014). A gradient in concentrations was noted above this level, with ozone concentrations returning to background levels above 1900 m MSL (Karion et al. 2014).

4.2 Sensitivity of Ozone Concentrations to Snow Cover

While ozone concentrations in the Uintah Basin are known to be strongly controlled by the presence of snow cover, there is uncertainty regarding what extent is due to the direct effects of higher surface albedo on photolysis relative to the indirect meteorological effects elucidated in the previous chapter: reduced near-surface temperatures; shallower mixed layer; and possibly enhanced east-west cross-basin transport a few hundred meters above the surface. Further, there are additional possible indirect effects such as chemical reactions in the surface layers of the snow leading to critical precursor chemical compounds (Roberts et al. 2014). We describe here some preliminary results that address the combined sensitivity to increased surface albedo as well as meteorological changes in the boundary layer that result from the presence of snow cover.

WRF output from the entire 6-day FULL and NONE simulations was provided to collaborator L. Avey, Utah Division of Air Quality, who then imported those fields into

the agency's version of the Community Multiscale Air Quality (CMAQ) model. The CMAQ model couples the meteorological data from the WRF model with an emissions inventory from the Uintah Basin developed by the Utah Division of Air Quality and chemistry-transport and photochemical subsystems to simulate concentrations for a variety of chemical compounds and pollutants (Byun and Schere 2006). The emissions inventory used in this study contained the most complete and accurate data available for the Uintah Basin. However, the inventory was prepared to represent emissions from 2011 based on growth of oil and gas activities since 2006 (Barickman et al. 2014). Data gathered during recent UBWOS field campaigns, along with additional projects, will be incorporated into an emissions inventory update scheduled for 2014. Since the emissions inventory and CMAQ are available from the Utah Division of Air Quality on the 4 km grid, that model was forced with WRF data from the 4 km nest shown in Fig. 1.5a as well as Fig. 4.2. The objective of this phase of the study is to simply assess the sensitivity of ozone concentration to snow cover during a CAP. The potential shortcomings of driving CMAQ from imperfect atmospheric information and emissions inventories as well as the limitations of CMAQ are not addressed.

The mean ozone concentrations near the surface averaged over the 6 afternoons (1100 to 1700 MST) from 1–6 February 2013 are generally 15–30% greater when the CMAQ model is forced by the snow cover and meteorological conditions in the FULL simulation compared to the absence of snow in the basin and concomitant conditions in the NONE simulation (Fig. 4.3). Ozone concentrations simulated by the CMAQ model are highest in the southeastern portion of the basin where the emission of ozone precursors (NO_X and VOCs) from the emissions inventory is greatest (Barickman et al. 2014). The region

where average concentrations are greater than 75 ppb is ~6 times larger in the FULL simulation than that in the NONE simulation. In addition, the peak ozone concentration simulated in the FULL case is 16 ppb higher than that from the NONE case (Table 4.1) and the timing and magnitude of the peak value on 6 February in the FULL case is comparable to that observed (see Figs. 3.4 and 4.1). Higher levels of ozone are simulated on average throughout the basin below 1800 m when driven by the FULL simulation compared to the NONE simulation.

Time-averaged east-west cross sections of ozone (Fig. 4.4) were averaged along the 24 km wide swath delineated in Fig. 4.2 for both the FULL and NONE simulations. Comparison between the two simulations demonstrates the higher ozone concentrations generated in the FULL run. The CMAQ model appears to lift the ozone slightly higher in the FULL simulation than observed with the drop-off to background levels (less than 60 ppb) taking place at 2000 m in the FULL simulation versus that observed roughly below 1900 m at Horsepool (Karion et al. 2014).

The time evolution of ozone concentrations at selected locations is shown in Fig. 4.5. Data at Roosevelt (Fig. 4.5a) indicate that CMAQ struggles to simulate the buildup of ozone during the CAP period in the western portion of the basin. This is likely due to the spatial variation of primary precursor emissions in the emissions inventory. A relatively small amount of emissions exists in the western section when compared to the southeastern quadrant of the basin (Barickman et al. 2014). Both the FULL and NONE simulations keep concentrations generally near 50–60 ppb, and below the NAAQS of 75 ppb. Closer to the specified primary precursor emission sources in the southeastern section of the basin, ozone concentrations are noticeably higher at Horsepool with

substantively higher concentrations when snow cover is specified (Fig. 4.5b). Within the primary precursor emission source region (Seven Sisters, Fig. 4.5c), the time evolution of ozone in the FULL simulation is similar to that observed with substantively higher concentrations than when snow is absent. The differences in ozone concentrations among these three locations illustrates that the CMAQ model with the emission inventories available at this time struggles to capture the broad areal extent of high ozone concentrations that are observed in this case.

Time-height sections in Fig. 4.6 of ozone and potential temperature at Horsepool help to analyze the evolution of the CAP and pollutant concentration as a function of snow cover. While the highest concentrations of ozone are confined within the CAP during the FULL simulation, elevated concentrations in excess of 75 ppb extend too far upwards in the afternoons into the base of the inversions. In addition, CMAQ fails to build ozone concentrations each day through the CAP event in the FULL simulation (Fig. 4.6a). Instead, the highest concentrations appear to be related to the depth of the CAP and inversion base. Concentrations are high on 1 and 2 February, when the CAP is shallow, then they decrease on the 3rd and 4th as the CAP deepens and the inversion base lifts to ~1800 m. As the inversion base lowers again on 5 and 6 February, concentrations increase with a maximum during the afternoon on the 6th. A similar evolution is noted in the NONE simulation (Fig. 4.6b), but the CAP is much deeper, concentrations are lower, and the maximum occurs on the afternoon of the 5th. This inverse relationship between CAP depth and ozone concentrations is supported by observations, signifying its potential importance. Intuitively, when the inversion base lowers, it effectively decreases the volume of the shallow mixed-layer in the CAP resulting in higher ozone concentrations.

Figure 4.7 shows time series from 1–6 February for shortwave radiation applicable to photochemistry from the FULL and NONE simulations. These values are averaged over a 26 by 39 km box in the center of the basin shown in Fig. 4.2. Downward shortwave radiation at the surface is generally similar between the FULL and NONE simulations (Fig. 4.7a). However, when both simulations have extensive cloud cover (such as midday on 3 and 4 February), the FULL simulation has ~150 W m^{-2} more downward shortwave radiation. This is likely because the ice-dominant clouds in the FULL simulation allow for greater transmittance of shortwave radiation than the liquid-dominant clouds in NONE. For all days, the upward (or reflected) shortwave radiation is greater in the FULL case, due to the high albedo of snow compared to the bare ground in the NONE case (Fig. 4.7b). The total shortwave radiation near the surface (sum of upward and downward radiation) is a crude approximation for actinic flux omitting, for example, the contribution due to scattering. Figure 4.7c shows that the total shortwave radiation in the FULL simulation is over ~1.5 times greater than that in the NONE simulation during the day. The greater total shortwave radiation in FULL then contributes to higher photolysis rates and greater ozone concentrations.

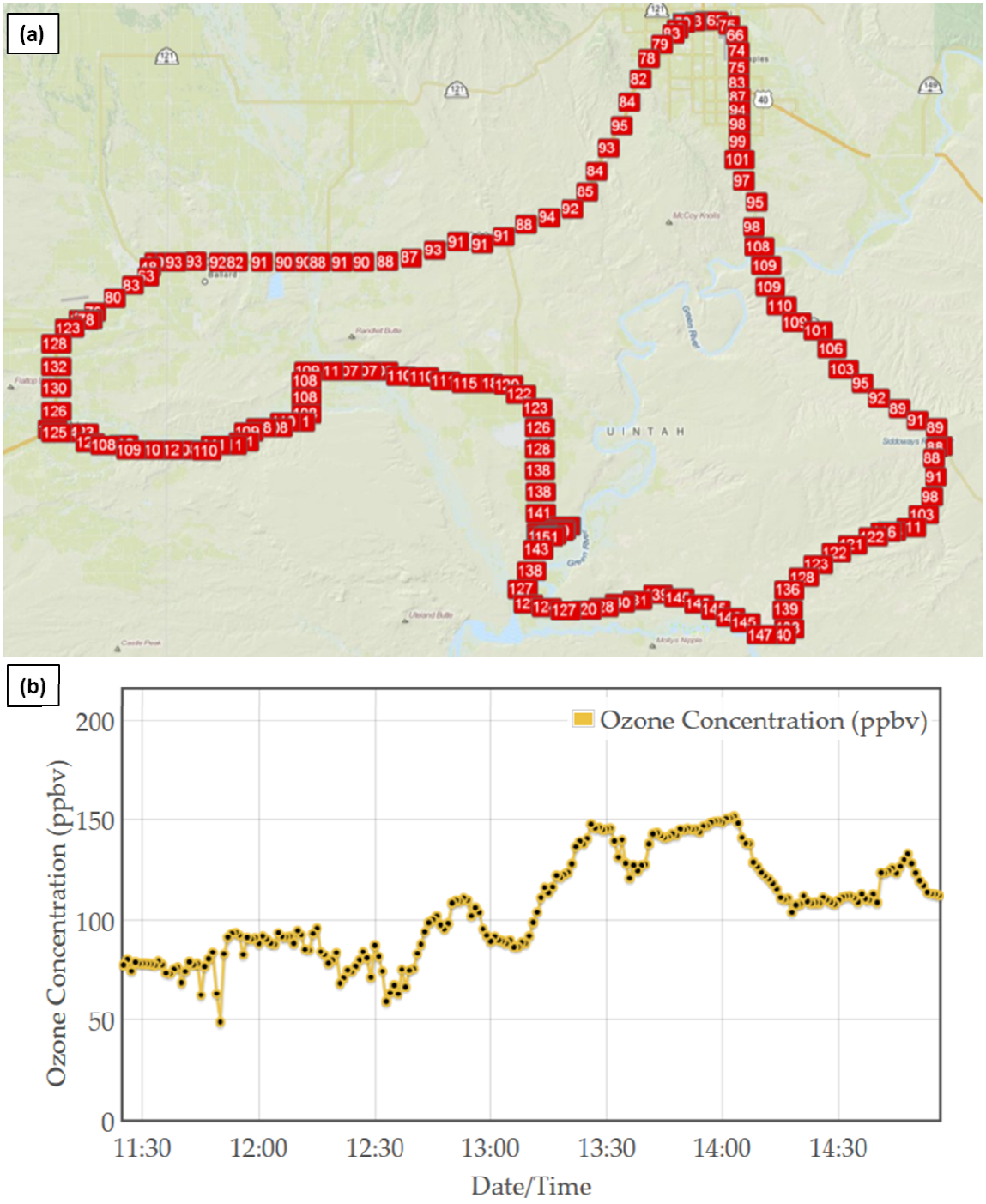

Fig. 4.1 Mobile transect of ozone concentration from 1130 to 1500 MST 6 February 2013 as a function of: (a) geographic location and (b) time.

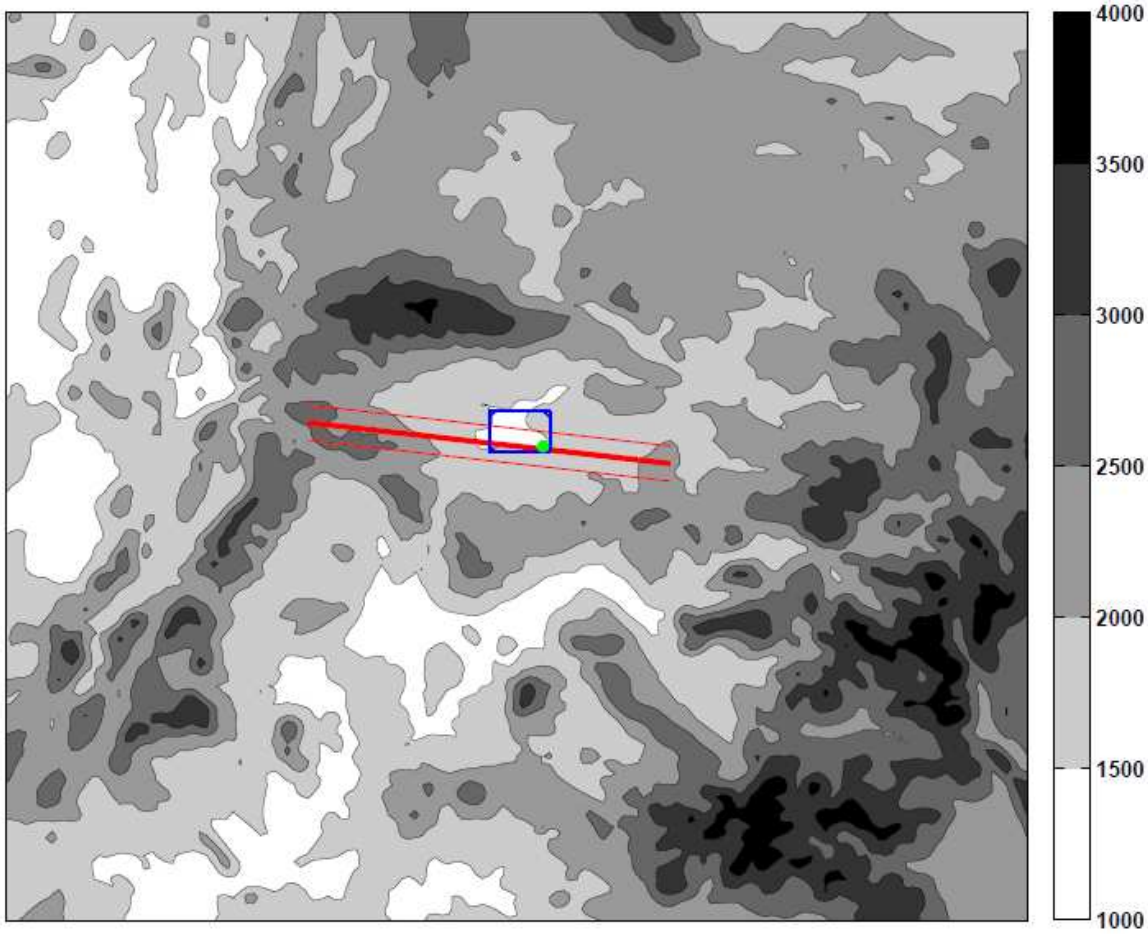

Fig. 4.2: Four-km model domain used in CMAQ simulations (terrain in m and shaded according to the scale on the right). The thick red line marks the location of ozone cross sections in Fig. 4.4 while the thin red lines delineate the spatial extent of the area-average in the direction perpendicular to the cross section. The blue box represents the area used for mean shortwave radiation calculations in Fig. 4.7 while the green dot indicates the location of the Seven Sisters ozone monitoring station discussed in the text.

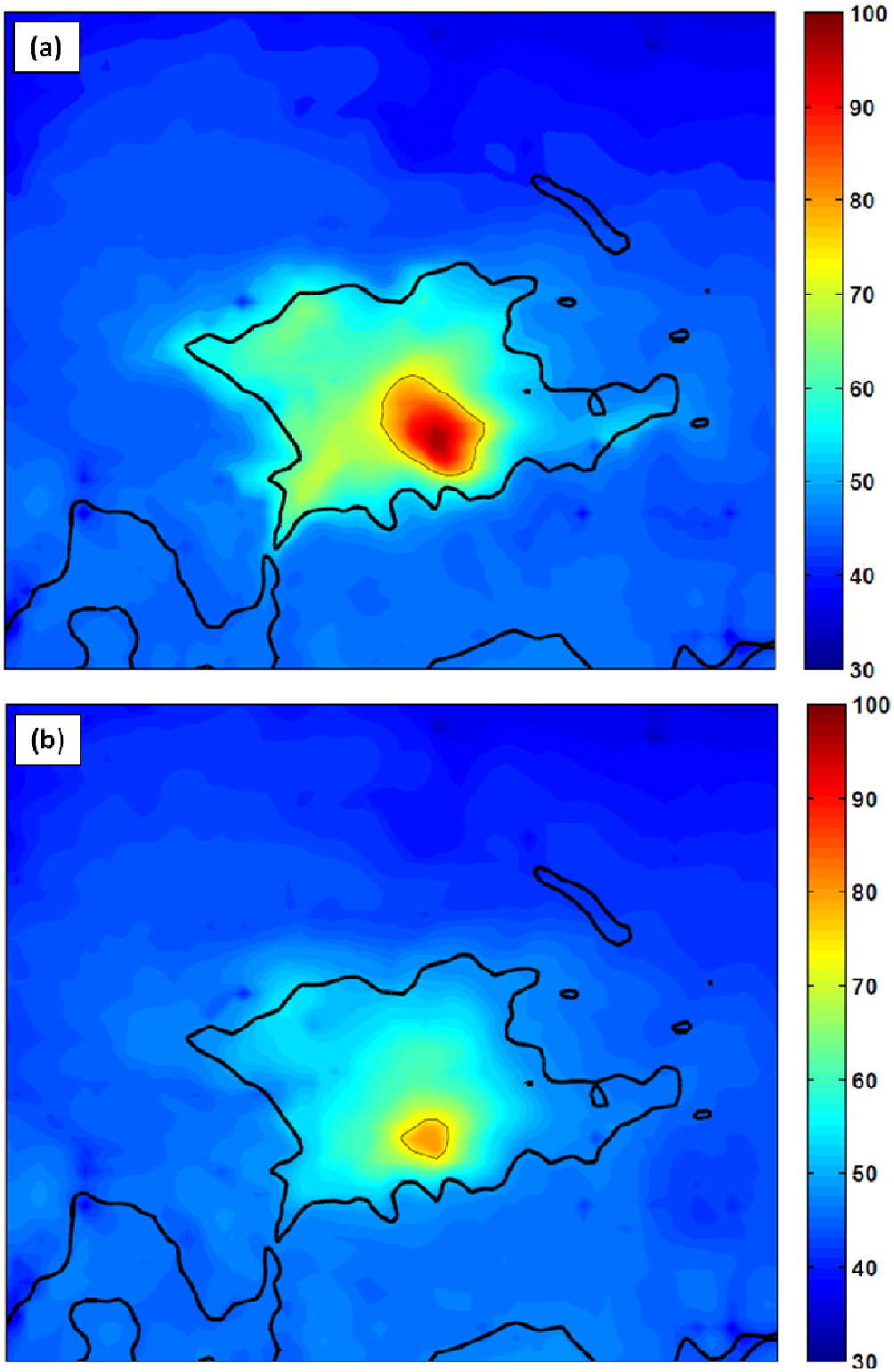

Fig. 4.3: Average ozone concentration (in ppb according to scale on the right) during 1100-1700 MST 1–6 February 2013 on the lowest CMAQ model level (~17.5 m) from (a) FULL and (b) NONE simulations. The thin black line outlines regions where the ozone concentration exceeds 75 ppb while the reference terrain elevation of 1800 m is shown by the heavy black line.

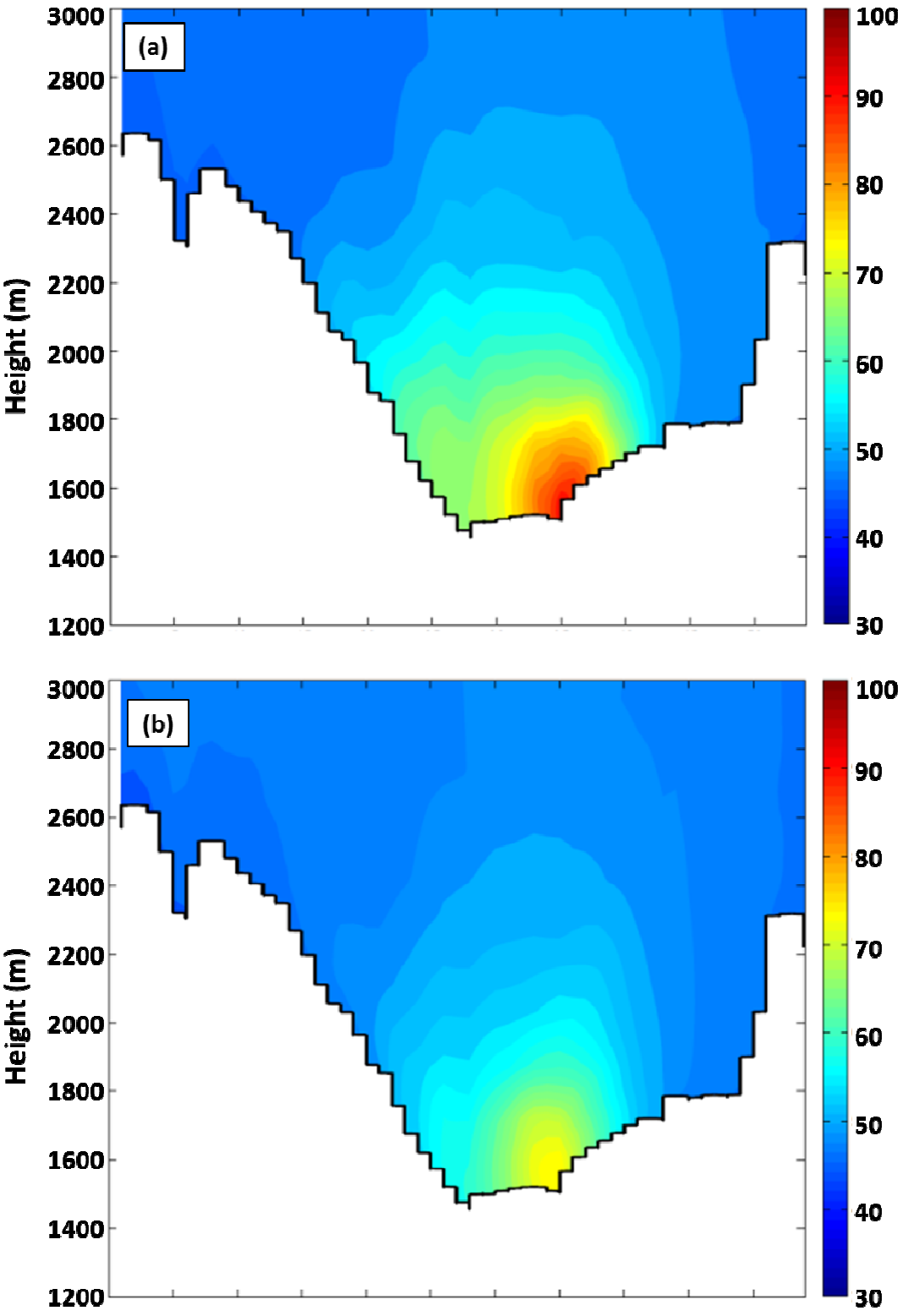

Fig. 4.4: Average ozone concentration (in ppb according to the scale on the right) during 1100-1700 MST 1–6 February 2013 between the thin red lines in Fig. 4.2 from (a) FULL and (b) NONE WRF simulations.

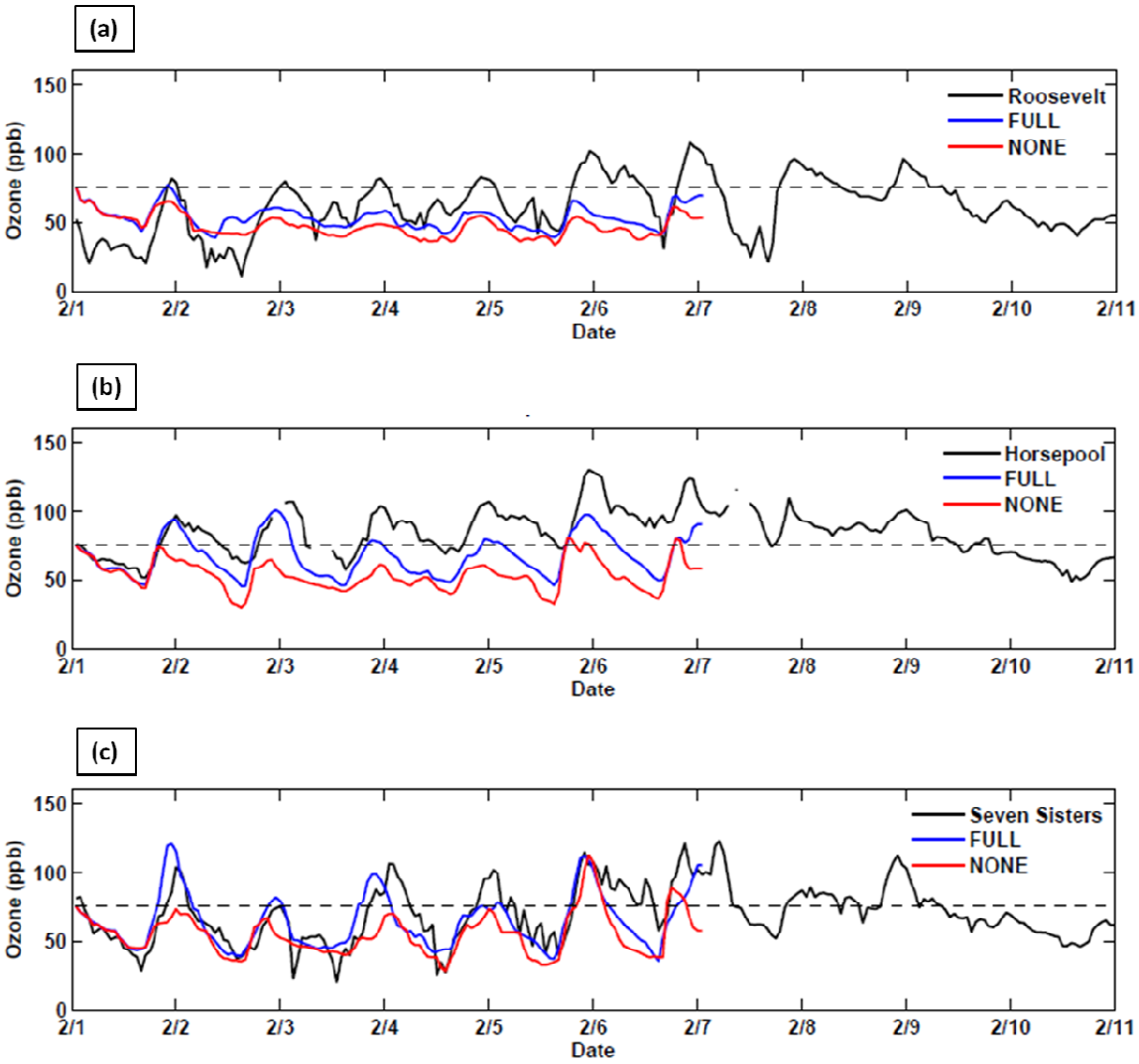

Fig. 4.5: Time series of ozone concentrations from (a) Roosevelt, (b) Horsepool, and (c) Seven Sisters. Observations, CMAQ output from FULL and NONE simulations in black, blue, and red, respectively. The NAAQS is denoted by the thin black dashed line.

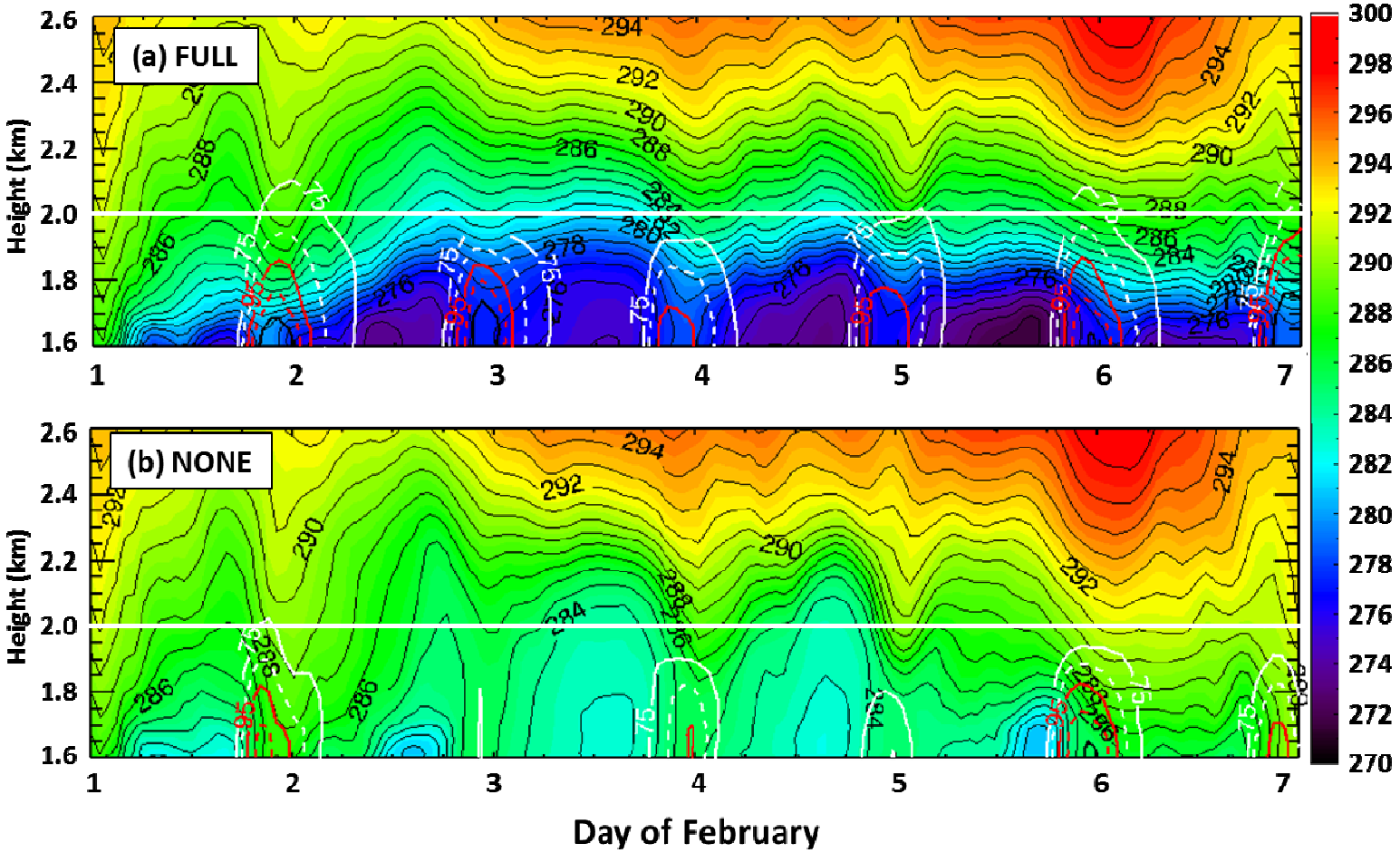

Fig. 4.6: Time-height plot of potential temperature at Horsepool (in K according to the scale on the right and contoured at an interval of 1 K) and ozone concentrations (white and red contours) from (a) FULL and (b) NONE simulations. Ozone concentrations are contoured every 10 ppb, starting at 75 ppb and alternate between solid and dashed every 10 ppb. Plotted ozone concentrations represent the maximum value for each hour in a 40 by 40 km region encompassing Ouray and Horsepool (not shown).

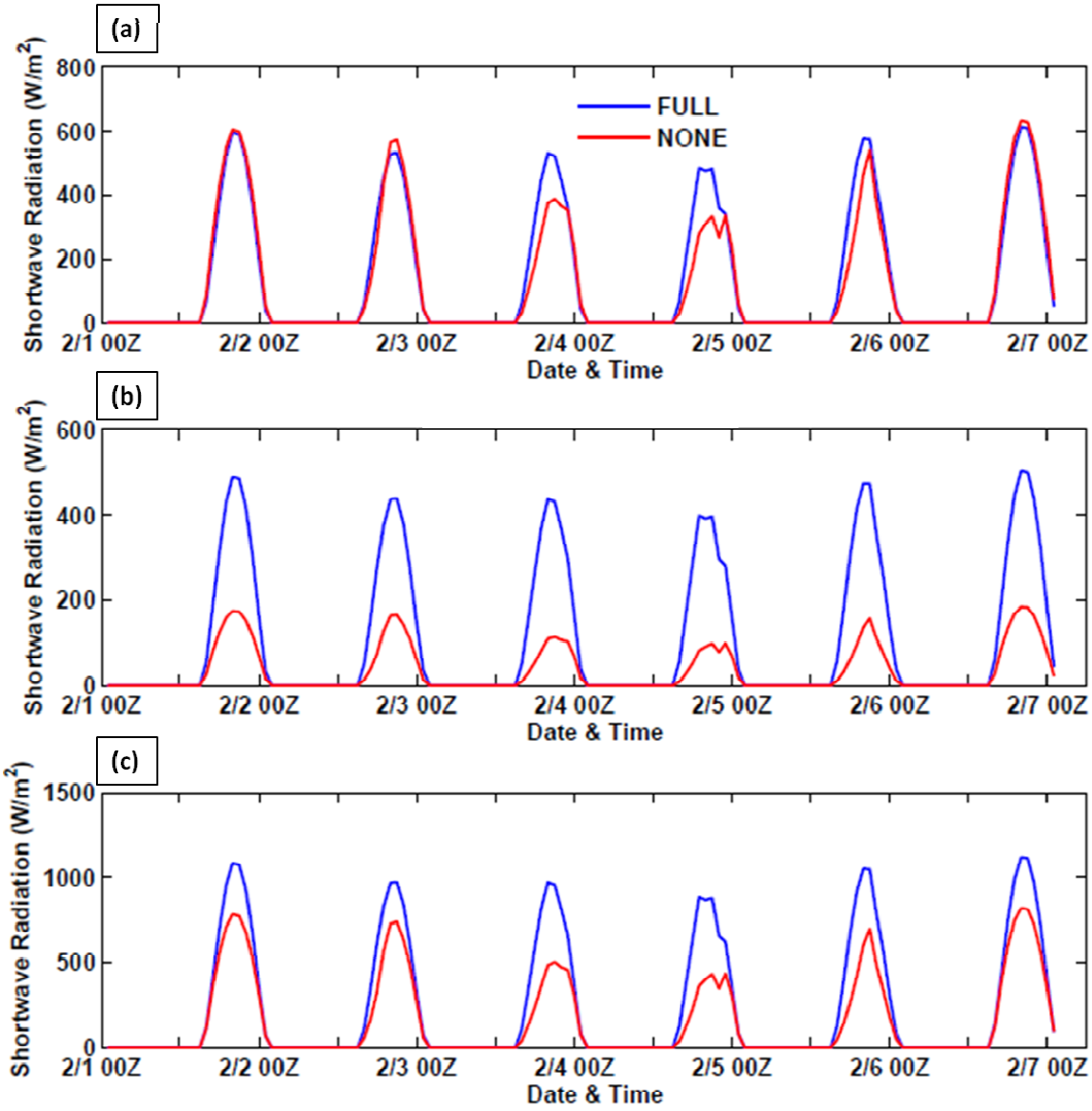

Fig. 4.7: Time series of shortwave radiation data at the surface from FULL (blue), and NONE (red) simulations: (a) downward radiation, (b) upward radiation, and (c) sum of downward and upward radiation. Values are averaged over a 26 by 39 km box in the center of the basin (shown in Fig 4.2).

Table 4.1: Ozone concentration statistics from CMAQ model forced by FULL and NONE simulations during the 1–6 February 2013 period.

	FULL	**NONE**
Highest mean O_3 - Afternoon (ppb)	97.2	81.2
Highest mean O_3 - Non afternoon (ppb)	61.9	51.0
Maximum Hourly O_3 (ppb)	134.4	118.0
Area of mean afternoon O_3 > 75 ppb (km^2)	896	144

CHAPTER 5

CONCLUSIONS AND DISCUSSION

5.1 Overview and Research Questions

Numerical simulations of a persistent CAP in the Uintah Basin from 1–6 February 2013 were conducted to investigate the sensitivity of cloud microphysics and snow cover on CAP evolution and structure. Terrain-flow interactions and basin- and smaller-scale thermally-driven circulations were identified as possible means to infuse clean air into the basin as well as transport pollutants within the basin. Output from selected meteorological simulations was input into the CMAQ model to investigate the sensitivity of ozone production to snow cover. The key findings of this study can be summarized as follows:

- Nested numerical simulations at high resolution (1.33 and 4 km) driven on the outer domain by continually updating analyzed lateral boundary conditions are capable of reproducing the large-scale features of the regional circulation over the Uintah Basin that control the basic morphology of the CAP.
- The intensity, vertical structure, and boundary-layer flows within the Uintah Basin CAP below ~500 m AGL are heavily influenced by the numerical treatment of cloud microphysics and snow cover.

- The default settings in the Thompson microphysics scheme produce dense, liquid-phase low clouds and fog that were not observed, whereas restricting ice sedimentation and cloud ice conversion to snow in the lowest model layers resulted in more realistic vertical profiles of temperature and low clouds in this case.
- Intrusions of clean air into the basin as a result of terrain-flow interactions, east-to-west cross-basin transport above the surface, and shallow thermally-driven slope and valley circulations are important factors for pollutant transport within the Uintah Basin.
- CMAQ model-derived estimates of ozone concentrations that are forced by the most realistic emission inventories available and the best specification of the snow surface and meteorological conditions tend to be adequate near major precursor emission source regions in the southeast quadrant of the basin but too low throughout most of the basin and overnight.

Partial answers to the specific research questions posed in Chapter 1 and additional related discussions on the implications of these findings are now provided.

- *What is the sensitivity of simulated CAP structure and evolution to cloud microphysics?*

The variations in radiative opacity and depth of simulated boundary-layer clouds resulting from the phase change from liquid to ice cloud particles had a significant impact on the modeled CAP structure and evolution. The sensitivity of the CAP to cloud droplet phase was tested by implementing a modified version of the Thompson microphysics scheme in the FULL simulation. This results in extended periods of ice fog and a

reduced 2-m temperature bias in that simulation, whereas liquid-phase stratus dominates in the default, BASE simulation. Furthermore, the depth of the CAP mixed layer in the FULL simulation is shallower and more representative of observed conditions. Both of these improvements are attributed to decreased nocturnal longwave radiation, greater cooling and a shallower, more realistic surface-based fog layer in the FULL simulation as a result of the change in cloud phase.

For this study, the modifications to the microphysics scheme (autoconversion from cloud ice to snow and sedimentation of cloud ice turned off) were potentially available to be triggered everywhere within the entire model simulation period in the lowest 15 model levels. However, these modifications had no impact outside of the Uintah Basin's CAP, due to the dominance of upper-level ridging and minimal precipitation generated elsewhere. The objective for making these modifications was to test whether those changes improve the physical treatment of clouds relevant to the Uintah Basin. To apply the changes more generally requires some additional code modifications to activate them based on appropriate boundary layer thresholds of stability and temperature (e.g., presence of a strong temperature inversion and low-level temperatures lower than -12 °C, the cloud ice nucleation temperature specified in the model). In this manner, the changes to the microphysics scheme would only be triggered to deviate from the default settings when specific criteria appropriate only to CAPs were met. The restricted sedimentation of ice particles in the lowest 15 model layers can lead to excessive ice accumulation but cloud ice is still able to convert to snow once it reaches a large enough diameter through depositional growth.

- *How do snow cover variations affect CAP simulations and structure?*

Removing snow cover has a profound effect on CAP characteristics for the event examined here. When snow is removed from the basin, the 2-m temperatures are much higher and the boundary layer is much deeper. Above ~1 km AGL and outside of the Uintah Basin CAP, no obvious differences were evident by removing snow cover in the basin. Hence, snow cover changes tend to affect processes internal to the boundary layer, since the strong stability above the CAP insulates the free atmosphere from the effects of the underlying surface.

- *What are the important wind flow regimes in the Uintah Basin CAP? Can they be diagnosed by mesoscale modeling and how might they affect air quality in the basin?*

A number of interrelated flow regimes exist in the Uintah Basin that may affect pollutant concentrations. The CAP is continually modulated by synoptically-driven mid-level flow atop the CAP and may become displaced or tilted through hydrostatic and dynamic processes forcing it to oscillate back and forth within the basin. Downslope flows carrying warmer, cleaner air into the basin are common and their impact depends on the stability and strength of the flow across the upwind barriers. Easterly flow immediately above the shallow mixed layer is observed across the basin and the WRF simulations suggest this weak flow is quite persistent during CAP episodes. Ozone precursors from eastern basin source regions may be entrained into the easterly flow layer and then transported westward to portions of the basin that have more limited precursor sources. Weak near-surface thermally-driven valley and slope flows are ubiquitous throughout the basin and likely contribute to localized redistribution of pollutants. These flow features appear to be fairly well-resolved within the 1.3 km WRF domain and likely

have distinct impacts on air quality. As a result, poor air quality may be seen throughout the basin particularly when precursors have time to migrate throughout the basin.

- *What is the influence of snow cover on air quality simulations in the Uintah Basin?*

Comparison of the FULL and NONE simulations demonstrates that the absence of snow cover leads to improvements in air quality. The high surface albedo of snow cover plays a critical role during wintertime ozone events for two reasons: (1) it strengthens CAPs and increases stability, and (2) it increases photolysis rates, contributing to rapid ozone production. The strong CAPs that form when snow cover is present have shallower PBLs and stronger stability within the inversion layer. Both of these properties act to trap pollutants and ozone precursors in the lowest few hundred meters of the atmosphere. The high albedo also increases actinic flux and fuels rapid ozone production near the surface when precursor concentrations are high. While the contributions to ozone production of the direct effects of enhanced actinic flux relative to the indirect effects of modifications to the atmospheric structure cannot be separated in this study, their combined effect is quite evident with mean afternoon ozone concentrations increasing substantially relative to when no snow cover is present.

5.2 Future Work

The work presented here has been limited to a single persistent CAP event in early February 2013. In order to obtain a more thorough understanding of how cloud microphysics and snow cover affect the evolution of persistent CAPs, their wind flow patterns, and resulting impacts on air quality, further studies are needed. A natural

extension of this research would be to include a greater number of CAP cases over a range of initial and boundary conditions that could be verified with observational data from recent winters to examine the robustness of these findings. For example, many persistent CAPs with snow cover do not produce any clouds or fog within the basin. How do boundary-layer vertical structure, flows, and subsequent pollutant transport differ between clear and cloudy CAPs within the Uintah Basin? Additional modeling studies in other locations prone to wintertime ozone events, such as the Upper Green River Basin, would help determine how applicable the findings of this study may be.

The microphysics modifications implemented to gauge the CAP sensitivity to cloud phase were very targeted and applied to achieve a specific effect. Further testing could be done with other microphysics schemes to determine if similar sensitivities are noted and to implement appropriate controls so that the modifications only apply to CAP situations.

Another challenge to model CAPs is the weakness of PBL schemes to handle low clouds, vertical temperature profiles, and mixing in stably stratified conditions. Most schemes generally allow for too much turbulent mixing, which results in boundary layers that are too deep (Holtslag et al. 2013). Mesoscale forecast models also poorly forecast whether or not low clouds will form within a persistent CAP and when they will break up. They also have considerable uncertainty in representing surface variables, often leading to 2-m temperature warm biases, and in some cases poorly simulate the inversion above the boundary layer (Reeves et al. 2011; Shin and Hong 2011). Alternative PBL parameterizations, such as the Mellor-Yamada Nakanishi and Niino and Quasi-Normal Scale Elimination schemes, were not tested in this study, but may show some

improvement for CAPs. Regardless, further work to improve parameterization schemes for modeling of very stable boundary layers and their impact on CAP simulations is needed (Baklanov et al. 2011), as well as a better understanding of the limitations and biases of various numerical parameterization schemes in CAP environments.

Finally, snow cover and albedo were shown to have a prominent impact on CAP evolution and air quality. This study has highlighted the need for improvements in the representation of snow variables in meteorological and air quality models and analysis initialization fields in regions with shallow, persistent snow cover. Due to weaknesses in the NAM analysis, a prescribed snow field and albedo based on observational data was applied here. However, this approach is inefficient for operational settings. Proper treatment of snow using a snow physics model driven by local atmospheric and chemical properties may be needed to obtain a sufficiently accurate evolution of the snowpack and surface albedo. Application of the Noah Multiparameterization land surface model, which features a three-layer snow model (Niu et al. 2011), may be a useful approach to test. Additional research is also needed to understand the complex cycling of water over the thin snowpacks in the Uintah Basin and its impact on surface albedo, i.e., the interplay of very small sublimation rates, formation of ice fogs, and deposition of ice crystals back onto the snow surface.

REFERENCES

Alcott, Trevor I., W. James Steenburgh, 2013: Orographic influences on a Great Salt Lake–Effect snowstorm. *Mon. Wea. Rev.*, **141**, 2432–2450.

Baklanov, Alexander A., and Coauthors, 2011: The nature, theory, and modeling of atmospheric planetary boundary layers. *Bull. Amer. Meteor. Soc.*, **92**, 123–128.

Barickman, Patrick, Seth Lyman, Marc Mansfield, Howard Shorthill, Randy Anderson, Jordan Evans, Chad Mangum, and Tate Shorthill, 2014: Emission inventory development activities. In T. Stoeckenius and D. McNally (Eds.), *Final Report: 2013 Uinta Basin Winter Ozone Study*, Chapter 9, 18 pp.

Bell, Michelle L., Aidan McDermott, Scott L. Zeger, Jonathan M. Samet, Francesca Dominici, 2004: Ozone and short-term mortality in 95 US urban communities, 1987–2000. *J. Am. Med. Assoc.*, **292**, 2372–2378.

Billings, Brian J., Vanda Grubišić, Randolph D. Borys, 2006: Maintenance of a mountain valley cold pool: A numerical study. *Mon. Wea. Rev.*, **134**, 2266–2278.

Byun, D., and K. L. Schere, 2006: Review of the governing equations, computational algorithms, and other components of the Models-3 Community Multiscale Air Quality (CMAQ) modeling system. *Appl. Mech. Rev.*, **59**, 51–77.

Cai, X.-M, Luhar A. K., 2002: Fumigation of pollutants in and above the entrainment zone into a growing convective boundary layer: A large-eddy simulation. *Atmos. Environ.*, **36**, 2997–3008.

Chen, Fei, Jimy Dudhia, 2001: Coupling an advanced land surface–hydrology model with the Penn State–NCAR MM5 modeling system. Part I: Model implementation and sensitivity. *Mon. Wea. Rev.*, **129**, 569–585.

Clements, Craig B., C. David Whiteman, John D. Horel, 2003: Cold-air-pool structure and evolution in a mountain basin: Peter Sinks, Utah. *J. Appl. Meteor.*, **42**, 752–768

Fry, J., Xian, G., Jin, S., Dewitz, J., Homer, C., Yang, L., Barnes, C., Herold, N., and Wickham, J., 2011: Completion of the 2006 National Land Cover Database for the conterminous United States, *Photogram. Eng. Remote Sensing*, **77**, 858–864.

Hart, Kenneth A., W. James Steenburgh, Daryl J. Onton, 2005: Model forecast improvements with decreased horizontal grid spacing over finescale intermountain orography during the 2002 Olympic Winter Games. *Wea. Forecasting*, **20**, 558–576.

Holtslag, A. A. M., and Coauthors, 2013: Stable atmospheric boundary layers and diurnal cycles: Challenges for weather and climate models. *Bull. Amer. Meteor. Soc.*, **94**, 1691–1706.

Horel, J., and Coauthors, 2002: Mesowest: Cooperative mesonets in the western United States. *Bull. Amer. Meteor. Soc.*, **83**, 211–225.

Iacono, M. J., J. S. Delamere, E. J. Mlawer, M. W. Shephard, S. A. Clough, and W. D. Collins, 2008: Radiative forcing by long-lived greenhouse gases: Calculations with the AER radiative transfer models. *J. Geophys. Res.*, **113**, D13103.

Janjić, Zaviša I., 1994: The step-mountain eta coordinate model: Further developments of the convection, viscous sublayer, and turbulence closure schemes. *Mon. Wea. Rev.*, **122**, 927–945.

Jeong, Jee-Hoon, Hans W. Linderholm, Sung-Ho Woo, Chris Folland, Baek-Min Kim, Seong-Joong Kim, Deliang Chen, 2013: Impacts of snow initialization on subseasonal forecasts of surface air temperature for the cold season. *J. Climate*, **26**, 1956–1972.

Jiménez, Pedro A., Jimy Dudhia, J. Fidel González-Rouco, Jorge Navarro, Juan P. Montávez, Elena García-Bustamante, 2012: A revised scheme for the WRF surface layer formulation. *Mon. Wea. Rev.*, **140**, 898–918.

Kain, John S., 2004: The Kain–Fritsch convective parameterization: An update. *J. Appl. Meteor.*, **43**, 170–181.

Karion, Anna, Samuel Oltmans, Gabrielle Petron, Colm Sweeney, Russ Schnell, 2014: Analysis of aircraft observations. In T. Stoeckenius and D. McNally (Eds.), *Final Report: 2013 Uinta Basin Winter Ozone Study*, Chapter 4, 26 pp.

Katurji, Marwan, Shiyuan Zhong, 2012: The influence of topography and ambient stability on the characteristics of cold-air pools: A numerical investigation. *J. Appl. Meteor. Climatol.*, **51**, 1740–1749.

Lareau, Neil P., Erik Crosman, C. David Whiteman, John D. Horel, Sebastian W. Hoch, William O. J. Brown, Thomas W. Horst, 2013: The persistent cold-air pool study. *Bull. Amer. Meteor. Soc.*, **94**, 51–63.

Lareau, Neil P., 2014: *The Dynamics of Persistent Cold-Air Pool Breakup.* Ph.D. Thesis., University of Utah, 138pp.

Lareau, Neil P., J. Horel, 2014: Dynamically induced displacements of a persistent cold-air pool. *Bound-Layer Meteor.*, accepted.

Lippmann M., 1993: Health effects of tropospheric ozone: Review of recent research findings and their implications to ambient air quality standards. *J. Expo. Anal.*

Environ. Epidemiol., **3**, 103–129.

Lyman, Seth, Howard Shorthill, 2013: *Final Report: 2012 Uintah Basin Winter Ozone and Air Quality Study*, 285 pp.

Malek, E., T. Davis, R. Martin, and P. Silva, 2006: Meteorological and environmental aspects of one of the worst national air pollution episodes (January, 2004) in Logan, Cache Valley, Utah, USA. *Atmos. Res.*, **79**, 108–122.

Niu, Guo-Yue, et al., 2011: The community Noah land surface model with multiparameterization options (Noah-MP): 1. Model description and evaluation with local-scale measurements. *J. Geophys. Res.*, **116**, D12109.

Pollack, I. B., Thomas B. Ryerson, Michael Trainer, J. A. Neuman, James M. Roberts, David D. Parrish, 2013: Trends in ozone, its precursors, and related secondary oxidation products in Los Angeles, California: A synthesis of measurements from 1960 to 2010. *J. Geophys. Res. Atmos.*, **118**, 1–19.

Reeves, Heather Dawn, David J. Stensrud, 2009: Synoptic-scale flow and valley cold pool evolution in the western United States. *Wea. Forecasting*, **24**, 1625–1643.

Reeves, Heather Dawn, Kimberly L. Elmore, Geoffrey S. Manikin, David J. Stensrud, 2011: Assessment of forecasts during persistent valley cold pools in the Bonneville Basin by the North American Mesoscale Model. *Wea. Forecasting*, **26**, 447–467.

Roberts, James M., and Coauthors, 2014: Intensive chemical measurements at Horsepool. In T. Stoeckenius and D. McNally (Eds.), *Final Report: 2013 Uinta Basin Winter Ozone Study*, Chapter 5, 96 pp.

Salmond, J. A., 2005: Wavelet analysis of intermittent turbulence in the very stable nocturnal boundary layer: Implications for the vertical mixing of ozone. *Bound-Layer Meteor.*, **114**, 463–488.

Schnell, Russ C., Samuel J. Oltmans, Ryan R. Neely, Maggie S. Endres, John V. Molenar, Allen B. White, 2009: Rapid photochemical production of ozone at high concentrations in a rural site during winter. *Nat. Geosci.*, **2**, 120–122.

Schnell, Russ, Bryan Johnson, Patrick Cullis, Chance Sterling, Emrys Hall, Rob Albee, Allen Jordan, Jim Wendell, Samuel Oltmans, Gabrielle Petron, Colm Sweeney, 2014: Tethered ozonesonde and surface ozone measurements in the Uintah Basin, winter 2013. In T. Stoeckenius and D. McNally (Eds.), *Final Report: 2013 Uinta Basin Winter Ozone Study*, Chapter 8, 48 pp.

Shin, Hyeyum H., Song-You Hong, 2011: Intercomparison of planetary boundary-layer parameterizations in the WRF model for a single day from CASES-99. *Bound-Layer Meteor.*, **139**, 261–281.

Shupe, Matthew D., Janet M. Intrieri, 2004: Cloud radiative forcing of the arctic surface: The influence of cloud properties, surface albedo, and solar zenith angle. *J. Climate*, **17**, 616–628.

Silcox, Geoffery D., Kerry E. Kelly, Erik T. Crosman, C. David Whiteman, and Bruce L. Allen, 2012: Wintertime $PM_{2.5}$ concentrations in Utah's Salt Lake Valley during persistent multi-day cold-air pools. *Atmos. Environ.*, **46**, 17–24.

Stoeckenius, Till, Dennis McNally, 2014: *Final Report: 2013 Uinta Basin Winter Ozone Study*, Chapter 2, 55 pp.

Thompson, Gregory, Paul R. Field, Roy M. Rasmussen, William D. Hall, 2008: Explicit forecasts of winter precipitation using an improved bulk microphysics scheme. Part II: Implementation of a new snow parameterization. *Mon. Wea. Rev.*, **136**, 5095–5115.

U.S. EPA, 2006: Air Quality Criteria for Ozone Related Photochemical Oxidants, Volume 1, 821 pp.

U.S. EPA, 2013: National Ambient Air Quality Standards (NAAQS). [Available online at http:// http://www.epa.gov/air/criteria.html.]

Verzijlbergh, R. A., H. J. J. Jonker, T. Heus, J. Vila-Guerau de Arellano, 2009: Turbulent dispersion in cloud-topped boundary layers. *Atmos. Chem. Phys.*, **9**, 1289–1302.

Whiteman, C. D., S. Zhong, W. J. Shaw, J. M. Hubbe, X. Bian, J. Mittelstadt, 2001: Cold pools in the Columbia Basin. *Wea. Forecasting*, **16**, 432–447.

Zängl, Günther, 2005a: Formation of extreme cold-air pools in elevated sinkholes: An idealized numerical process study. *Mon. Wea. Rev.*, **133**, 925–941.

Zängl, Günther, 2005b: Wintertime cold-air pools in the Bavarian Danube Valley Basin: Data analysis and idealized numerical simulations. *J. Appl. Meteor.*, **44**, 1950–1971.